2017

Single Molecule Ligand Binding Studies on CCR5 by Fluorescence Cross-Correlation Spectroscopy

Carlos Rico

SINGLE MOLECULE LIGAND BINDING STUDIES ON CCR5 BY FLUORESCENCE CROSS-CORRELATION SPECTROSCOPY

A Thesis Presented to the Faculty of

The Rockefeller University

in Partial Fulfillment of the Requirements for

the degree of Doctor of Philosophy

by

Carlos A. Rico

June 2017

SINGLE MOLECULE LIGAND BINDING STUDIES ON CCR5 BY FLUORESCENCE CROSS-CORRELATION SPECTROSCOPY

Carlos A. Rico, Ph.D.

The Rockefeller University 2017

The G protein-coupled receptor (GPCR) C-C chemokine receptor 5 (CCR5) is the major co-receptor for HIV-1. CCR5 binds to the viral glycoprotein gp120 allowing HIV particles to infect T cells. Currently, maraviroc is the only Food and Drug Administration (FDA) approved entry inhibitor for HIV-1 but resistance to maraviroc has been reported indicating the need for novel entry inhibitors. Recently, four peptides derived from RANTES (Regulated on Activation, Normal T cell Expressed and Secreted), the endogenous ligand of CCR5, were shown to induce different CCR5 signaling pathways and efficiently block viral entry. The peptide analogues are 5P12, which blocks HIV-1 entry but does not induce signaling or receptor internalization; 6P4, which is a non-biased ligand; PSC, which is a super agonist relative to RANTES; and 5P14, which does not activate G-protein mediated signaling yet induces receptor internalization. Yet, we lack mechanistic knowledge about how the analogues bind to CCR5. To address this issue, we have employed fluorescence cross-correlation spectroscopy (FCCS) to determine equilibrium dissociation and inhibition constants for the RANTES analogues binding to CCR5.

We developed a tandem affinity purification protocol to purify full-length, monomeric CCR5 from receptor truncations and oligomers. We fluorescently labeled CCR5 using the

SNAP tag, a functional tag derived from DNA alkyl transferase, with Alexa-488. We show similar cell surface expression for CCR5-SNAP and wild-type CCR5 using flow cytometry with different epitope recognizing antibodies. We demonstrate that CCR5-SNAP activates G-proteins and internalizes similarly as wild type CCR5 in response to chemokine stimulus. We perform saturation and competition binding with the Alexa-647 labeled RANTES analogues and show that they bind with picomolar to nanomolar affinities. Global fitting on the binding isotherms shows that the RANTES analogues bind to 38% of CCR5-SNAP and recognize two different species that are non-interconvertible. Competition binding with gp120 complexed to soluble CD4 shows that the RANTES analogues are efficient at blocking Env binding. We also show that the native chemokines are incapable of displacing the RANTES analogues from CCR5-SNAP. We speculate that CCR5-SNAP is modified differentially with post-translational modifications that affect receptor affinity for the analogues. Our studies were performed with CCR5-SNAP in detergent solution that is not suitable to investigate the role G-protein on CCR5-SNAP ligand binding. To address this issue, we developed a novel zebrafish derived apolipoprotein AI (ZapN1) for the assembly of nanoscale apolipoprotein bound bilayers (NABBs). We optimized expression and purification of ZapN1 from *E*. coli and the assembly of NABBs with different lipids and detergent conditions. We performed FCCS ligand binding with CCR5-SNAP in NABBs to show that the receptor can recognize a conformationally sensitive antibody. Our studies illustrate the advantage of single molecule ligand binding assays to study receptor species that are averaged in ensemble measurements

ACKNOWLEDGEMENTS

To describe my journey from these past few years, it would require more than a few pages to do justice to the challenges and triumphs that shaped who I am today as an individual and scientist. However, one thing is clear, and that is, I am very thankful to all the people that helped me in my journey. For without them, I would not be where I am today. As much as I may be tempted to profess this as my success, it is truly the success of all the people who contributed their time, energy, and resources to make this dissertation a reality. To all of them I dedicate this dissertation for it is the work of all of us. Words alone won't truly convey how thankful and honored I am to have had the opportunity to work on this thesis and all the projects and experiments I describe hereafter. Nonetheless, I will put forth my most sincere thoughts to words and thank all who supported and guided me throughout this journey. I would like to being by thanking my advisor Thomas Sakmar. Dear Tom, thank you for taking me under your tutelage. I feel extremely privileged to have had the opportunity to do research at a world-class laboratory. I value that you encourage independence, that you fostered a collaborative and friendly environment, that you trust your mentees to be productive and excel in their projects. Moreover, I thank you for your sincere kindness and compassion you display. You truly care about the success of each one of your mentees as well as their personal wellbeing. You pushed and challenged me to ensure the success of this project. I would also like to thank Thomas Huber, my second advisor, for all his mentorship, advice, discussions, and hard work. I appreciate that you took the time to discuss experiments, data, or just any idea with me despite your very busy schedule. I admire how thoughtful, precise, and knowledgeable your contributions are. You challenged me every day to be a

better scientist, to be more attentive to detail, to design well thought-out experiments. I thank you for all the time, energy, and hard work you have invested on my scientific and professional development and the success of this project. I would also like to thank Yamina Berchiche, Emily Lorenzen, and Alexandre Furstenberg four our fruitful and wonderful collaboration in characterizing the receptor constructs we made, for your efforts in analyzing and discussing data, for your advice and comments in the development of the FCCS project. You made a tremendous contribution to this project and I hope you are as proud as I am of the work we did together. I would like to my parents, Hector Lopez and Maria Aguirre, my brother, Hector Rico for their continued devotion and support throughout these years. Even thou you are hundreds of miles apart; your love and support have made me feel that you are closer than ever. I cannot imagine making it throughout these years without your love. I would also like to thank my friends Mikel Etchegaray, Adah Jung, Axel Azcue, Alex Ossola, Shahin Islam, Suman Sarker, Dewi Harjanto, Derek Simon, Baris Reha, Jhin Villamor, and many others who gave me counsel, provided me support during difficult and stressful times, who were there and good and bad times and made my time in New York truly a memorable experience. I am thankful and honored to have you in my life and helped me through this process. I would like to thank Enida Vezelaj for all her support, care, encouragement, dedication, and motivation to be my best and do my best. Without you, I would not be who I am today as an individual and scientist. I would like to thank my committee members Vanessa Ruta, Olaf Andersen, and Barry Coller for some of their time to meet and discuss my progress, for their insightful and detailed comments, for their commitment and support throughout these past 6 years. I would also like to thank my external advisor, Elsa Yan, for being

willing to take part during my final examination and taking the time to travel to NYC to hear about my thesis projects. I would like to thank Adam Knepp and Minyoung Park with whom I worked closely on the FCS and NABBs project. I enjoyed working alongside you and I value the time we spent together imaging samples for FCS, discussing data, troubleshooting experiments, and learning new techniques. Your contributions to the FCS and NABBs projects laid the foundations for much of the data presented in this dissertation. I would also like to thank Dorien Staljanssens, Guy Smagghe, Margaret MacDonald, and Leonia Bozzacco for our fruitful collaborations with the NABBs. I enjoyed working alongside you and discovering novel applications for the NABBs. I would like to thank the Rockefeller Bio-imaging facility staff Alison North, Kaye Thomas, Christina Pyrgaki, and Pablo Ariel for training me on the LSM 780, providing me assistance and tremendous helpful advice during and after my FCS sessions. Without you, I could not have done any of the FCS and FCCS experiment hereby presented. I would also like to thank the Memorial Sloan Kettering Molecular Cytology Core Facility members Katia Manova, Navid Paknejad, and Matthew Brendel for their assistance and advice with the AFM imaging. I thank you for all your efforts to image the NABBs despite your very busy schedule. I would also like to thank Jennifer Peeler, Vallen Graham, He Tian, and Manija Kazmi for all the scientific discussions we had, helping me find my way around the lab, and taking the time to answer all my questions. You made the lab feel very welcoming and warm when I arrived. I would also like to thank all the other Sakmar lab members for all your help, the time we spent together as colleagues and friends, for your scientific inputs during my stay here, for your friendliness and collegiality, for your spirits, for your motivation and passion for science.

I would also love to thank the Rockefeller University Dean's office and the Tri-Institutional Training Program in Chemical Biology for providing an amazing environment for students to learn and become competent scientists. I appreciate all the effort you dedicate to ensure the student's well-being and success.

TABLE OF CONTENTS

LIST OF FIGURES

LIST OF TABLES

LIST OF ABBREVIATIONS

AFM	Atomic force microscopy
ApoAI	Apolipoprotein AI
BGHR	Bovine growth hormone reverse
BRET	Bioluminescence resonance energy transfer
BSA	Bovine serum albumin
cAMP	Cyclic adenosine monophosphate
CC	Cross-correlation
CHAPS	3-[(3-Cholamidopropyl)dimethylammonio]-1-propanesulfonate
CHS	Cholesteryl hemisuccinate
DAG	Diacyl glycerol
DAPI	2-(4-amidinophenyl)-1H-indole-6-carboxamidine
DDM	n-dodecyl-β-D-maltopyranoside
DLPC	1,2-dilauroyl-sn-glycero-3-phosphocholine
DMEM-Q	Dulbecco's modified eagle's medium - glutamine
DMPC	1,2-dimyristoyl-sn-glycero-3-phosphocholine
DNA	Deoxyribonucleic acid
dNTP	Deoxynucleoside triphosphate
DOPC	1,2-dioleoyl-sn-glycero-3-phosphocholine
DOPS	1,2-dioleoyl-sn-glycero-3-phospho-L-serine
DPPC	1,2-dipalmitoyl-sn-glycero-3-phosphocholine
DTT	Dithiothreitol

EC	Extracellular
EDTA	Ethylenediaminetetraacetic acid
EM	Electron microscopy
EPAC	Exchange protein directly activated by cAMP
EtBr	Ethidium bromide
FBS	Fetal bovine serum
FCS	Fluorescence correlation spectroscopy
FCCS	Fluorescence cross-correlation spectroscopy
FLIM	Fluorescence lifetime imaging microscopy
FPLC	Fast protein liquid chromatography
FRET	Förster resonance energy transfer
GEF	GTPase nucleotide exchange factors
GPCR	G protein-coupled receptor
GFP	Green fluorescent protein
GTP	Guanosine triphosphate
GTPase	Guanosine triphosphatase
HBSS-H	Hank's Balanced Salt Solution – HEPES
HDL	High density lipoprotein
HEK	Human embryonic kidney cells
HEPES	4-(2-hydroxyethyl)-1-piperazineethanesulfonic acid
IC	Intracellular
IP_3	Inositol 1,4,5-triphosphate
IPTG	Isopropyl β-D-1-thiogalactopyranoside

ITC	Isothermal titration calorimetry
LB	Luria-Bertani
LRB-PE	1,2-dipalmitoyl-sn-glycero-3-phosphoethanolamine-N-(lissamine rhodamine B sulfonyl)
mAb	Monoclonal antibody
MBS	Main beam splitter
MES	2-(*N*-morpholino)ethanesulfonic acid
NIR	Near infrared
OD_{600}	Optical density at 600 nm wavelength
pAb	Polyclonal antibody
PBS	Phosphate buffered saline
PE	Phycoerythrin
PCR	Polymerase chain reaction
PIP_2	Phosphatidylinositol 4,5-bisphosphate
PMSF	Phenylmethylsulfonyl fluoride
POPC	1-palmitoyl-2-oleoyl-sn-glycero-3-phosphocholine
PSF	Point spread function
PVDF	Polyvinylidene difluoride
RANTES	Regulated on Activation, Normal T cell Expressed and Secreted
RFU	Relative fluorescence units
RLuc3	*Renilla* luciferase 3
ROS	Rod outer segments
RT	Room temperature

SDS-PAGE	Sodium dodecyl sulfate polyacrylamide gel electrophoresis
SEM	Standard error of the mean
SOC	Super optimal broth with catabolite repression
SOPC	1-stearoyl-2-oleoyl-sn-glycero-3-phosphocholine
SP-FLAG	Signal peptide-FLAG
SPR	Surface plasmon resonance
SUV	Small unilamellar vesicles
TAE	Tris base, acetic acid, and EDTA
TB	Terrific broth
TM	Transmembrane
WT	Wild-type

CHAPTER ONE: INTRODUCTION

1.1 G Protein-Coupled Receptors Activation and Signaling Pathways

G-protein coupled receptors (GPCRs) are heptahelical trans-membrane receptors responsible for signal transduction across the plasma membrane.[1] GPCRs regulate many important physiological processes, such as vision, smell, cognitive, metabolic, and immune responses.[2] GPCRs constitute a large and diverse family of receptors with more than 800 members classified into 5 classes: rhodopsin (class A), secretin (class B), adhesion (originally class B), glutamate (class C), and frizzled/taste2.[3] The largest GPCR class is the rhodopsin family with 701 members of which 241 receptors are non-olfactory receptors. GPCRs share a common structural framework of 7 transmembrane α-helices with an extracellular N-terminus, intracellular C-terminus, and various loops between transmembrane helices.[4] Ligands bind GPCRs on the extracellular side leading to receptor structural rearrangements that allow coupling and activation of G protein on the intracellular side.[5] GPCRs bind a plethora of chemically diverse ligands such as ions, synthetic molecules, lipids, and proteins despite their conserved structural framework.[2] Specific receptor-ligand contacts in the N-terminus and transmembrane interhelix domain dictates ligand specificity.[6, 7] Despite their broad ligand recognition, GPCRs share a common mechanism of activation and G-protein coupling.[6, 8] GPCRs share conserved structural motifs in the transmembrane interhelix domain responsible for receptor activation.[9] Two such motifs, the (D/E)RY and NPxxY$(x)_{5,6}$F motifs regulate receptor transition from the inactive to the active state.[6] The (D/E)RY

motif is conserved in several receptors located between transmembrane III (TMIII) and intracellular loop 2 (ICL2). [10] The arginine residue forms a salt bridge with either the glutamic or aspartic residue in TMVI constraining the receptor in an 'inactive' conformation. Ligand binding displaces TMVI from the interhelix domain breaking the salt bridge leading to an 'active' receptor conformation.[11, 12] Mutations of glutamic or aspartic acid lead to constitutionally active receptors. The (D/E)RY motif functions to keep the receptor in the inactive state to prevent its activation. GPCRs also encode for another conserved motif, NPxxY$(x)_{5,6}$F, which connects TMVII and cytoplasmic helix VIII.[13] The NPxxY$(x)_{5,6}$F motif forms a helix-turn-helix structure which is stabilized by hydrophobic interactions between the tyrosine and phenylalanine residues.[14] Alanine mutations in the NPxxY$(x)_{5,6}$F motif that disrupt the hydrophobic interaction allows the receptor to proceed to the 'active' state at the expense of reduced G-protein activation. The NPxxY$(x)_{5,6}$F motif is important for receptor activation and G-protein coupling. Yet, not at all GPCRs encode for these conserved motifs indicating that they are not essential for GPCR activation and G-protein coupling.

Ligand binding on the EC domain allows heterotrimeric G-protein to bind the active state receptor in the IC side. G-proteins are composed of Gα, Gβ, and Gγ subunits of which Gα contains the catalytic site for nucleotide exchange.[15] GPCR activation leads to the exchange of GDP to GTP in Gα and its dissociation from the Gβγ dimer. Gα is classified into 4 different sub-families, $G\alpha_i$, $G\alpha_s$, $G\alpha_q$, and $G\alpha_{12/13}$ based on their signaling pathway coupling.[16] $G\alpha_i$ and $G\alpha_s$ bind to adenylyl cyclase either inhibiting or stimulating production of cyclic adenosine monophosphate (cAMP) respectively. $G\alpha_q$ activates phospholipase C which cleaves phosphatidylinositol 4,5-bisphosphate (PIP_2) into diacyl

glycerol (DAG) and inositol 1,4,5-trisphosphate (IP_3).[17] $G\alpha_{12/13}$ activates members of the RhoGTPase nucleotide exchange factors (RhoGEFs) family such as p115-RhoGEF.[18] The Gβγ dimer activates voltage-gated calcium and potassium channels, and regulates several signaling effectors such as adenylyl cyclase and phospholipase C.[19] Following G-protein dissociation from the receptor-ligand complex, GPCRs can be phosphorylated by G protein-coupled receptor kinases (GRKs) on serine and threonine residues located in the IC loops and receptor C-terminus.[20] GPCR phosphorylation induces high affinity binding of the intracellular effector arrestin.[21] Arrestin prevents further G-protein activation and targets the receptor for internalization via clathrin-mediated endocytosis. Arrestin also regulates activation of several kinases such as the Scr family of tyrosine kinases, c-Jun N-terminal kinase 3, mitogen-activated protein (MAP) kinases, and extracellular signal-regulated kinases (ERK) 1 and 2. Internalized GPCRs are then targeted to the lysosome for degradation or recycled to the plasma membrane for future activation.[22]

Ligands can modulate GPCR coupling to either G-protein or arrestin in a phenomenon known as “biased agonism” [8]. For example, SNC80, a δ-opioid receptor agonist, induces high receptor internalization in the central and peripheral nervous system which leads to behavioral desensitization in animals [23]. ARM390 is another δ-opioid agonist with similar selectivity and potency as SNC80 but it induces low internalization abolishing behavioral desensitization. Biased signaling has been observed for several other GPCRs including the beta adrenergic receptors 1 and 2, the ghrelin receptor, vasopressin 2 receptor, and serotonin $5HT_{2B}$ and receptors.[24] The binary model of GPCR activation assumes that the receptors exists between an inactive and active

states.[8] Ligand binding stabilizes the active state which is responsible for intracellular partner binding and regulation. However, the binary model cannot account for biased signaling since one receptor conformation cannot be responsible for G-protein, GRK, and arrestin coupling. Given this, GPCRs are believed to adopt multiple conformations, which can be stabilized differentially by ligands. Structural and biophysical evidence shows that GPCRs are dynamic structures that can adopt multiple conformations.[25] For example, ^{19}F-NMR studies in the β2-adrenergic receptor revealed the existence of two receptor conformational states associated with TMVI and TMVII. Agonist binding shifted the equilibrium towards the TMVI conformational state while arrestin biased agonists shifted the equilibrium towards the TMVII state. Crystal structure of the β2-adrenergic receptor bound $G\alpha_s$ showed that TMVI was displaced away from the transmembrane interhelix domain by 14 Å.[26] In contrast, the rhodopsin-arrestin complex shows additional contacts made with TMVII and cytoplasmic helix 8 and the receptor C-terminus makes several ionic contacts with positively charged residues in arrestin.[27] Despite the available structural data, we do not understand how ligands modulate receptor transitions along the conformational landscape. Given this, further studies are required to understand the mechanistic parameters that define biased agonism. Such understanding will guide future therapeutic development of novel drugs that mitigate unwanted side effects while retaining the desired effect. [28, 29] We propose to investigate how a series of biased peptide analogues bind to the chemokine receptor CCR5.

1.2 CCR5 is a Model GPCR

CCR5 is a chemokine GPCR that is expressed on monocytes, macrophages, dendritic cell, natural killer cells, memory and effector T cells, fibroblasts, and neuronal cells where it directs cells to inflammation and infection sites and stimulates T-cells [30, 31]. Chemokines are small chemoattractant cytokines that modulate various biological processes such as chemotaxis, inflammation, and viral infection.[32] Chemokines are sub-divided into 4 families differentiated by their cysteine motifs: CXC chemokines (α-chemokines), CC (β-chemokines), C chemokines (γ-chemokines), and CX_3C chemokines (δ-chemokines).[33] CCR5 recognizes primarily the CC chemokines CCL5 (RANTES), CCL3 (MIP-α), and CCL4 (MIP-1β).[34] RANTES mediates proliferation and activation of natural killer cells and induces chemotaxis in T cell, monocytes, and dendritic cells. MIP-α and MIP-1β also induce chemotaxis in monocytes, macrophages, and dendritic cells but MIP-α preferentially attracts CD8+ T cells while MIP-1β preferentially attracts CD4+ T cells.[35, 36] CCR5 also recognizes envelope glycoprotein gp120 in HIV. Gp120 first binds to the membrane receptor CD4 which then exposes variable loop 3 (V3) in gp120 that then binds to CCR5 [37]. Maraviroc is the only Federal Drug Administration (FDA) approved HIV-1 entry inhibitor but there are viral strains that are resistant to Maraviroc [38]. RANTES inhibits HIV-1 replication but it has very low potency compared to other entry inhibitors such as Maraviroc [39]. To address this issue, RANTES analogs that inhibit HIV-1 with picomolar potencies were developed by random mutagenesis in the first 9 amino acids (Table 1.1.2)[40, 41]

Table 1.2 Characterization of RANTES and some of its peptide analogues. The RANTES analogues investigated in this report have several amino acid mutations within the first 9 amino acids. The RANTES N-terminus sequence is shown for comparison. PSC-RANTES is the only analogue to be chemically modified where PSC is N^{α}-(*n*-nonanoyl)-*des*-Ser[1]-[L-thioproline[2], L-α-cyclohexyglycine[3]]. RANTES has very low anti-HIV potency while the RANTES analogues display picomolar inhibition potencies. PSC and 6P4-RANTES display "super-agonist" activity in comparison to RANTES in that they are more effective in G-protein signaling and CCR5 internalization than RANTES (numbers are % of PSC-RANTES activity). 5P12-RANTES does not show appreciable G-protein signaling or CCR5 internalization by either functional assay. 5P14-RANTES shows no G-protein signaling but can induce CCR5 internalization. The RANTES analogues show similar affinities based on the displacement of ^{125}I-MIP-1β from CHO cells expressing CCR5.

Ligand	N-terminal Sequence	Anti-HIV potency (pM)	G protein signaling (% PSC)	CCR5 internalization (% PSC)	Binding affinity (nM)
RANTES	S-P-Y-S-S-D-T-T-P	~ 1000000	50	64	7.9
PSC-RANTES	PSC-S-S-D-T-T-P	25	100	100	1.9
6P4-RANTES	Q-G-P-P-G-D-I-V-L-A	21	88	93	0.3
5P12-RANTES	Q-G-P-P-L-M-A-T-Q-S	28	<5	3	1.3
5P14-RANTES	Q-G-P-P-L-M-S-L-Q-V	26	<5	47	1.2

Remarkably, the RANTES analogues display very different functional properties from RANTES on CCR5 cell-based assays. For example, PSC-RANTES (PSC) and 6P4-RANTES (6P4) display "super-agonist" activity in comparison to RANTES while 5P14-

RANTES (5P14) and 5P12-RANTES (5P12) show no G-protein activation by calcium flux. 5P14 was half-effective at inducing CCR5 internalization when compared to PSC while 5P12 did not induce CCR5 internalization (Table 1.1.2). The RANTES analogues display similar affinities towards CCR5 expressed in cells based on their displacement of ^{125}I-MIP-1β.[40] Gaertner (2008). deduced that their similar affinities could not account for the analogues different pharmacological properties. However, CCR5 is known to partition into different lipid environments and measured affinities from cell based assays are an average of all CCR5 states [42, 43]. Therefore, we propose to derive dissociation binding constants, K_D, and constants of inhibition, K_i, for the RANTES analogues at the single molecule scale to characterize their binding mechanism to CCR5 [44, 45].

1.3 Ligand Binding Assays

We propose to perform saturation binding and competition binding with the RANTES analogues and native chemokines to derive their K_D and K_i values. Equilibrium binding assays provide information about ligand affinities, receptor species, and the mechanism by which ligands interact with receptors.[46] We hypothesize that the RANTES analogues bind to different CCR5 conformations or receptor species, which may be responsible for their pharmacological properties. Traditionally, radiolabeled ligands had been employed to measure affinities to a receptor expressed in cells or purified in membrane preparations.[47] Radioligand binding assays are advantageous in that they can be performed in primary cell cultures and recombinant expression systems. As such, radioligand binding assays probe receptor-ligand interactions in a native environment without disrupting receptor function. Radioligand binding assays are also advantageous

in that they provide information about receptor distribution, density, and dynamics. Yet, radioligand binding assays present several disadvantages such as working with radioactive reagents, which are hazardous and expensive to synthesize. Radiolabeling can also modify ligand properties specially if the labeling site is not specific. An alternative to radioligand binding assays is surface plasmon resonance (SPR) or isothermal titration calorimetry (ITC) that can measure affinities on purified or reconstituted receptor without labeling or ligand or receptor.

Surface plasmon resonance detects refractive index changes from addition of an analyte to a sensor surface with immobilized receptor. Unlike radioligand binding assays, most SPR assays require receptor purification, which may affect its ligand binding properties. However, SPR offers several advantages over radioligand binding assays. For example, SPR relies on measuring refractive index changes, which do not require labels on either the ligand or receptor. Furthermore, SPR monitors reactions on real-time allowing derivation of rate constants and K_D values from the same experiments. SPR requires lower concentration of reagents in comparison to radioligand binding assays. Yet, SPR does have disadvantages in comparison to radioligand binding assays. For example, analytes that induce small changes in refractive index may not be observed at all. Also, SPR measurements are susceptible to mass transport effects. SPR data analysis requires the assumption that the free analyte concentration is uniform in space and time. However, the assumption breaks down when analyte diffusion and/or flow does not result in a homogeneous analyte distribution in the sensor chip. As such, ligand association rates to the receptor are dependent on analyte diffusion into the receptor-dextran matrix. SPR also

requires receptor surface immobilization, which can introduce artifacts or alter receptor function.

An alternative to SPR is ITC, which measures changes in heat released or absorbed caused by a binding event. Unlike SPR, ITC measures ligand interactions in solution overcoming possible immobilization artifacts and the technique is not limited by the molecular weight of the analytes. ITC provides information such as K_D, the number of binding sites, and thermodynamic parameters such as the change of enthalpy and entropy but it does not provide rate constants. ITC is useful to measure ligand-binding interactions with affinities in the millimolar to nanomolar range. However, the technique is limited to high reagent concentrations are required to detect ligand binding. For example, the minimum protein required is 10 μM for a 200 μl cell and a ΔH of 5 kcal/mol.[48] Ideally, we would like to use a technique that can detect ligand binding with nanomolar receptor and ligand concentrations. ITC measurements are also susceptible to buffer mismatch between the ligand and receptor, which affect the measured ΔH.

Methods such as X-ray crystallography and NMR provide precise information about the structural determinants of ligand binding at atomic resolution. In the last decade, several GPCR structures bound to antagonists, agonists, G-protein mimics and G-protein, and arrestin have emerged providing key insights into different ligand binding modes and receptor activation. GPCRs are notoriously difficult to purify in high quantities and to crystallize due to their inherent dynamical nature. In many cases, GPCRs were heavily modified with stabilizing mutations and fused to proteins such as T4 lysozyme to create larger lattice contacts. Also, structural methods provide a snapshot of a single receptor

conformation eliminating the conformational diversity that characterizes these proteins. Given this, we advocate for a technique that allow us to probe ligand-binding interactions without heavily perturbing receptor structure and function. Also, we would prefer a technique that allow us to investigate the dynamic behavior of these receptors in an environment that preserves their function.

Fluorescence based ligand binding assays offer several advantages over traditional methods. For example, fluorescence detection can be performed using different wavelengths of light, which allows for multi-color detection of several species. For example, the ligand and receptor can be monitored independently in binding measurements by placing different labels on them. Fluorescent ligand binding assays can be performed on cells or in solution allowing for direct comparison of measured affinities. Yet, fluorescence detection offers a tremendous advantage that the previously discussed methods do not offer. Given the conformational diversity of GPCRs, methods such as SPR and radioligand binding would not provide information about such different conformations since they average the entire ensemble. Single molecule interrogation allows us to observe conformations or transitions along the reaction pathway that are typically averaged in ensemble measurements. Given this, we propose to perform single molecule ligand binding measurements using a technique known as fluorescence correlation spectroscopy.

1.4 Fluorescence Auto- and Cross-Correlation Spectroscopy

Fluorescence correlation spectroscopy (FCS) is a statistical method that analyzes fluorescence fluctuations from molecules in a femtoliter sized volume of focused laser excitation. [49] To derive physical parameters, an autocorrelation analysis is performed on the fluorescence intensity profile. FCS can be used to monitor any process that causes fluorescence fluctuations such as diffusion, chemical reactions, changes in concentration, rotational diffusion, triplet state kinetics, and ligand binding. In 1972, Magde et al. derived the mathematical expressions to determine rate constants and diffusion coefficients for ethidium bromide binding to DNA. Recent advances in confocal microscopy such as correlators and improved laser for diffraction-limited sensitivity have allowed FCS to become a more routine method.[49] The auto-correlation function is defined in equation 1.1

$$G(\tau) = \frac{\langle F(t)F(t+\tau)\rangle}{\langle F\rangle^2} \qquad \text{(Equation 1.1)}$$

Where $F(t)$ is the fluorescence intensity in time and $F(t+\tau)$ is the fluorescence intensity at a lag time after t. To derive parameters that describe the system, an analytical expression of the auto-correlation function is fitted to the experimental correlation trace. Equation 1.2 gives the general form of the analytical expression for the correlation function

$$G_{Total} = 1 + A + \prod_k \sum_l G_{k,l}(\tau) \qquad \text{(Equation 1.2)}$$

Where A is the amplitude of the correlation function and $G_{k,l}(\tau)$ is the correlation for a single process where the suffixes are correlation terms that represent dependent or independent processes. Functional expressions of $G_{k,l}(\tau)$ can be used to derived concentrations, particle size, and triplet state fraction.[50] For example, A, the correlation amplitude $G(0)$, is given by $\frac{1}{N}$ where N is the number of fluorescent species. As such, changes in $G(0)$ can be used to determine fluctuations in concentration caused by chemical reactions. To illustrate how correlation traces change with varying concentration, particle size, and triplet state fraction, we have modeled correlation traces for such processes using functional forms $G_{k,l}(\tau)$ (Methods and Materials) with a set of fixed parameters. Figure 1.1.4a shows the modeled correlation traces and how changes in concentration, size, and triplet state fraction affect the form of the correlation function.

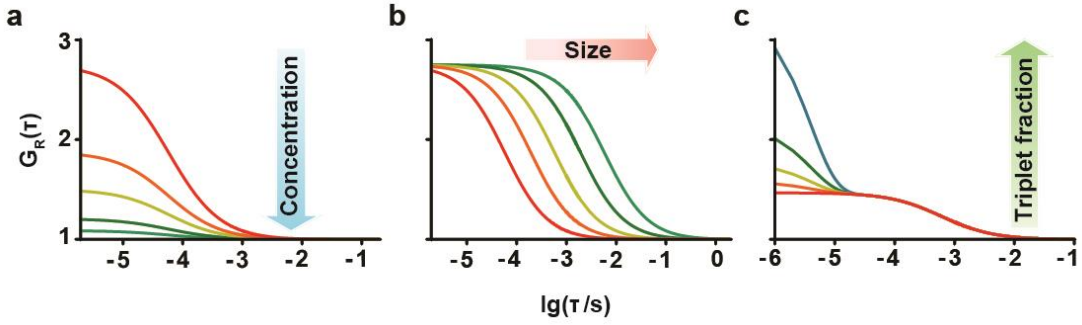

Figure 1.1.4a Dependency of correlation trace amplitudes and lag time (τ) on fluorescent species concentration (a); molecular size (b); and triplet state fraction (c). Correlation amplitude is plotted on the y-axis, $G_R(0)$, as a function of lag time, τ, in a logarithmic x-axis.

As described before, $G(0)$, is inversely proportional to the total number of particles present in the sample. If the concentration of the fluorescent species decrease, then the autocorrelation amplitude increases (Figure 1.1.4a). The diffusion time, τ_D, of a particle is related to the particle's molecular weight and diffusion coefficient. Increases in the diffusion time can be used to detect ligand binding or changes in particle size (Figure 1.1.4a). Fluorescence fluctuations also arise from triplet state transitions that appear as a second decay component in the microsecond timescale (Figure 1.1.4a). FCS is advantageous over other single molecule techniques in that concentrations can be derived directly for any fluorescent sample. Binding interactions are observed in solution eliminating immobilization artifacts common to other single molecule techniques.

FCS has previously been employed to derive K_D values for the serotonin receptor $5HT_{3AS}$ antagonist GR-119566X labeled with different fluorophores in solution [51]. Measuring binding interactions by FCS is limited to ligand-receptor pairs that are vastly different in size. Fluorescence cross-correlation spectroscopy (FCCS) overcomes this limitation by cross-correlating the fluorescence fluctuations from two different fluorescent species.[52] Figure 1.1.4b shows a schematic of two confocal volumes (blue corresponds to 488 nm excitation and red to 633 nm excitation) overlapping with each other under the assumption of no chromatic aberrations. In each case, we show particles that are bound to each and diffusing together or do not interact and diffuse through the confocal volumes independently.

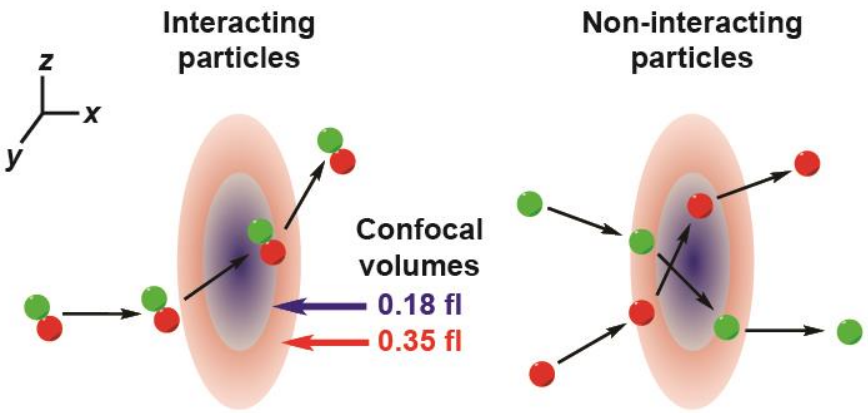

Figure 1.1.4b Schematic showing the confocal volumes for 488 nm excitation (blue ellipse), 633 nm excitation (red ellipse), and their calculated sizes and orientations (xyz coordinates). Green sphere corresponds to a green-labeled species and the red sphere to a red labeled species that either interact (left) or do not interact (right).

We have previously determined the confocal volumes for 488 and 633 nm excitations and determined their values to be 0.18 fl and 0.35 fl respectively. Particles that are bound diffuse together yielding a cross-correlation amplitude that is dependent only on the bound complex concentration. Figure 1.1.4c shows the averaged fluorescence intensity profiles for the two binding cases and their associated auto- and cross-correlation traces.

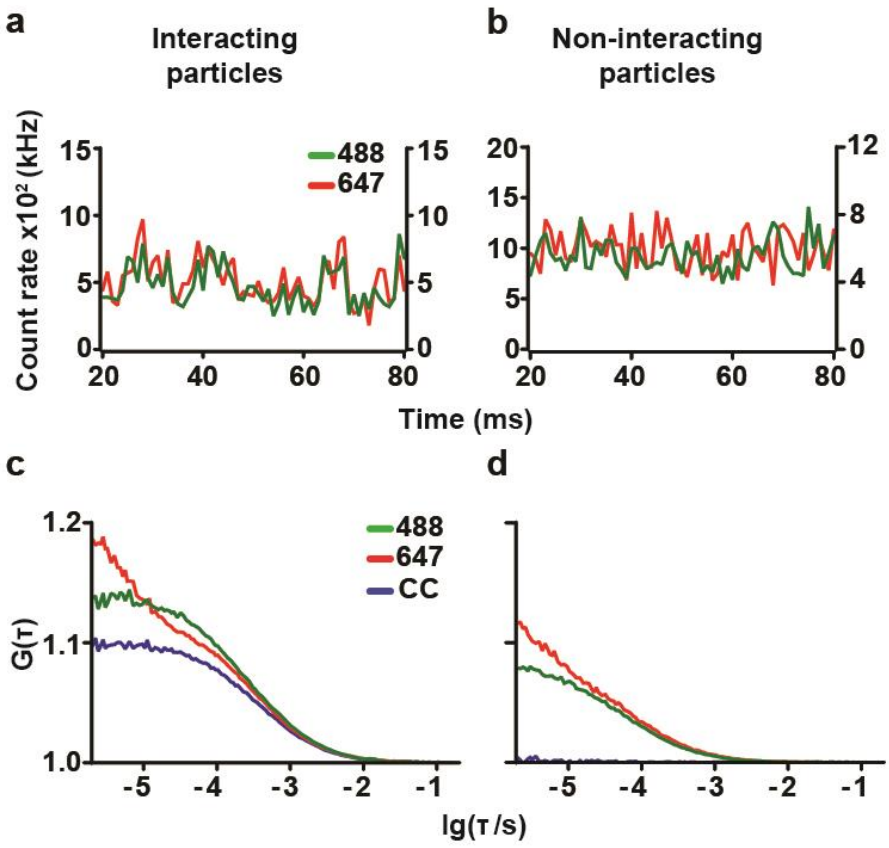

Figure 1.1.4c Averaged fluorescence intensity profiles for green and red labeled particles that are interacting (a) or not interacting (b). Correlation traces for green and red labeled particles that bind or do not bind. Particles that bind (c) yield a cross-correlation amplitude (blue line), which is absent if the particles do not interact.

The averaged fluorescence intensity profiles overlap with each other if the particles interact. In the case where the particles do not interact, the averaged fluorescence intensity profiles do not overlap with each other. Correlation analysis on the intensity profiles yields a third correlation trace, which is dependent solely on the concentration of complex. In the case where particles bind, the cross-correlation amplitude is present whereas in the non-binding case the cross-correlation amplitude is absent. FCCS has been

employed previously to derive K_D values for the peptide ligand Leu-enkephalin binding to the human μ-opioid receptor in membrane nanopatches [53]. FCCS has also been employed to derive K_D and K_i values for different fluorescent labeled ligands binding to solubilized GPCRs in cell lysate supernatant [54]. Given the advantages of FCCS over FCS and other ligand binding methods, we propose to employ FCCS on CCR5 to derive equilibrium dissociation constants, K_D, and constants of inhibition, K_i, for the RANTES analogues. We propose to perform saturation and competition binding on purified CCR5 in a well-defined micelle-lipid system where we can identify possible CCR5 species that are masked in ensemble measurements 15,16.

CHAPTER TWO: FUNCTIONAL CHARACTERIZATION, EXPRESSION, LABELING, AND PURIFICATION OF CCR5

2.1 Introduction

To perform FCCS measurements on CCR5 and the chemokines, we must label the receptor and chemokines with two different fluorophores. Also, we need to purify CCR5 in a suitable buffer-detergent solution to high purity to avoid heterogeneities in the final purification product. Given these challenges, we have designed a CCR5 construct fused to several functional tags that allow us to label the receptor with any small organic fluorophore and purify the full-length receptor from cell lysates. Human CCR5 was codon optimized for higher expression in mammalian cells and fused to the SNAP tag for fluorescent labeling. The SNAP tag is an O^6-guanine nucleotide alkyltransferase mutant.[55] The SNAP tag unlike traditional fluorescent proteins allow us to covalently attach any benzyl guanine derivatized fluorophore into the protein. The SNAP tag works by binding the benzyl guanine moiety and then using a free cysteine performs nucleophilic substitution to attach itself to the fluorophore (Figure 2.1.1)

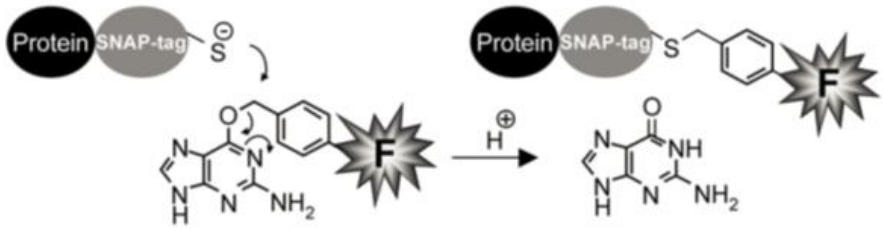

Figure 2.2.1 SNAP-tag labeling mechanism.

Because the SNAP tag recognizes only benzyl guanine derivatives, the SNAP tag offers excellent bio-orthogonality in comparison to other labeling methods. For FCCS, we will employ Alexa-647 labeled chemokines synthesized by Oliver Hartley's group. We will label CCR5 with Alexa-488 using a C-terminal SNAP-tag. We chose the C-terminal position since the N-terminal fusion construct can undergo FRET with the labeled chemokine affecting FCCS measurements.

Since we want to purify our CCR5-SNAP fusion protein from cells, we have designed our construct to encode for three additional functional tags for purification and expression. For receptor purification, we will employ an N-terminal FLAG and C-terminal 1D4 tags. The positions of the functional tags allow us to purify full-length receptor from the cell lysate. Studies in CXCR4, a related chemokine receptor, have shown that N-terminal modifications severely affect receptor trafficking to the plasma membrane (unpublished observation). To resolve this issue, we also introduced a signal peptide from the serotonin $5HT_{3A}$ receptor upstream the FLAG tag to induce proper receptor trafficking and expression.[56] We also characterized CCR5-SNAP using pharmacological assays to demonstrate that the receptor functions like WT CCR5.

In the following sections, we describe CCR5-SNAP construct design from a previous template to introduce the signal peptide and the FLAG tag. We also describe several functional assays such as calcium mobilization and cAMP inhibition to demonstrate that the receptor functions like WT CCR5. We also describe the labeling and purification method developed to obtain full-length, monomeric CCR5-SNAP from HEK2P3T cells. We employed SDS-PAGE analysis and FCS to evaluate the affinity purification. We

show that CCR5-SNAP can be purified away from receptor truncations and aggregates and that the method is robust and reproducible.

2.2 Materials and Methods

2.2.1 Sequence Design and Molecular Cloning of CCR5-SNAP

1.0 μg of plasmid encoding the $5HT_{3A}$ serotonin receptor signal peptide and FLAG tag (SP-FLAG) sequence was digested with MlyI (New England Biolabs, Ipswich, MA) for 2 hours at 37 °C. MlyI was heat-inactivated by incubating for 20 minutes at 65 °C. The SP-FLAG fragment was purified from the linearized plasmid by agarose gel (0.8%) electrophoresis in 1x TAE with ethidium bromide (0.5 μg/ml). The desired bands were isolated from the gel and purified using QIAGEN's gel purify kit per the manufacturer's instructions (Germantown, MD). Methylation-free SP-FLAG was generated using Invitrogen's Pfx Platinum polymerase (Grand Island, NY) using the following forward primers 5-'GCTTCCTGCAGGAGATGATACC-3' and reverse primer 5-GCTGGACACCTGGTAATCCAT-3. Methylation-free SP-FLAG was purified by adding the PCR reaction directly to the spin filter from QIAGEN's gel purify kit and then proceeding with the protocol per the manufacturer's instructions. FLAG-SP was inserted upstream of human CCR5 using Agilent's Quikchange Lightning mutagenesis kit (Santa Clara, CA) with slight modifications. Briefly, 25 ng of CCR5 was added to 250 ng of purified, methylation-free SP-FLAG in the presence of dNTPs, Quikchange buffer, and

polymerase in 25 µl total volume. The PCR mixture was cycled using the parameters shown in Table 2.2.1.

Table 2.2.1 PCR cycling times and temperatures used to generate SP-FLAG-CCR5.

Segment	Cycles	Temperature (°C)	Time (s)
1	1	95	30
2	5	95	30
		52	60
		68	480
3	13	95	30
		55	60
		68	480

The PCR reaction was then used for bacterial transformation per Agilent's instructions. Single colonies were inoculated in 5 ml of LB media with ampicillin (50 µg/ml) and incubated for 12 hours at 37 °C. Plasmid DNA was isolated and purified from 3 ml of culture using QIAGEN's miniprep kit per the manufacturer's instructions. Samples were sequenced using the T7 forward primer, BGHR reverse primer, and several CCR5 internal primers. Sequencing results were analyzed using Snapgene and Omega Clustal. To generate FLAG-SP-CCR5-SNAP, FLAG-SP-CCR5 and CCR5-SNAP were digested with HindIII and KpnI-HF endonucleases for 16 hours at 37 °C. Enzymes were heat-inactivated by incubating the samples at 80 °C for 20 minutes. The DNA fragments were resolved by agarose gel (1.0 %) electrophoresis in 1x TAE. The desired bands were isolated using Millipore's DNA extraction centrifugal filter units (Billerica, MA). Ligation reactions were set-up using T4 DNA ligase (New England Biolabs) per the manufacturer's instructions. Reactions were incubated for 30 minutes at room

temperature and then 2 µl of sample was added to 20 µl of TOP10 chemically competent cells. Cells were incubated on ice for 30 minutes before heat-shocking them at 42 °C for 45 seconds. Cells were placed on ice for an additional 2 minutes and then 180 µl of SOC media was added to each sample. Cells were recovered for 1 hour at 37 °C with shaking in an Eppendorf thermomixer at 1,100 rpm. 200 µl of sample were plated onto individual LB-agar plates with ampicillin (50 µg/ml) for 16 hours at 37 °C. Single colonies were inoculated in LB media (5 ml) with ampicillin and incubated at 37 °C for 16 hours. DNA was isolated from 3 ml of culture using QIAGEN's miniprep and sequenced using T7 and BGHR primers. Successful clone was re-named simply as CCR5-SNAP.

2.2.2 Cell Culture and Transfection

HEK293T cells (passage number 5 to 15, ATCC, Manassas, VA) were maintained in DMEM-Q, 1% penicillin-streptomycin, and 10% fetal bovine serum (FBS) from Atlanta Biologicals (Flowery Branch, GA). Transient transfections including high-throughput in-plate transfections were performed using Lipofectamine 2000 according to manufacturer's instructions with some modifications as described previously (Berchiche & Sakmar 2016). Total transfected DNA was kept constant in all our experiments at 12 µg in 10cm dishes; 2 µg in 6 well plates; 100 ng in 96 well plates and 20 ng in 384 well plates by adding empty vector pcDNA3.1+.

2.2.3 Flow Cytometry

HEK293T cells transfected in six-well plates with 0.75 µg CCR5 W.T. or 2.0 µg CCR5-SNAP or 2 µg of empty vector pcDNA3.1+. Cells were detached in ice cold PBS. Cells were then distributed in 96 well round bottom plates, spun down and re-suspended in BRET buffer (PBS containing 0.5mM $MgCl_2$ and 0.1% BSA) containing, anti-CCR5 mAb (Clone 2D7) or anti-CCR5 (Clone T21/8) or anti-Flag PE for 45 minutes at 4°C. Cells were then washed three times in ice cold PBS. Cell surface expression was quantified by flow cytometry using the Accuri C6 flow cytometer (BD Biosciences).

2.2.4 Adenylyl Cyclase Activity

HEK293T cells were co-transfected in a high-throughput in-plate manner with 12 ng Rluc3-EPAC-GFP, a $BRET^2$ cAMP sensor, and 23 ng CCR5 W.T. or 60 ng CCR5-SNAP or 88 ng of empty vector pcDNA3.1+. Cells were then plated into 0.01% poly-D-Lysine coated 96-well, white microplates with clear bottom at a density of 100,000 cells/well. Twenty-four hours post transfection; media was replaced with BRET buffer. Coelenterazine 400A was added at a final concentration of 5 µM followed by a 5 minutes incubation at room temperature (RT). Cells were then stimulated with ligand in the presence or absence of 5 µM of forskolin at room temperature for 5 minutes. Luminescence and fluorescence readings were collected using the Synergy NEO2 plate reader from Biotek (Winooski, USA) and Gen5 software. $BRET^2$ readings between Rluc3 and GFP10 were collected by sequential integration of the signals detected in the 365 to

435 nm (Rluc3) and 505 to 525 nm (GFP10) windows. $BRET^2$ ratios were calculated as described previously [57, 58].

2.2.5 Calcium Flux Assay

For each well of a 384-well plate, 20,000 HEK293T cells were transfected with 10 ng CCR5 W.T. or 20 ng CCR5-SNAP. Transfected HEK293T cells were plated into 384-well plates (Corning) coated with poly-D-lysine hybrobromide (Sigma-Aldrich, St. Louis, MO) at 20 uL/well. Twenty-four hours post-transfection, 20 uL/well FLIPR calcium 6 dye (Molecular Devices, Sunnyvale, CA) was added to the cells and incubated for 1.5 hours at 37°C with 5% CO_2. The dye was dissolved in HBSS-H (Hank's Balanced Salt Solution with 20 mM HEPES, pH 7.4) and supplemented with 0.4% BSA (fatty acid free-Free, Roche). Prior to measurement, the plate was incubated at 37ºC for an additional 30 minutes in a pre-warmed FlexStation II 384 Plate Reader (Molecular Devices). Ligands at a 5x final concentration were diluted in HBSS-H supplemented with 0.2% BSA. Fluorescence readings were collected using the FlexStation plate reader with excitation at 485 nm, emission at 535 nm and dichroic mirror at 525 nm. The FlexStation took measurements over a 100 second time course, with 10 µL of ligand added to the cells 20 seconds after the start of measurement. Relative fluorescence units (RFU) are reported as the peak magnitude signal subtracted by the basal signal in each well.

2.2.6 Lipids and Buffer N Preparation

DOPC and DOPS chloroform solutions are added to a previously tared round bottom flask separately. Chloroform solutions are gently swirled under an argon stream to evaporate the solvent and leave a thin and uniform lipid film. Round bottom flasks are placed inside a rotovap to evaporate the remaining chloroform under vacuum. Flasks are re-weighted to determine the total weight of the lipids. 10% DDM solution is added to the lipids to bring them to 1% (w/v) final concentration. Solutions are then repeatedly freeze-thawed in liquid nitrogen-warm water to bring the lipids into solution. Lipids are stored at -20 °C for long-term storage. To prepare Buffer N, a solution containing 100 mM HEPES pH 7.4, 0.5 M $(NH_4)_2SO_4$, 5 mM $CaCl_2$, and 25 mM $MgCl_2$ is added to a 50 ml vessel. Glycerol is then added to a final concentration of 10% (v/v) along with the lipids and detergents to the desired concentration. Lipids and detergents have been previously normalized to ensure that the total detergent concentration does not exceed the desired final concentration. The solution is brought to 50 ml total volume with Millipore grade water and then filtered using a 0.45 μm vacuum filter unit. Buffer N is stored at -20 °C for long-term storage.

2.2.7 Expression, Labeling, and Purification of CCR5-SNAP

To purify CCR5-SNAP, we employed a tandem affinity purification protocol employing the FLAG and 1D4 epitopes to remove receptor truncations (Figure 2.2.8). 10 100mm x 20mm polystyrene dishes are plated with HEK293T cells at $4.0x10^6$ cells/dish in DMEM

+ FBS. 24 hours post-plating, 100 µl of Plus Reagent is mixed with 80 µg of CCR5-SNAP in 7.5 ml of DMEM. In a separate vessel, 170 µl of lipofectamine reagent is mixed with 5 ml of DMEM. After 15 minutes, the transfection solutions are mixed and incubated for 15 minutes. Media is removed from HEK293T cells and supplemented with 2.8 ml of DMEM. 1.2 ml of the transfection solution is added to each plate and the cells are incubated for 4 hours before supplementing the media with 4 ml of DMEM + 20% FBS. 24 hours post-transfection, media is removed from the cells and cells are harvested in 2 ml/dish of PBS and 1 mM phenylmethylsulfonyl fluoride (PMSF). Cells are pelleted in a 50 ml vessel at 1,500 rpm using a Beckman GS-6R centrifuge at 4 °C for 5 minutes. The harvesting solution is removed and the cell pellet is solubilized in 5 mls of Buffer L (20 mM HEPES pH 7.4, 0.1 M $(NH_4)_2SO_4$, 1 mM $CaCl_2$, 5 mM $MgCl_2$, 10% Glycerol, 0.1% CHS, 1.0% DDM, 1.0% CHAPS) supplemented with a protease inhibitor cocktail for 2 hours at 4 °C. Cell lysates are then centrifuged at 55,000 rpm for 30 minutes, 4 °C, using a TLA 100.3 rotor. The supernatant was added to 600 µl of 50% slurry 1D4 mAb Sepharose 2B resin and incubated overnight at 4 °C. Resin is pelleted in a GS-6R for 5 minutes, 2,000 rpm, 4 °C and then transferred to a Ultrafree-MC-HV Durapore PVDF 0.45 µm centrifugal unit. CCR5-SNAP was labeled in 400 µl of buffer N (20 mM HEPES pH 7.4, 0.1 M $(NH_4)_2SO_4$, 1 mM $CaCl_2$, 5 mM $MgCl_2$, 10% Glycerol, 0.07% CHS, 0.33% DDM, 0.33% CHAPS, 0.018% DOPC, 0.008% DOPS) with 50 µM SNAP-substrate and 1 mM DTT for 30 minutes at R.T. Resin was then washed 3 x 0.5 ml in Buffer N for 30 minutes each at 4 °C. CCR5-SNAP was eluted from the 1D4 resin by incubating the sample with 1D5 peptide in Buffer N (0.33 mg/ml) twice for 30 minutes on ice and eluting by centrifugation. 1D4 purified CCR5-SNAP was added to 100 µl of

FLAG M2 resin and incubated overnight at 4 °C. FLAG resin was transferred to a separate Durapore spin filter and washed 3 times with 0.5 ml of Buffer N for 30 minutes each at 4 °C. CCR5-SNAP was eluted by incubating the resin twice with 100 µl of buffer N and FLAG peptide (200 µg/ml) 30 minutes on ice. FLAG purified CCR5-SNAP was loaded into a Superdex 200 10/300 GL column previously equilibrated with Buffer N and 0.1 mg/ml BSA (IgG free). CCR5-SNAP was eluted over 1 column volume into 0.5 ml fractions. Western immunoblotting and fluorescence correlation spectroscopy were employed to analyze the SEC fractions.

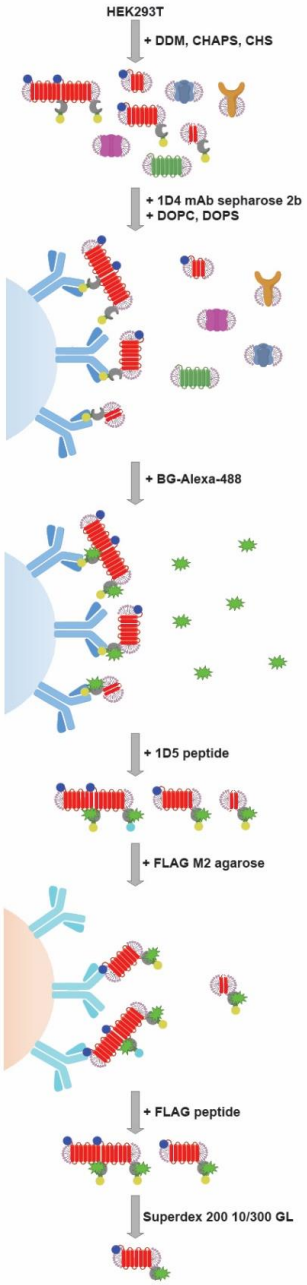

Figure 2.2.8. Schematic displaying the tandem affinity protocol developed to purify full length, monomeric CCR5-SNAP from mammalian cells.

2.2.8 Immunostaining and TIRF microscopy

HEK293T cells were plated onto 35 mm glass bottom (1.5) Matek plates at 300,000 cells per dish. Cells were transfected with CCR5 W.T. at 0.75 µg or CCR5-SNAP at 0.2 µg or pCDNA3.1+ at 2.0 µg at a total DNA/dish of 2.0 µg using Lipofectamine 2000 per manufacturer's instructions. 24 hours post-transfection, media was aspirated from the plates and cells washed with 1 x 2 ml of PBS supplemented with Ca and Mg (Ca/Mg). Cells were then permeabilized with 1 ml of cold methanol for 5 minutes at -20 °C. Cells were then washed 3x1 ml of cold PBS (Ca/Mg) before blocking overnight in 0.5% BSA in PBS (Ca/Mg) at 4 °C. Blocking solution was removed and 1D4 monoclonal antibody at a dilution of 1:2,000 in 0.5% BSA-PBS (Ca/Mg) was added for 1 hour at room temperature. Cells were then washed with 3x1 ml of PBS (Ca/Mg). Secondary antibodies conjugated to Alexa-488 were added at a final dilution of 1:500 in 0.5% BSA-PBS (Ca/Mg) for 1 hour at room temperature. Cells were washed again 3x1 ml of PBS (Ca/Mg) and then LiCor mounting media containing DAPI was added to the cells. Cells were visualized on a Nikon TiE inverted TIRF-FLIM microscope using an Apo TIRF 100x oil N2 objective (N.A. 1.49). Images were collected on an Andor NEO sCMOS camera using 405 and 488 nm excitation with a total exposure of 150 ms per image. Images were acquired at room temperature using the following dimension order, XYCZT, which are 2048, 2048, 3, 1, 1 pixels respectively. Filters used were 525/50 and 450/40. Images were processed using ImageJ and Adobe Illustrator.

2.2.9 SDS-PAGE Analysis and Immunoblotting

Samples were mixed with DTT at 150 mM final concentration and NuPAGE loading buffer. Samples were loaded into a NuPAGE 4-12% Bis-Tris gel in MES-SDS buffer. Electrophoresis was conducted at a constant voltage of 115V. The gel was removed from the cassette and rinsed in water before equilibrating in Western Transfer buffer (48 mM Tris, 39 mM glycine, 1.3 mM SDS, 20% methanol, pH 9.2). 1 piece of Immobilon PVDF membrane-Fl was incubated for 1 minute at room temperature in 100% methanol. The PVDF membrane and 2 pieces of extra thick blot papers (Bio-rad) were rinsed in Western transfer buffer. Western transfer was performed in a semi-dry apparatus for 45 minutes with a constant voltage of 18V. After electrophoresis, the membrane was placed in 10 ml of Odyssey blocking buffer (PBS) and incubated for 1 hour at room temperature. The membrane was then placed in 10 ml of blocking buffer with anti-1D4 mouse monoclonal (1:1,000), anti-FLAG rabbit polyclonal (1:1,000) antibodies, and 0.2% Tween-20. The membrane was incubated overnight at 4 °C. Membrane was then washed 5x5 minutes in 1x PBS-T (0.1% Tween-20). Membrane was incubated for 1 hour at room temperature in 10 ml blocking buffer supplemented with 0.2% Tween-20, 0.01% SDS, goat anti-mouse IR 680 RD (1:10,000), and goat anti-rabbit IR 800 CW (1:10,000). Membrane was washed again 5x5 minutes in 1x PBS-T and then 2x5 minutes in 1x PBS buffer. Membranes were visualized using a LICOR Odyssey SA using 100 μm resolution, and intensity level 7 for both 700 and 800 nm excitations. Images were processed using Image Studio Lite Version 4.0 and ImageJ. For the line scan analysis, a rectangle of 45 x 120 pixels was drawn around the desired gel lane and set as First Lane under Analyze,

Gels, in ImageJ. The command 'Plot Lanes' was then selected with vertical and horizontal scale factors set to 1.0 with uncalibrated optical density. Using the magic wand, an area under the curve was selected and saved as x and y coordinates for replotting in GraphPad Prism 7.

2.2.10 Fluorescence Correlation Spectroscopy Measurements

Samples were loaded into # 1.5 glass bottom 96 well black plate (Senso plates, black, 384 well reference number: 788892, 96-well plate reference number: 655892) and mounted in an inverted laser scanning confocal microscope LSM 780 (Zeiss). Alexa-488 was excited using an Argon 488 nm laser at 0.2% laser transmission. Laser excitation was focused into the sample by using a 40x C-Apochromat NA 1.2 water immersion objective. Correction collar was adjusted in the objective to 0.17 and room temperature. To prevent deformation of the PSF due to glycerol in the solution, the excitation volume was focused 50 µm above the glass by performing a line scan using reflected light from the 488 nm laser line. For 488 nm excitation, a 488 only main beam splitter (MBS) was used. Emission from Alexa-488 was collected in the range of 516 – 596 nm using a GaAsP detector. Pinhole was set to 1.0 airy unit and aligned along the xy plane using a solution of free dye. Count-rate binning time was set to 1 ms and the correlator binning time was set to 0.2 µs. Count rates were never greater than 500 kHz and traces showing large deviations from the average or decaying/increasing fluorescence were manually removed from the analysis. Counts per molecule (CPM) values were between 1-16 kHz for all measurements to avoid optical saturation while maximizing counts above background.

For each single sample, data was collected in 10 repetitions of 10 seconds each and averaged after removing traces that contained large deviations from the average. FCS data analysis and concentration derivations were performed as described in section 3.2.2 and 3.2.7

2.3 Results

2.3.1 CCR5-SNAP Cloning and Sequence

CCR5-SNAP was successfully generated from the parent plasmid DNA containing CCR5. Our initial construct did not encode for the FLAG and signal peptide sequences. Also, we did not have restriction sites that we could use to swap the SP-FLAG sequence into CCR5-SNAP. We did not introduce new restriction sites since it would require various steps and the method would be time consuming. Instead, we employed a cloning method that does not rely on restriction enzyme or DNA ligation to introduce the SP-FLAG sequence into CCR5-SNAP.[59] The method relies on PCR amplification of a 'megaprimer' containing the desired sequence to be inserted and the parent DNA sequence. The parent DNA and 'megaprimer' sequences must have homologous end DNA sequences for the insertion to be successful. The PCR reaction is slightly modified from the Quickchange mutagenesis protocol to allow efficient insertion of the megaprimer sequence. We generated SP-FLAG-CCR5 from which we inserted the into a plasmid backbone to replace CCR5 and generate SP-FLAG-CCR5-SNAP. For this step, we employed restriction enzymes and DNA ligation since the sites between DNA

sequences were compatible. We sequenced both SP-FLAG-CCR5 and CCR5-SNAP (end-product) and we verified that the coding sequence remained intact. Figure 2.3.1 shows a schematic of CCR5-SNAP and the functional tags fused to the N- and C-terminal ends of the receptor.

Figure. 2.3.1. CCR5-SNAP sequence and functional tags fused to human CCR5. Schematic showing the different functional tags fused to the codon optimized human CCR5 gene (blue cylinder) and their amino acid positions. The signal peptide (violet ellipse) was incorporated for receptor cell surface trafficking, FLAG (cyan cylinder) and 1D4 (green cylinder) epitopes for affinity purification, double OLLAS (orange cylinders) and Strep-III (red) tags for surface immobilization, and SNAP tag (yellow hexagon) for covalent attachment of fluorophores.

2.3.2 CCR5-SNAP Cell Surface Expression Quantification

We characterized CCR5-SNAP in HEK293T cells to demonstrate that the functional tags did not interfere with receptor cell surface expression. CCR5-SNAP and WT CCR5 cell surface expression levels were quantified by flow cytometry using different epitope recognizing antibodies conjugated to PE (Figure 2.3.2).

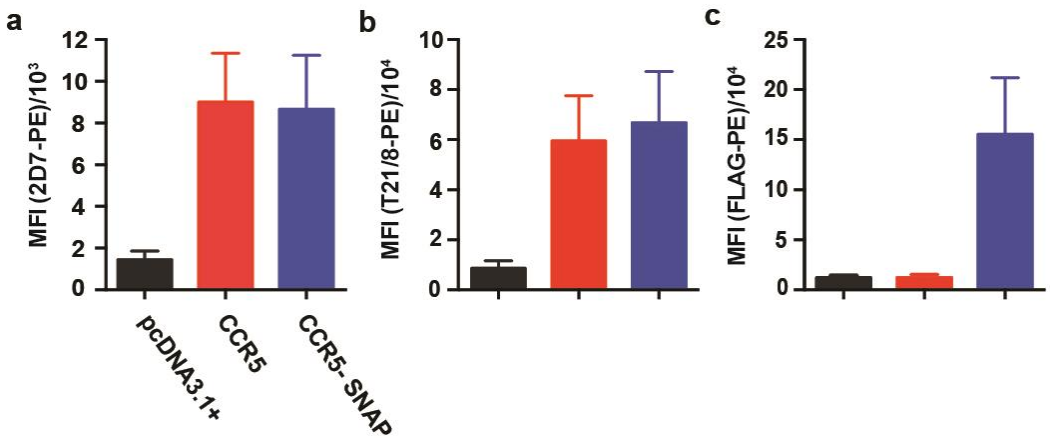

Figure 2.3.2 Cell surface quantification by flow cytometry of wild-type CCR5 and CCR5-SNAP in HEK293T cells stained with (**a**) anti-CCR5 (clone 2D7); (**b**) anti-FLAG or (**c**) anti-CCR5 (clone T21/8) coupled to phycoerythrin (PE). Data are mean of four independent experiments ± S.E.M.

We employed the conformational sensitive 2D7 mouse monoclonal antibody, which recognizes the second extracellular loop (ECL2) of CCR5. 2D7-PE staining shows that wild-type CCR5 and CCR5-SNAP express at similar levels in HEK293T cells under the transfection conditions tested (a). Since the N-terminus of CCR5-SNAP is fused to the FLAG tag sequence, we tested the mouse monoclonal antibody T21/8-PE to show that the N-terminus could be recognized. T21/8-PE staining shows that the FLAG tag does not interfere with CCR5-SNAP recognition and that CCR5-SNAP express at similar levels as wild-type in agreement with the 2D7-PE detection (b). We also tested recognition of CCR5-SNAP with anti-FLAG-PE as a positive control since the antibody is not conformationally sensitive. Figure 2.3.2c shows that the anti-FLAG-PE does recognize CCR5-SNAP but not CCR5 as expected.

2.3.3 CCR5-SNAP Expression Characterization in Cells

To validate the flow cytometry results, we performed TIRF imaging on HEK293T cells expressing CCR5 or CCR5-SNAP and stained with anti-1D4 antibody and Alexa-488 conjugated secondary antibody. Figure 2.3.3 shows representative TIRF images for WT CCR5 and CCR5-SNAP stained in fixed HEK293T cells.

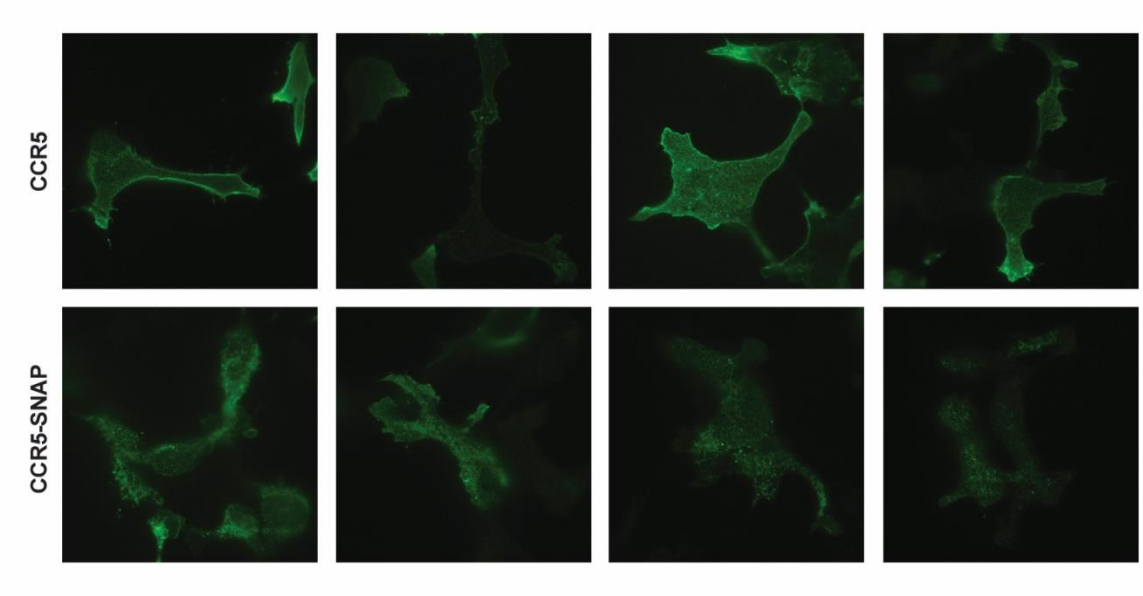

Figure 2.3.3. Fluorescent images of HEK293T cells expressing wild-type CCR5 (**i**) or CCR5-SNAP (**j**) imaged using TIRF microscopy. CCR5 was detected using the anti-1D4 mouse antibody and Alexa-488 conjugated anti-mouse secondary.

We employed TIRF microscopy since only receptor at the plasma membrane will be excited by the evanescent wave. CCR5 and CCR5-SNAP both express at the cell membrane of HEK293T cells and show prototypical membrane distribution observed for

membrane receptors indicating that the functional tags do not perturb receptor cell surface trafficking.

2.3.4 CCR5-SNAP Inhibits cAMP like WT CCR5

We characterized the signaling properties of CCR5-SNAP in comparison to wild-type CCR5 to show that the intracellular tags did not affect coupling to intracellular partners. CCR5 is a $G\alpha_i$ coupled receptor whose activation reduces the levels of cAMP in cells. cAMP levels in cells can be measured using a BRET reporter based on the exchange protein directly activated by cAMP or (EPAC). In the absence of cAMP, the EPAC-BRET reporter is in an open conformation that allows energy transfer between RLuc3 and GFP. cAMP binding to the reporter induces a conformational change that prevents energy transfer and a reduction in BRET is observed. We generated dose response curves for CCR5 and CCR5-SNAP expressed in HEK293T cells with the EPAC-BRET reporter in response to different concentrations of chemokines (Figure 2.3.4)

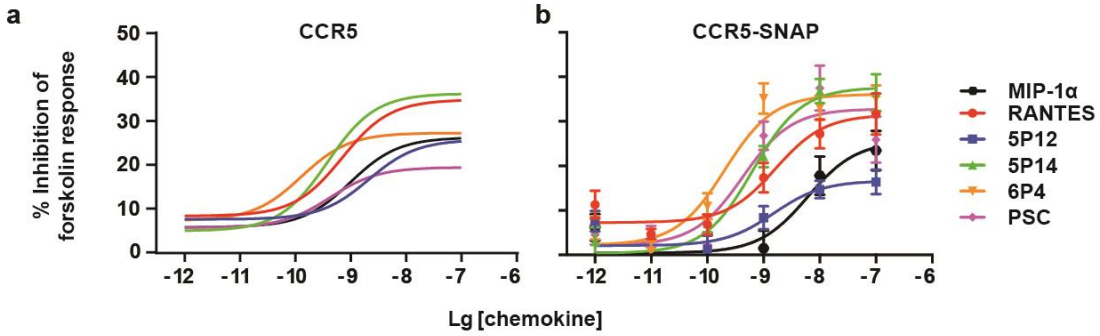

Figure. 2.3.4 Percent inhibition of forskolin-induced cAMP production by wild-type CCR5 (**d**) and CCR5-SNAP (**e**) in response to increasing concentrations of MIP-1α (black), RANTES (red), 5P12 (blue), 5P14 (green), 6P4 (yellow), and PSC (violet). Fits are only shown for wild-type CCR5 as a direct comparison (Lorenzen et al.). Data points are mean from 3 independent experiments performed in triplicate ± S.E.M.

Dose response curves were fitted to a 3-parameter logarithmic equation to derive logEC50 and E_{max} values (Table 2.3.4). Chemokines inhibited cAMP production with similar efficacies and potencies in CCR5-SNAP and CCR5 expressing cells indicating that CCR5-SNAP can signal through $G\alpha_i$ as wild-type CCR5. We did observe that 6P4 and PSC had higher ΔE_{max} values at CCR5-SNAP (34 ± 1 and 31 ± 7 respectively) than at wild-type CCR5 (20 ± 1 and 17 ± 3 respectively).

Table 2.3.4 Fitted parameters to the dose response curves generated for CCR5 and CCR5-SNAP to varying concentrations of chemokines. Dose response curves for cAMP inhibition were fitted in Origin with a three-parameter logistic equation. Values are the average from three independent experiments ± S.E.M.

	cAMP inhibition				
Receptor	**Ligand**	**N**	**IC50 (nM)**	**pIC_{50} ± S.E.M.**	**ΔE_{max} ± S.E.M.**
CCR5	RANTES	3	0.8	-9.2 ± 0.2	26 ± 2
	MIP-1α	3	1.3	-9.3 ± 0.5	21 ± 4
	5P12-RANTES	3	2.4	-8.7 ± 0.1	17 ± 6
	5P14-RANTES	3	0.5	-9.4 ± 0.2	32 ± 3
	6P4-RANTES	3	0.1	-9.9 ± 0.1	20 ± 1
	PSC-RANTES	3	0.7	-9.2 ± 0.1	17 ± 3
CCR5-SNAP	RANTES	3	1.7	-9.8 ± 0.1	24 ± 5
	MIP-1α	3	8.8	-8.2 ± 0.2	24 ± 7
	5P12-RANTES	3	1.9	-8.9 ± 0.3	15 ± 3
	5P14-RANTES	3	0.9	-9.2 ± 0.2	38 ± 6
	6P4-RANTES	3	0.2	-9.7 ± 0.1	34 ± 1
	PSC-RANTES	3	0.4	-9.4 ± 0.1	31 ± 7

2.3.5 CCR5-SNAP Induces Calcium Mobilization Like WT CCR5

We also tested CCR5-SNAP capability to induce calcium mobilization in HEK293T cells using the G-protein chimera $G\alpha_{qi5}$ which has the last five C-terminal amino acids from $G\alpha_i$ in $G\alpha_q$. Cells expressing CCR5 or CCR5-SNAP were treated with the FLIPR calcium 6 dye which becomes fluorescent after chelating calcium ions. Dose response curves for CCR5 and CCR5-SNAP were generated in response to different concentrations of chemokines and fitted to a three-parameter logarithmic equation (Figure 2.3.5.)

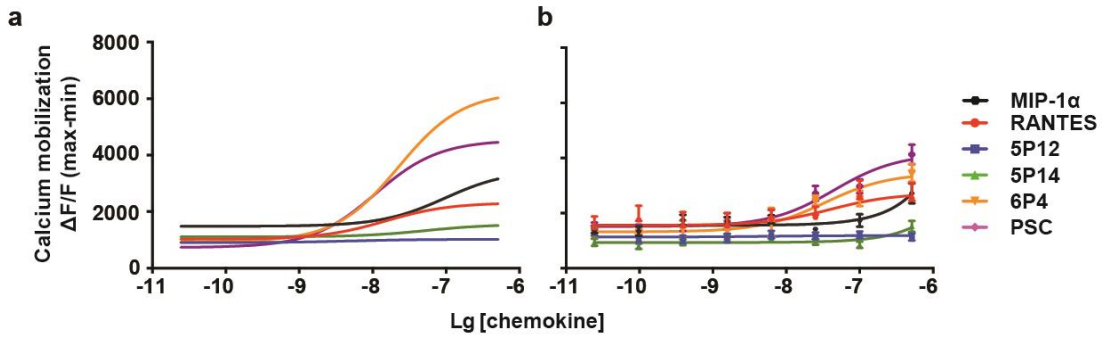

Figure 2.3.5 Calcium flux by wild-type CCR5 (**a**) and CCR5-SNAP (**b**) in response to increasing concentrations of the indicated native and chemokine analogues. Data points represent the mean maximum fluorescence minus basal fluorescence from 3 independent experiments in triplicate ± S.E.M.

CCR5 and CCR5-SNAP did not induce calcium mobilization when stimulated with 5P12 or 5P14. CCR5-SNAP did not respond to MIP-1α and showed lower potencies to RANTES (40 nM) and PSC-RANTES (45 nM) as compared to wild-type CCR5 (14 and 11 nM respectively, Table 2.3.5) Overall, CCR5-SNAP is capable of recognizing G-proteins and activate different signaling pathways indicating that the intracellular tags do not affect G-protein coupling and activation.

Table 2.3.5 Fitted parameters to the dose response curves generated for CCR5 and CCR5-SNAP to varying concentrations of chemokines. Dose response curves for calcium flux were fitted in Origin with a three-parameter logistic equation. Values are the average from three independent experiments ± S.E.M. ND (not determined) is reported for when the fit did not converge.

	Calcium flux				
Receptor	**Ligand**	**N**	**EC50 (nM)**	**pEC_{50} ± S.E.M.**	**E_{max} ± S.E.M.**
CCR5	RANTES	3	14	-7.8 ± 0.2	13000 ± 1600
	MIP-1α	3	96	-7.0 ± 0.3	20000 ± 3900
	5P12-RANTES	3	ND	ND	ND
	5P14-RANTES	3	ND	ND	ND
	6P4-RANTES	3	23	-7.6 ± 0.1	53000 ± 2600
	PSC-RANTES	3	11	-7.9 ± 0.1	38000 ± 2200
CCR5-SNAP	RANTES	3	40	-7.3 ± 0.4	12000 ± 3000
	MIP-1α	3	ND	ND	ND
	5P12-RANTES	3	ND	ND	ND
	5P14-RANTES	3	ND	ND	ND
	6P4-RANTES	3	34	-7.5 ± 0.3	21000 ± 3400
	PSC-RANTES	3	45	-7.4 ± 0.2	26000 ± 3300

2.3.6 CCR5-SNAP Tandem Affinity Purification

To evaluate the tandem affinity purification procedure, we analyzed the purity of the cell lysate, 1D4, and FLAG elution fractions by near-infrared (NIR) fluorescent western immuno-blotting (Figure 2.3.7). We employed NIR detection because it provides higher sensitivity than chemiluminescence detection, signals are linearly proportional to protein amount, and multiple antibodies can be used simultaneously. The 680-nm emission, red color, is from detection of the 1D4 epitope and the 800-nm emission, green color, is from detection of the FLAG tag in the receptor.

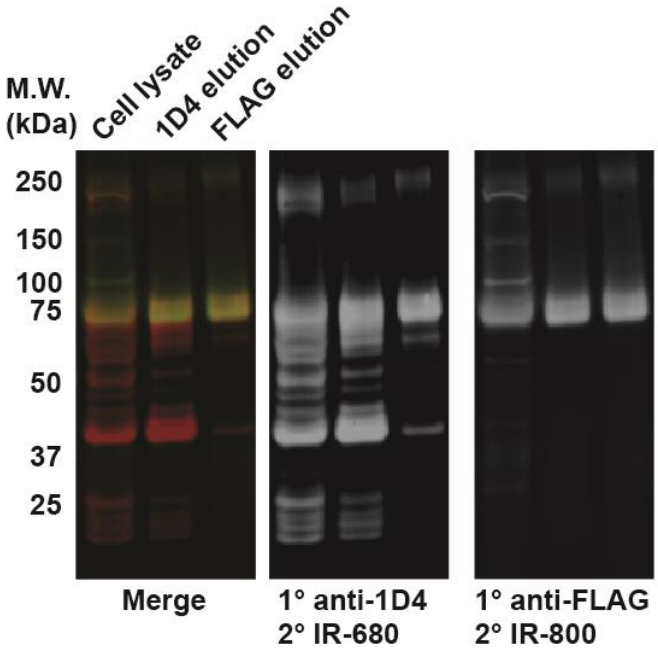

Figure 2.3.6 Reducing SDS-polyacrylamide gel electrophoresis and near-infrared fluorescent western blot of cell lysate (left lane), 1D4 elution (middle lane), and FLAG elution (right lane) from tandem affinity purification. Full-length CCR5-SNAP (~75 kDa, yellow band) was detected using antibodies against the 1D4 and FLAG epitopes and 680 nm (middle panel) and 800 nm (right panel) fluorescent secondary antibodies.

CCR5-SNAP runs with an apparent molecular weight of ~75 kDa which is the prominent yellow band in all 3 lanes. Cell lysate fraction shows the presence of several receptor N-terminal truncations that are 1D4 only positive and run below 75 kDa. We also observe the presence of CCR5-SNAP dimers at 150 kDa and higher order oligomers around 250 kDa. After 1D4 affinity purification, we observe that most receptor N-terminal truncations and oligomers co-elute with the monomeric receptor. However, we can purify away most of the receptor truncations after FLAG affinity purification as shown by their

absence in the FLAG elution fraction. We also observe CCR5 oligomers in the FLAG elution fraction and their presence can complicate the analysis of single molecule measurements. Therefore, we employed SEC to purify the monomeric receptor from these receptor oligomers.

2.3.7 SEC Purification and Concentration Quantification by FCS

We employed SEC to purify the monomeric receptor from these receptor oligomers. We injected the FLAG elution into a Superdex 200 10/300 GL column and protein elution was monitored by adding IgG- and detergent-free bovine serum albumin (BSA) to the sample. Figure 2.3.8 shows the 280 nm absorbance chromatograph (blue line) for fractions 20 to 30.

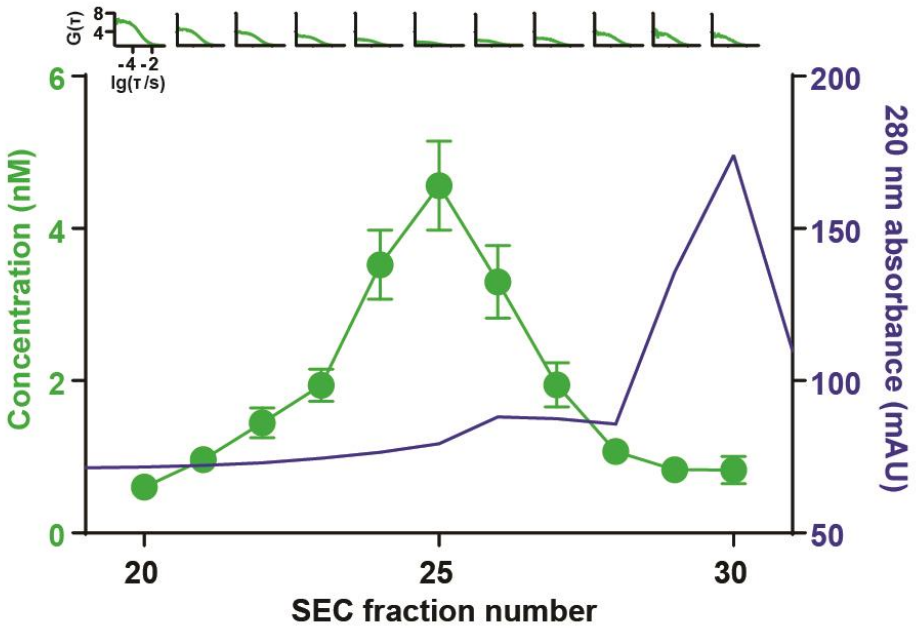

Figure 2.3.7 Size exclusion purification chromatograph (SEC) of CCR5-SNAP-488. Protein elution was monitored using 280 nm absorbance (blue). Fractions 20 to 30 were analyzed by FCS (top inset) to derive concentrations for each fraction (green). FCS autocorrelation traces for representative fractions are shown in the top inset. We averaged concentrations from 5 independent purifications and are shown alongside the 280 nm absorbance chromatograph as the green line where the errors bars are the S.E.M. The FCS-derived chromatograph shows that the receptor peak fraction is in fraction 25 and the average concentration is 4.5 ± 0.6 nM per purification.

2.3.8 Western Immunoblot of CCR5-SNAP SEC Fractions.

We also analyzed fractions 20 to 30 by NIR western immunoblotting to determine where monomeric CCR5-SNAP-488 eluted and the purity of the fraction. Figure 2.3.9 shows the overlay from 680 and 800 nm fluorescence and the independent fluorescence channels.

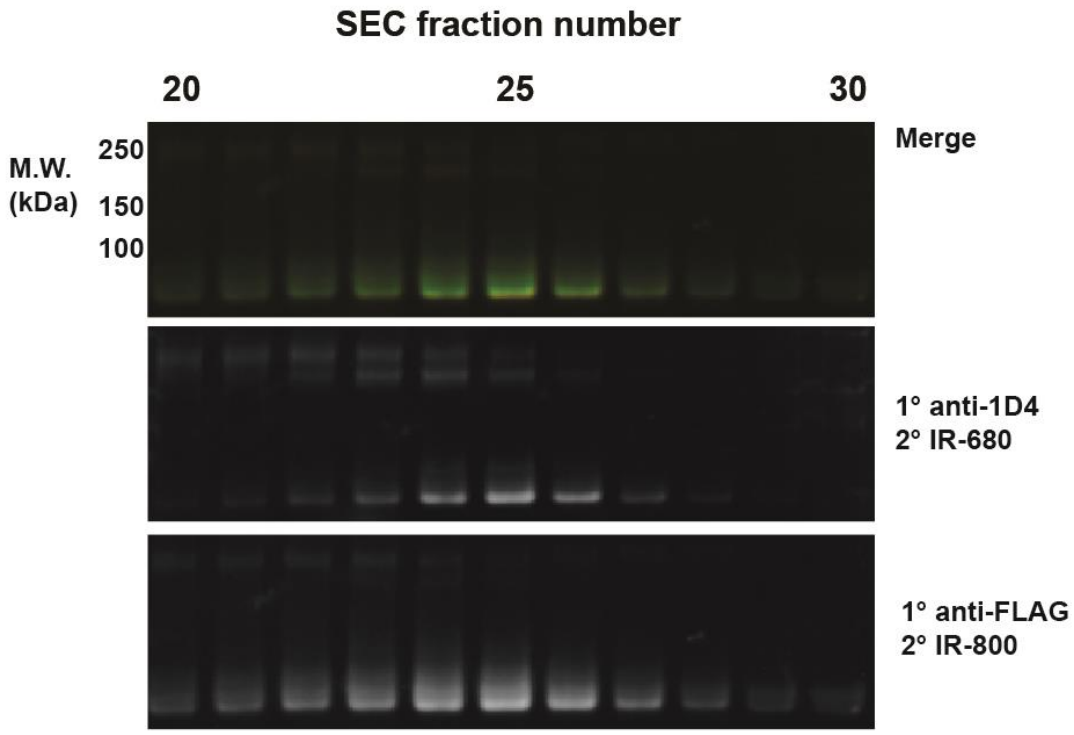

Figure 2.3.8 Reducing SDS-polyacrylamide gel electrophoresis and near-infrared fluorescent western blot of SEC fractions 20 to 30. CCR5-SNAP-488 was detected using antibodies against the 1D4 and FLAG epitopes and 680 nm (middle panel) and 800 nm (right panel) fluorescent secondary antibodies.

Monomeric CCR5-SNAP-488 elutes in all fractions but CCR5-SNAP-488 oligomers are only present in fractions 20 to 24. Fractions 25 to 27 contain only monomeric CCR5-SNAP-488 and these fractions were employed for single molecule FCCS ligand binding measurements.

2.4 Discussion

2.4.1 CCR5-SNAP Cell Surface Expression

We proceeded to characterize CCR5-SNAP in cell-based functional assays to determine if the functional tags affect receptor activity. We normalized receptor expression levels by varying the DNA amount used for transient transfection. We had previously observed that different expression levels resulted in shifts in efficacy and potency in cAMP inhibition experiments (data not shown). We found that 0.75 μg of CCR5-SNAP yielded similar receptor expression as 2.0 μg of CCR5. We employed these DNA quantities for all receptor characterization experiments. We expressed CCR5-SNAP and wild-type CCR5 for 24 hours in HEK293T cells since longer incubation times severely affected receptor expression and function. We were concerned that the FLAG tag may interfere with ligand recognition so we performed flow cytometry experiments using the conformationally sensitive 2D7 antibody to quantify CCR5-SNAP cell surface expression.[60] We did not observe any differences in CCR5-SNAP and wild-type CCR5 cell surface expression in HEK293T cells with 2D7-PE. Chemokines also bind to the receptor N-terminus and the FLAG tag is positioned upstream the N-terminus.[61] Given this, we repeated the flow cytometry measurements but we used the T21/8 antibody, which recognizes the receptor N-terminus. As before, we did not observe any differences between CCR5-SNAP and wild-type CCR5 expression levels with the T21/8-PE antibody. We also did not observe any differences in total fluorescence between the T21/8-PE stained samples and the 2D7-PE samples. We also tested the FLAG-PE antibody on CCR5-SNAP and CCR5 expressing cells as a control experiment. We

detected CCR5-SNAP with the FLAG-PE antibody while we did not observe fluorescence above background from either the mock or wild-type CCR5 cells.

2.4.2 CCR5-SNAP Coupling to G-Proteins

We determined CCR5-SNAP capacity to inhibit cAMP production after chemokine stimulus. CCR5 couples to $G\alpha_i$, which regulates adenylyl cyclase activity in cells. We employed the EPAC-BRET reporter to measure cAMP levels before and after chemokine stimulus.[62] We tested the RANTES analogues and the native chemokines RANTES and MIP-1α at increasing concentrations to generate dose-response curves for cAMP inhibition. To induce production of cAMP, cells were treated with the diterpene Forskolin that activates adenylyl cyclase. Lorenzen (2017) systematically analyzed biased agonism by the RANTES analogues on CCR5 and we based our wild-type CCR5 results from this study. CCR5-SNAP inhibited cAMP production with similar efficacy and potencies as wild-type CCR5 with the tested chemokines. The result shows that the intracellular functional tags do not interfere with receptor coupling and activation of $G\alpha_i$ in HEK293T cells. Surprisingly, 5P12 and 5P14 inhibited cAMP production even though they are presumed to not activate G-protein. Puzzled by these findings, we tested the chemokines in a different assay that measures calcium levels after ligand stimulation. We employed the G-protein chimera $G\alpha_{qi5}$ which has the last five C-terminal amino acids from $G\alpha_i$ in $G\alpha_q$. $G\alpha_q$ signaling activates calcium channels in the endoplasmic reticulum thereby increasing calcium levels in the cytosol. To measure calcium levels, cells were treated with the calcium cheater, FLIPR calcium dye 6, which becomes fluorescent upon calcium

binding. Dose response curves showed that the chemokines induce activation of $G\alpha_{qi5}$. We observe that the chemokines induce calcium mobilization with similar efficacy and potency at CCR5-SNAP and wild-type CCR5. Our results with the cAMP inhibition and calcium flux assays show that CCR5-SNAP can couple and activate G-protein like wild-type CCR5.

2.4.3 CCR5-SNAP Functional Tags for Purification

We purified Alexa-488 labeled, monomeric human CCR5 from receptor truncations and aggregates for single molecule ligand binding studies. Previous CCR5 purifications reports focused on optimizing detergent conditions to retain CCR5 activity and obtaining homogenous preparations in sufficient quantities for structural studies.[63-65] We focused on maximizing CCR5 homogeneity and purity and optimizing fluorescent labeling in an established detergent system. We employed a combined tandem affinity purification and size exclusion chromatography (SEC) step to yield highly pure monomeric CCR5. CCR5-SNAP expression in HEK293T cells yields several receptor C-terminal truncations that are co-purified during one-step affinity purification. We based the tandem affinity purification method from Kobilka (1995) with two changes: 1) we swapped the hexa-histidine tag in the C-terminus for the 1D4 epitope and 2) we used the serotonin $5HT_3A$ receptor signal peptide from guinea pig while Kobilka utilized the signal peptide from influenza hemagglutinin.[66] The 1D4 epitope is derived from the last 18 C-terminal amino acid residues of Rhodopsin.[67] We employed the 1D4 epitope because it has higher specificity than metal affinity purification and it is compatible with

several detergents types.[68] We chose the $5HT_3A$ receptor signal peptide because Zebrafish odorant receptor expression was increased significantly in HEK293 cells.[56] Mirzabekov (1999) supplemented sodium butyrate in their cell medium to boost expression of CCR5. We tested the effect of sodium butyrate on CCR5-SNAP expression and found negligible expression enhancement (unpublished data).

2.4.4 Analysis of Previous CCR5 Purification Reports

We successfully purified full-length CCR5-SNAP from receptor truncations using the 1D4/FLAG tandem affinity purification. SDS-PAGE and western immunoblot analysis shows that 1D4 affinity purification yields full-length receptor co-purified with FLAG-insensitive truncations of various molecular weights. FLAG purification of CCR5-SNAP 1D4 elution removes these C-terminal receptor truncations yielding only full-length CCR5-SNAP. In contrast, Mirzabekov (1999) and Nisius (2008) employed only C-terminal epitopes for CCR5 affinity purification since they only observe two prominent species in their preparations. Mirzabekov (1999) observes two species that correspond to mature and precursor CCR5, while Nisius (2008) observes monomeric and dimeric CCR5. We attribute these differences in CCR5 preparations due to the different cell lines used by Mirzabekov, canine thymocytes (Cf2Th) cells, and Nisius, insect sf9 cells. We also observe CCR5 dimers and higher order oligomers in the FLAG fraction and we employed SEC to remove these species from monomeric CCR5. Nisius (2008) also employed SEC purification to separate CCR5 monomers and dimers with great success.[64] We differ from their approach in that we supplemented CCR5-SNAP with

BSA to monitor protein elution by 280 nm absorbance since we were working with very small receptor concentrations. Nisius (2008) observed that the total CCR5 population consisted of 50% dimer and 50% monomer species. In contrast, we observe one major peak fraction, fraction 25, in our FCS-derived chromatograph, which corresponds to monomeric CCR5-SNAP. Dimeric CCR5-SNAP elutes in fractions 20-24 but its concentration is too low to be observed as a separate peak by FCS. We speculate that the different monomer/dimer ratios observed are due to different detergents employed that can affect receptor aggregation. We should note that CCR5 oligomerization can also be dependent on cell line used and we cannot rule out an effect from the functional tags employed in both constructs.

2.4.5 CCR5-SNAP Solubilization Conditions

We employed a mixture of DDM, CHAPS, CHS, and the lipids DOPC and DOPS in our purification procedure that retains CCR5 ligand binding activity.[44] Mirzabekov (1999) and Nisius (2008) tested the same detergents for CCR5 solubilization but selected different ones based on conflicting results. They tested Cymal-5 and DDM, which are maltoside-derived detergents that differ in the alkyl chain. Cymal-5 and DDM solubilized CCR5 without affecting receptor binding. Mirzabekov (1999) chose Cymal-5 over other DDM because it has a lower critical micellar concentration than DDM. Nisius (2008) chose FosCholine-12 over Cymal-5 and DDM because it was better at solubilization and preparations were more homogeneous by electron microscopy. Mirzabekov (1999) tested FosCholine-14, which has a longer alkyl chain than FosCholine-12 by 2 carbons, and

observed that it was better at solubilizing CCR5 than Cymal-5 and DDM but it abolished CCR5 binding to 2D7. Nisius (2008) reported a K_D value of 1 μM for RANTES binding to FosCholine-12 solubilized CCR5 by isothermal calorimetry titration (ITC). Navratilova (2005) also observed that CCR5 solubilization with DDM preserved binding to 2D7 better than any other detergent tested. Also, Navratilova (2005) discovered that addition of CHS, DOPC, and DOPS increased 2D7 binding by providing a more native environment than detergent alone. Thus, CCR5 solubilized in DDM containing buffers is in a more native environment which is suitable for single molecule ligand binding measurements.

CHAPTER THREE: FLUORESCENCE CROSS-CORRELATION SPECTROSCOPY

3.1 Introduction

We utilized FCCS to perform saturation and competition binding with Alexa-647 labeled RANTES analogues and CCR5-SNAP-488. Figure 3.1.1 illustrates the type of binding interactions analyzed by FCCS. The blue species represents the membrane receptor embedded in a detergent micelle represent by the yellow torus. On the site opposite ligand binding, the receptor has been fused with a labeling tag, in this case a SNAP tag, represented by the violet circle. The SNAP tag has been labeled with a green fluorophore represented by the green star. The ligand, represented by the orange species, has been labeled with a red fluorophore as shown by the red star. Ligand interacts with the receptor in a 1:1 stoichiometry leading to a double labeled complex. The labeled ligand can be displaced from the binding site by a competing ligand in this case the orange species without the red star.

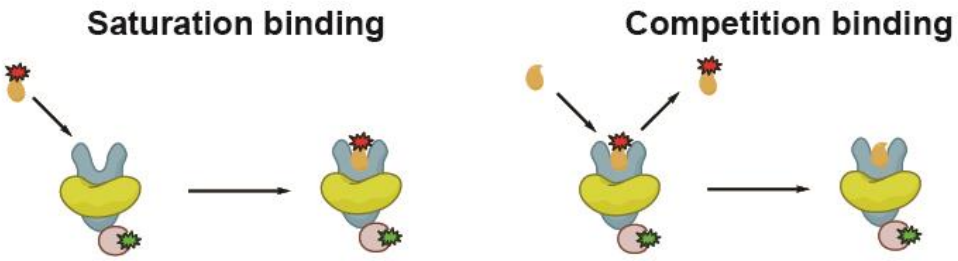

Figure 3.1.1 Schematic showing the binding interactions analyzed by FCCS. Fluorescent ligand (orange ellipse with red star) recognizes a lipid bound (yellow ellipse) membrane receptor (blue species) that has been fused to a functional tag (violet circle) labeled with a fluorophore (green star). Fluorescent ligand binds the receptor (saturation binding) but in the presence of unlabeled ligand it is displaced from the binding site (competition binding).

FCCS measurements are sensitive to refractive index mismatch. The point spread function (PSF) becomes distorted if the refractive index mismatch is large between the immersion solution and the sample. We optimized the imaging optical depth to ensure that we could obtain the maximum count rates from the sample. We also optimized the laser power used for FCCS measurements. Optical saturation distorts the PSF and the assumption that the PSF can be described as a 3D Gaussian is no longer valid. We measured count rates as a function of laser power for Alexa-647, Alexa-488, PSC-647, and CCR5-SNAP-488 to determine the linear range at which we could safely record fluorescence fluctuations. We also determined the cross-talk from the green channel into the red channel. Cross-talk would over-estimate the calculated number of particles for the receptor-ligand complex. We quantified the amount of cross-talk and we found negligible cross-talk in our system. We also quantified the size of the confocal volumes for 488 and 633 nm excitations and the cross-correlation volume to derive concentrations for receptor, ligand, and complex.

We then describe the fitting models we used to model the auto- and cross-correlation traces and the derivation for how K_D and K_i values can be determined from FCCS measurements under ideal situations. We performed saturation ligand binding with the RANTES analogues, native chemokines, and gp120. We show that the RANTES analogues bind with picomolar to nanomolar affinities. We found that 25% of the

receptor is active and within this fraction the analogues bind to 38% with high affinity and the remaining 62% with low affinity. We also performed homologous and heterologous competition binding and show that the unlabeled chemokines bind with similar affinities as the labeled chemokines. We also show that native chemokines and gp120 cannot displace the labeled RANTES analogues from CCR5-SNAP-488. We discuss plausible explanation for the two CCR5-SNAP species and the physiological implications of each hypothesis.

3.2 Materials and Methods

3.2.1 Correlation and Cross-Correlation Settings

Samples were loaded into # 1.5 glass bottom 96 or 384 well black plates (Senso plates, black, 384 well reference number: 788892, 96 well plate reference number: 655892) and mounted in an inverted laser scanning confocal microscope LSM 780 (Zeiss). Alexa-488 was excited using an Argon 488 nm laser at 0.2% or 0.8% laser transmission and Alexa-647 was excited using a Helium-Neon 633 nm laser line at 1.0% laser transmission. Laser excitation was focused into the sample by using a 40x C-Apochromat NA 1.2 water immersion objective. Correction collar was adjusted in the objective to 0.17 and room temperature. To prevent deformation of the PSF due to glycerol in the solution, the excitation volume was focused 50 μm above the glass by performing a line scan using reflected light from the 488 nm laser line. For 488 nm excitation, a 488 nm only main beam splitter (MBS) was used, and for 633 nm and dual excitation a MBS 488/561/633

was used. Emission from Alexa-488 was collected in the range of 516 – 596 nm using a GaAsP detector and emission from Alexa-647 in the range of 650 – 694 nm using a separate GaAsP detector. Pinholes for both excitations were set to 1.0 airy units and aligned along the xy plane using a solution of free dye or the sample itself. Count-rate binning time was set to 1 ms and the correlator binning time was set to 0.2 µs. Count rates were never greater than 500 kHz and traces showing large deviations from the average or decaying/increasing fluorescence were manually removed from the analysis. Counts per molecule (CPM) values were between 1-16 kHz for all measurements to avoid optical saturation while maximizing counts above background. For single dye measurements, 10 repetitions of 10 seconds each were collected and averaged while for receptor-ligand binding experiments 50 repetitions of 30 seconds each were collected and averaged.

3.2.2 Fitting Correlation Traces

FCS and FCCS raw traces were fitted using the ZEN software. Auto- and cross-correlations were analyzed from 2 µs to 10 s to remove after pulsing from the detectors. For the CCR5-SNAP-488 auto-correlation, a single 3D translational diffusing component undergoing triplet state transitions was chosen. The structural parameter was fixed to 8, the gamma factor to 0.35, and the triplet state relaxation time to 4 µs. The correlation function used to model the data is shown below:

$$G_{488}(\tau) = \frac{\gamma}{N}\left(\frac{1}{\left(1+\left(\frac{\tau}{\tau_D}\right)\right)}\frac{1}{\sqrt{1+\left(\left(\frac{w_{xy}}{z}\right)^2\left(\frac{\tau}{\tau_D}\right)\right)}}\right)\left(1+\frac{T_t e^{-\frac{\tau}{\tau_t}}}{1-T_t}\right)+1 \quad \text{(Equation 3.1)}$$

For the ligand-647 auto-correlation, we applied the previous fit with an included independent blinking term. The blinking term was only observed when the ligand was present with CCR5-SNAP-488. The structural parameter was fixed to 8 and the gamma factor 0.35. The correlation function used to model the data is shown below:

$$G_{647}(\tau) = \frac{\gamma}{N}\left(\frac{1}{\left(1+\left(\frac{\tau}{\tau_D}\right)\right)}\frac{1}{\sqrt{1+\left(\left(\frac{w_{xy}}{z}\right)^2\left(\frac{\tau}{\tau_D}\right)\right)}}\right)\left(1+\frac{T_t e^{-\frac{\tau}{\tau_t}}}{1-T_t}\right)\left(1+\frac{T_b e^{-\frac{\tau}{\tau_b}}}{1-T_b}\right)+1 \quad \text{(Equation 3.2)}$$

Triplet and blinking states correlation functions were set to be normalized to calculate the number of particles that are only in the fluorescent state. In some cases, τ_t, was fixed to 7 μs so that the fit will converge.

Cross-correlation functions were analyzed by using a single component with 3D translational diffusion. Triplet states from Alexa-488 and Alexa-647 will not cross-correlate since they are independent processes.

$$G_{CC}(\tau) = \frac{\gamma}{N}\frac{1}{\left(1+\left(\frac{\tau}{\tau_D}\right)\right)}\frac{1}{\sqrt{1+\left(\left(\frac{w_{xy}}{z}\right)^2\left(\frac{\tau}{\tau_D}\right)\right)}}+1 \quad \text{(Equation 3.3)}$$

To derive errors for each measurement, the total repetitions were divided into 3 independent sets of measurements and each set was averaged and analyzed using the equations above. From these 3 averages, the standard deviation was calculated for the number of particles. In cases where $\tau_D complex$ deviate significantly from previously measured values, it was fixed to 550 µs so that the fit would converge.

3.2.3 Focal Depth Optimization for Measurements in Glycerol Solutions

We employ a 40x immersion water objective to record correlation measurements. Buffer N contains 10% glycerol (v/v) to stabilize membrane proteins. FCS and FCCS measurements are best obtained at a focal depth from the glass slide at 200 µm. However, pilot FCS and FCCS measurements in Buffer N solution with fluorophores showed a decay in measured count rates and a larger PSF than the ones calculated on water solutions. We proceeded to optimize the focal depth at which FCS and FCCS measurements at recorded to minimize PSF distortion. We prepared solutions of Alexa-488 and Alexa-647 in Buffer N and Millipore grade water at a final concentration of 1 nM. We imaged the 4 samples per the settings listed in section 3.2.1. For Alexa-488, we used a 1% laser power transmission and Alexa-647 15% laser power transmission.

3.2.4 Laser Power Optimization for 488 and 633 nm Excitations

Triplet state transitions are dependent on laser power but the PSF becomes distorted at high laser powers. As such, the measured count rates will underestimate the true value

and the number of particles will overestimate the true number for the sample. To determine the optimal laser power for 488 and 633 nm laser excitations, we measured laser power as a function of % transmission for both Alexa-488 and Alexa-647. We employed 1 nM solutions of both dyes in Buffer N and Millipore grade water. Count-rates were also measured for Buffer N and water alone to determine the background count-rates. For the CCR5-SNAP-488 and RANTES analogues, we employed 0.5 nM receptor and 1 nM PSC-647 and measure count rates at conditions identical for FCCS measurements. We employed PSC-647 since all the chemokines are labeled at the same site using the same chemistry. We measured count rates as described for the free dyes as well as just Buffer N to derive background count rates.

3.2.5 Confocal Volume Determination

Solutions of Alexa-488 and Alexa-647 were diluted in Buffer N at various concentrations from 25 nM to 0.8 nM. FCS measurements were performed per section 3.2.1 and fitted using the equations on section 3.2.2. Alexa-647 was fitted without the blinking component. Concentrations were plotted as a function of number of particles derived from the fits to the correlation traces. To correct for pipetting errors, Alexa-88 and Alexa-647 stock solutions used for the dilutions (10 μM) were analyzed by UV-Vis to derive real concentrations. Concentrations for the diluted solutions were then corrected by a factor which accounts for deviations from the assumed valued. From the concentration vs. number of particles plot, we derived the slope using LINEST in Microsoft excel and divided the number by Avogadro's number to derive the confocal volume. To calculate

the confocal volume for the CC channel, we employed a dual-labeled oligonucleotide 40 base pairs long with Alexa-488 and Alexa-647 at both ends to minimize FRET. Single strand oligonucleotides were re-suspended in 10 mM Tris pH 8.0, 50 mM NaCl, 1 mM EDTA to a final concentration of 1 μM in 100 μl of buffer. Samples were added to a water bath at 94 °C in a Dewar flask and allowed to anneal until the temperature in the water bath reached less than 40 °C. Oligos were then placed at RT while a C4 column was equilibrated with 0.1 M ammonium acetate pH 6.6. Oligos were loaded into the column and eluted with 50% acetonitrile in water (v/v) by using a 50% gradient of acetonitrile. HPLC fractions were analyzed by UV-Vis absorbance for both Alexa-488 and Alexa-647. The peak fraction was aliquoted into 50 μl aliquots and stored at -20 C for long-term storage. The final concentration of the oligo was 110 nM. Stock solutions were employed to dilute the oligonucleotide as done for the free dyes. The FCCS measurements were done per section 3.2.1, analyzed using the equations in sections 3.2.2 and the confocal volume determined as described previously for Alexa-647 and Alexa-488.

3.2.6 Cross-Talk Determination

Cross-talk from the green channel to the red channel was determined using the protocol by Bacia & Schwille (2007).[52] Briefly, Alexa-488 (25 nM) in Buffer N was excited using 488 nm laser line and the count rates were recorded in GaAsP 1. The same solution was excited with the same laser line but instead count rates were recorded on GaAsP 2, which is used for the red channels. Count rates from these two measurements were used to calculate the bleed-through ratio:

$$\kappa_{Gr} = \frac{F_r^{Calibration}}{F_g^{Calibration}} \qquad \text{(Equation 3.4)}$$

In a sample containing dual-labeled oligonucleotide or CCR5-SNAP-488 and labeled chemokine, the ratio of the measured green and red count rates was taken and then multiplied with the bleed-through ratio calculated previously.

$$\frac{G_{0,\kappa}}{G_{0,g}} = \kappa_{Gr}\left(\frac{F_g}{F_r}\right) \qquad \text{(Equation 3.5)}$$

The value determined above is then compared with Equation 3.6

$$\frac{G_{0,x}}{G_{0,g}} \qquad \text{(Equation 3.6)}$$

Which is the relative cross-correlation not corrected for cross-talk.

3.2.7 Determining Fractional Occupancy from FCCS Measurements

In FCS, fluorescence fluctuations arise from diffusion through the confocal volume ($V_{confocal}$) and changes in concentration. To derive diffusion coefficients and concentrations, a correlation analysis is performed on the fluorescence intensity profile. The autocorrelation function is defined by

$$G(\tau) = \frac{\langle F(t)F(t+\tau)\rangle}{\langle F\rangle^2} \qquad \text{(Equation 3.7)}$$

However, an analytical expression is needed to fit the autocorrelation function to derive parameters such as concentration and diffusion coefficients. For a single fluorescent species undergoing 3D translational diffusion, the autocorrelation function is described by

$$G(\tau) = \frac{1}{N}\frac{1}{\left(1+\left(\frac{\tau}{\tau_D}\right)\right)}\frac{1}{\sqrt{1+\left(\left(\frac{w_{xy}}{z}\right)^2\left(\frac{\tau}{\tau_D}\right)\right)}} + 1 \qquad \text{(Equation 3.8)}$$

Where N is the number of fluorescent particles, w_{xy} is the radius along the xy plane for a 3D Gaussian, z is the radius along the z plane, and τ_D is the diffusion time through $V_{confocal}$ which is related to the diffusion coefficient by

$$\tau_D = \frac{w_{xy}^2}{4D_{coefficient}} \qquad \text{(Equation 3.9)}$$

To derive concentrations from the autocorrelation data, $V_{confocal}$ for any excitation must be known. $V_{confocal}$ is defined by

$$V_{confocal} = \left(\frac{\pi}{2}\right)^2 w_{xy}^2 z \qquad \text{(Equation 3.10)}$$

Concentrations are obtained using $\frac{(N)(V_{confocal})}{N_A}$. Equation 1.1 is changed to account for the two correlating fluorescence intensities

$$G_X(\tau) = \frac{\langle F_G(t)F_R(t+\tau)\rangle}{\langle F_G\rangle\langle F_R\rangle} \text{ (Equation 3.11)}$$

In the case that the sample contains multiple fluorescent species, then the auto-correlation and cross-correlation amplitudes are given by

$$G_j(0) = \frac{\sum_i N_i \eta_{i,j}^2}{(\sum_i N_i \eta_{i,j})^2} \qquad \text{(Equation 3.12)}$$

$$G_X(0) = \frac{\sum_i N_i \eta_{i,g} \eta_{i,r}}{(\sum_i N_i \eta_{i,g})(\sum_i N_i \eta_{i,r})} \qquad \text{(Equation 3.13)}$$

Where $\eta_{i,j}$ defines the molecular brightness for a specific fluorescent component. Let's assume that the $V_G = V_R = V_X$, the molecular brightness $\eta_{i,j}$ of all fluorescent components are identical, and the binding reaction is unimolecular. Then the contributions of each fluorescent species to the auto- and cross-correlation amplitudes are given by

$$G_R(0) = \frac{N_R + N_{GR}}{(N_R + N_{GR})^2} = \frac{1}{N_R + N_{GR}} \qquad \text{(Equation 3.14)}$$

$$G_X(0) = \frac{N_{GR}}{(N_R + N_{GR})(N_G + N_{GR})} \qquad \text{(Equation 3.15)}$$

Where N_R is the number of red-labeled particles, N_G is the number of green-labeled particles, and N_{GR} is the number of dual-labeled particles. If the red-labeled species is the ligand, then the fraction of double-labeled species is given by

$$\frac{G_x(0)}{G_R(0)} = \frac{N_{GR}}{N_G + N_{GR}} \qquad \text{(Equation 3.16)}$$

The ratio shown above is also equal to the fractional occupancy, which is defined as

$$\rho = \frac{[RL]}{[R]} = \frac{[L]}{K_D + [L]} \qquad \text{(Equation 3.17)}$$

Where $[R]$ is the concentration of receptor, $[L]$ is the concentration of ligand, and $[RL]$ is the concentration of receptor-ligand complex. To derive K_i, we begin with equation 3.16 and establish the following relation,

$$\frac{G_x(0)}{G_R(0)} = \frac{V_R}{V_X}\frac{[RL]}{[R_T]} \text{(Equation 3.18)}$$

Where $[R_T]$ is the total concentration of receptor. We then define the following relations,

$$K_D = \frac{L_F R_F}{RL} \qquad \text{(Equation 3.19)}$$

$$K_i = \frac{C_F R_F}{RC} \qquad \text{(Equation 3.20)}$$

Where L_F is the free ligand concentration, R_F is the free receptor concentration, C_F is the free competitor concentration, and RC is the receptor-competitor complex concentration. From these relations, we can assume that free ligand is equal to total ligand concentration and that the free competitor concentration is also equal to the total competitor concentration to derive the following expression for $[R_T]$,

$$R_T = R_F + RC + RL \quad \text{(Equation 3.21)}$$

We can substitute these relations to derive the following expression

$$\frac{G_x(0)}{G_R(0)} = \frac{\frac{L_T R_F}{K_D}}{R_F + \frac{C_T R_F}{K_i} + \frac{L_T R_F}{K_D}} \quad \text{(Equation 3.22)}$$

Re-arranging yields the Cheng-Prussof relation

$$\frac{G_x(0)}{G_R(0)} = \frac{L_T}{K_D\left(1 + \frac{C_T}{K_i}\right) + L_T} \quad \text{(Equation 3.23)}$$

3.2.8 Ligand Binding Measurements

Saturation ligand binding assays were set-up in PCR tubes by serially diluting the ligand in Buffer N supplemented with 0.1 mg/ml BSA (IgG free, detergent free). CCR5-SNAP-A488 was then added in equal volume for a total reaction volume of 20 µl. Samples were equilibrated at room temperature for 4 hours protected from ambient light. 15 µl of each

sample were loaded into individual wells of a 384 well plate previously blocked with 1.0 mg/ml BSA (IgG free, detergent free) in water for 15 minutes at room temperature. To prevent sample evaporation, 5 - 10 µl of paraffin oil was applied to the top of each sample. Competition binding assays were set-up in a similar fashion except that the labeled chemokine was kept at constant concentration and the competitor was serially diluted. 5 µl of the labeled chemokine was mixed with 5 µl of non-labeled chemokine and then 10 µl of CCR5-SNAP-A488 was added for a 20 µl total reaction volume. Samples were equilibrated for ≥16 hours at R.T. before imaging by FCCS. For competition with the sCD4-gp120 complex, sCD4 and gp120 were incubated for 1 hour at a molar ratio of 10:1 respectively and final complex concentration of 20 µM. Complex was then serially diluted in Buffer N prior to adding labeled 5P12- or 6P4-647 and CCR5-SNAP-488. Samples were then incubated for ≥ 16 hours at room temperature prior to FCCS measurements.

3.2.9 Neuraminidase Treatment of CCR5-SNAP and SNAP-CCR5

21 µl of 1D4 and FLAG purified CCR5-SNAP-488 and SNAP-CCR5-647 were mixed with 6 µl of GlycoBuffer1 and 3 µl of α2-3,6,8,9 neuraminidase A in individual PCR tubes. Control samples had 3 µl added of water instead of enzyme. Samples were incubated for 1 hour at RT and then analyzed by SDS-PAGE, NIR western immunoblotting, and line scan analysis in ImageJ as described previously.

3.2.10 Global Fitting Analysis of Binding Curves

We define the following equilibrium expressions for a two-binding site model:

$$K_{D,H} = \frac{L_F R_{F,H}}{RL_H} \qquad \text{(Equation 3.24)}$$

$$K_{D,L} = \frac{L_F R_{F,L}}{RL_L} \qquad \text{(Equation 3.25)}$$

$$K_{i,H} = \frac{C_F R_{F,H}}{RC_H} \qquad \text{(Equation 3.26)}$$

$$K_{i,L} = \frac{C_F R_{F,L}}{RC_L} \qquad \text{(Equation 3.27)}$$

Where $K_{D,H}$ is the equilibrium dissociation constant for the high affinity site, $K_{D,L}$ is the equilibrium dissociation constant for the low affinity site, $K_{i,H}$ is the equilibrium inhibition constant for the high affinity site, $K_{i,L}$ is the equilibrium inhibition constant for the low affinity site, C_F and L_F are the free concentrations of competitor and ligand, respectively, $R_{F.H}$ and $R_{F,L}$ are the free concentrations of receptor for the high and low affinity sites, respectively, RL_H and RL_L are the concentrations of receptor-ligand complex for the high and low affinity sites, respectively, and, RC_H and RC_L are the concentrations of receptor-competitor complex for the high and low affinity sites, respectively. We define the concentration of the high affinity site as

$$f_H * R_T = R_{T,H} \qquad \text{(Equation 3.28)}$$

Where f_H is a number from 0 to 1 to determine the high affinity receptor fraction, R_T is the total receptor concentration, and $R_{T,H}$ is the high affinity receptor fraction. We then define the concentration of the low affinity fraction as follows

$$f_L = 1 - f_H \qquad \text{(Equation 3.29)}$$

$$f_L * R_T = R_{T,L} \qquad \text{(Equation 3.30)}$$

Using these relations, we re-arrange equations 3.24 to 3.27 to yield the concentrations of $R_{T,H}$, $R_{T,L}$, C_T, L_T, RL_T, and R_T

$$R_{T,H} = R_{F,H} + RL_H + RC_H \qquad \text{(Equation 3.31)}$$

$$R_{T,L} = R_{F,L} + RL_L + RC_L \qquad \text{(Equation 3.32)}$$

$$C_T = C_F + RC_H + RC_L \qquad \text{(Equation 3.33)}$$

$$L_T = L_F + RL_H + RL_L \qquad \text{(Equation 3.34)}$$

$$RL_T = RL_H + RL_L \qquad \text{(Equation 3.35)}$$

$$R_T = R_{T,H} + R_{T,L} \qquad \text{(Equation 3.36)}$$

Using the expressions above, we derived the following equations for saturation binding

$$\theta_H = \frac{R_{L,H}}{R_H + RC_H + RL_H} \qquad \text{(Equation 3.37)}$$

$$\theta_L = \frac{R_{L,L}}{R_L + RC_L + RL_L} \qquad \text{(Equation 3.38)}$$

And for competition binding

$$\theta_H = \frac{L_F}{K_{D,H}\left(1+\frac{C_F}{K_{i,H}}\right)+ L_F} \qquad \text{(Equation 3.39)}$$

$$\theta_L = \frac{L_F}{K_{D,L}\left(1+\frac{C_F}{K_{i,L}}\right)+ L_F} \qquad \text{(Equation 3.40)}$$

We then define the following relations for the receptor-ligand complex

$$RL_T = R_{T,H} * \theta_H + R_{T,L} * \theta_L \qquad \text{(Equation 3.41)}$$

Substituting in for the definitions of high and low receptor fractions we derive the following equation

$$RL_T = (f_H * \theta_H + (1 - f_H) * \theta_L) * R_T \qquad \text{(Equation 3.42)}$$

From equation 3.42, we derive the fractional occupancy as follows

$$\frac{RL_T}{R_T} = f_H * \theta_H + (1 - f_H) * \theta_L \qquad \text{(Equation 3.43)}$$

Expanding the relation above yields the following expression

$$\frac{RL_T}{R_T} = f_H * \frac{L_F}{K_{D,H}\left(1+\frac{C_F}{K_{i,H}}\right)+ L_F} + (1 - f_H) * \frac{L_F}{K_{D,L}\left(1+\frac{C_F}{K_{i,L}}\right)+ L_F} \qquad \text{(Equation 3.44)}$$

We employed equation 3.44 to fit both saturation and competition binding isotherms. In the absence of competitor, the equation above reduces to the two binding sites saturation binding equation without ligand depletion. To correct for ligand depletion, we first fit the equation above by setting the concentration of free ligand and competitor equal to the total concentration of ligand and competitor. We then fit iteratively to correct for ligand depletion. The functional form above combined with the iterative fitting allows us to correct for ligand depletion without deriving an analytical solution. We define the chi squared function as follows

$$X^2(p,u) = \sum_{i=1}^{N}[\left(\frac{RL_T}{R_T}\right)_i - f(p, C_{F,i}, L_{F,i}))^2 \qquad \text{(Equation 3.45)}$$

Where $u = \{C_{F,i}\}_{i=1,2,3\ldots N}, \{L_{F,i}\}_{i=1,2,3\ldots N}$. We minimize X^2 with u set to the concentration of ligand and competitor to get an initial solution for $p: p_i$. We then calculate a correction for C_F and L_F from p_i and initial C and L. We repeat the minimization until the correction is smaller than ϵ. We fixed the total active receptor fraction to 25% and performed various binding fits to determine the optimal f_a value. We set f_a to 38% for all fits since this value yielded the best fits from all the different f_a values tested. We set $K_{D,H}$ and $K_{D,L}$ to be free parameters and the values determined from saturation binding are fixed to determine $K_{i,H}$ and $K_{i,L}$ from competition binding assays. To determine errors associated with each affinity, we performed bootstrapping with data re-sampling by replacement. Global analysis with non-linear least square fitting of the binding isotherms yields parameters that describe the complete data set. We repeated the bootstrap resampling 100 times and eliminated cases, 14 out of 100, where the affinities

were for the high and low binding sites are switched. Saturation and competition binding isotherms were normalized and binding isotherms were plotted as a 2D function (ρ, L) or the 3D surface (ρ, C, L) for saturation and competition binding respectively.

3.3 Results

3.3.1 Optical Focus Depth Optimization

We measured count rates for Alexa-488 and Alexa-647 in Buffer N and water to determine at which optical depth we measured the most count rates. Figure 3.3.1 shows plots for Alexa-488 and Alexa-647 as a function of optical depth for solutions containing glycerol (Buffer N) and solutions not containing glycerol (water).

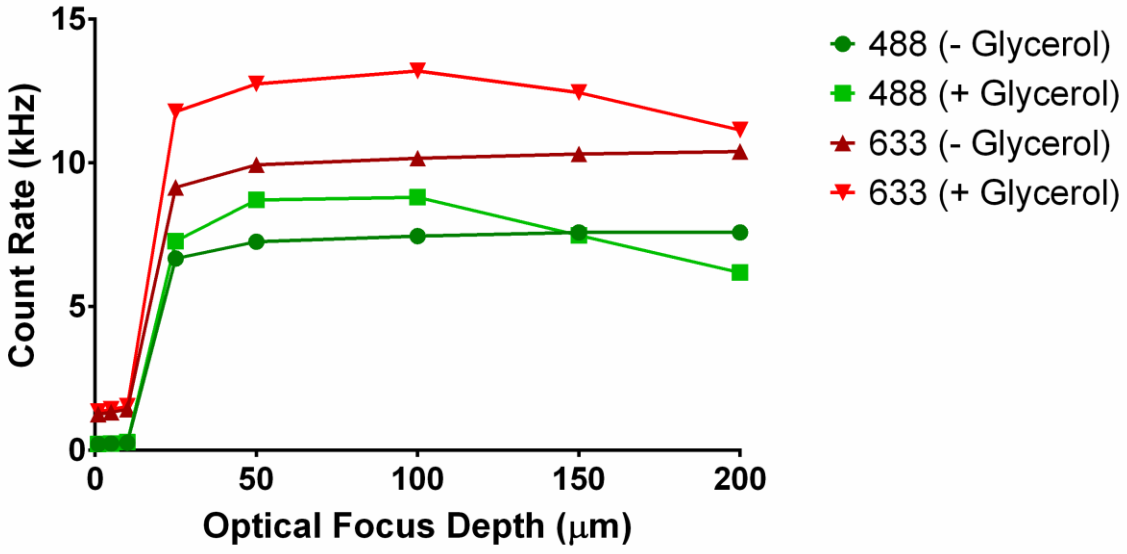

Figure 3.3.1 Optical focus depth optimization for Alexa-488 and Alexa-647 count rates as a function of optical depth.

Alexa-647 is brighter than Alexa-488 at the conditions tested. We did not exceed count rates above 15 kHz because of optical saturation. We observed that the Alexa dyes are brighter in glycerol-containing solutions than water. At depths below 50 μm, we observed no fluorescence from either Alexa dye. We started to observe fluorescence above 25 μm. For both dyes, we observed constant count rates from 50 to 100 μm depth indicating that at this range the PSF was not affected by glycerol. From there on, count rates started to decrease only for the fluorophores in glycerol solutions but not fluorophores in water. Based on these results, we performed all FCS and FCCS measurements at an optical depth of 50 μm.

3.3.2 Laser Power Optimization for 488 and 633 nm Excitations

Count rates were measured for Alexa-488, Alexa-647, CCR5-SNAP-488, and PSC-647 at various laser powers. We also measured background count rates at identical laser powers for Buffer N and/or Millipore grade water. Figure 3.3.2 shows the 4 plots obtained for each experiment conducted where count rates are plotted as a function of laser power.

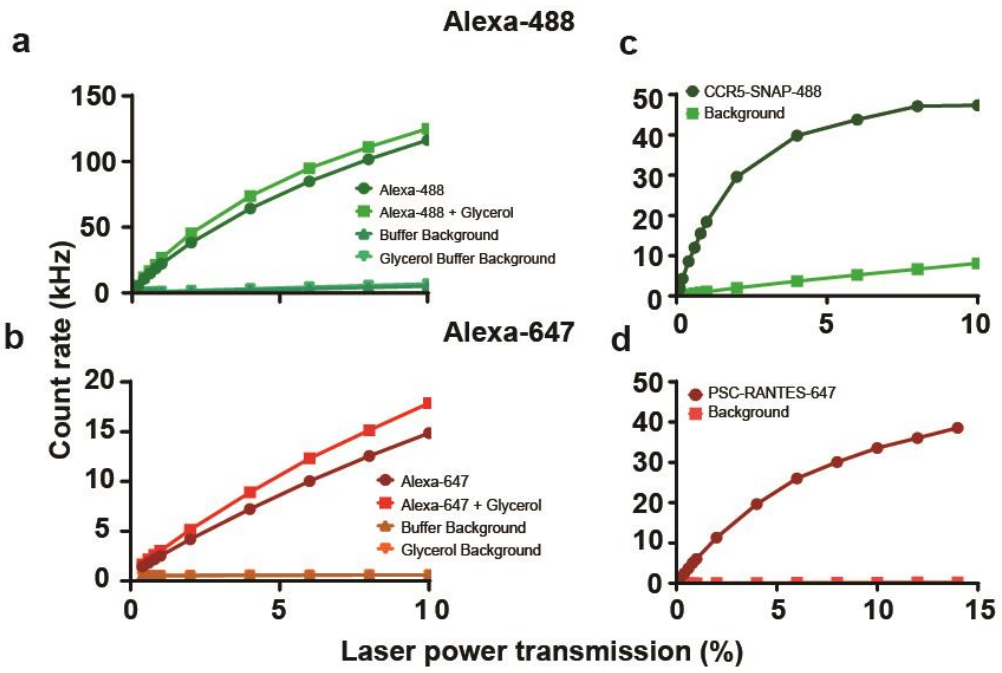

Figure 3.3.2 Count rates determined for Alexa-488, Alexa-647, CCR5-SNAP-488, and PSC-647 at various laser powers and buffer conditions. (a) Alexa-488 count rates for solutions containing glycerol or water. (b) Alexa-647 count rates for solutions containing glycerol or water. (c) CCR5-SNAP count rates determined in Buffer N (d) PSC-647 count rates determined in Buffer N.

We observed a general trend where Alexa-488 or Alexa-647 count rates are linearly dependent on laser power in the range of 0.2-1% laser transmission. The labeled receptor and chemokine saturate faster than the free dyes. We chose laser powers of 0.2% transmission for CCR5-SNAP-488 and 1.0% transmission for PSC-64. At these values, we maximize brightness from the fluorophores without optical saturation. We also chose these values because background contribution to the total fluorescence signal was less than 10%.

3.3.3 Confocal Volume Determination for 488 and 633 nm Excitations

We determined the confocal volumes for 488 nm, 633 nm, and their volume overlap (cross-correlation) using dilution series of Alexa 488, Alexa 647, and a dual labeled oligonucleotide.[69] We plotted the fitted number of particles for each sample vs. the corrected concentration determined from UV-Vis measurements (Figure 3.3.3). To derive the concentration volume, the slope from each curve is divided by Avogadro's number. For each channel, we observed that the number of particles is a linear function of concentration. We did not observe any deviations from the linear trend at low or high concentrations. Deviations at low concentrations are due to background fluorescence overestimating the calculated number of particles. Deviations at high concentrations are due to optical saturation that arise from PSF distortion. We chose this method to determine the confocal volumes over xyz scan of fluorescent beads because we perform FCS measurements at 50 μm into the sample and not at the glass surface. We also chose this method over calculating the confocal volume from τ_D because this method is dependent on the model employed to fit the autocorrelation functions. We derived for 488 nm excitation a confocal volume of 0.18 fl, for 633 nm excitation a confocal volume of 0.35 fl, and for the cross-correlation volume 2.16 fl.

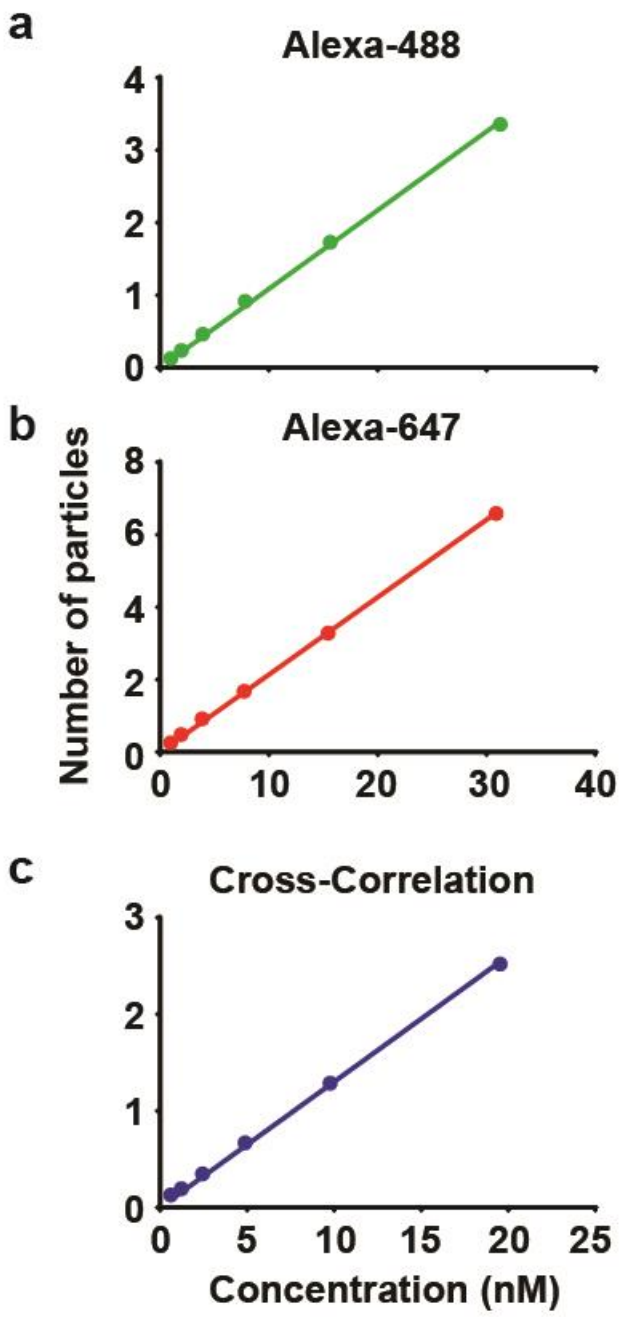

Figure 3.3.3 Linear plots of Alexa-488, Alexa-647, and CC number of particles as a function of concentration. (a) Alexa-488 plot, (b) Alexa-647 plot, and (c) cross-correlation plot.

3.3.4 Cross-Talk Quantification

We determine the cross-talk contribution from the green channel into the red channel using the method by Bacia & Schwille (2007). [52] In this method, the bleed-through ratio is determined from a solution of Alexa-488 excited with 488 nm excitation. The excitation is recorded on either the green (GaAsP 1) or the red channel (GaAsP 2) and the ratio is taken from these count rates. We determined these values using the FCCS acquisition parameters we used for the ligand binding assays. Table 3.3.4 shows the calculated count rates for Alexa-488 detected in both channels using two different main beam splitters.

Table 3.3.4 Cross-talk quantification values determined from a solution of Alexa-488.

Alexa-488 (MBS 488)		Bleed-through Ratio	
Count Rate (GaAsP 1)	Count Rate (GaAsP 2)		
93.292	0.569	0.00609913	
A488 Count Rate (MBS 488/561/633)		**Bleed-through Ratio**	
Count Rate (GaAsP 1)	Count Rate (GaAsP 2)		
80.169	0.574	0.007159875	
Dual-labeled Oligo (MBS 488/561/633)		**Corrected Ratio**	**Gx/Gg**
Count Rate (GaAsP 1)	Count Rate (GaAsP 2)		
1.551	3.383	0.003282579	0.875908

We observe that regardless of the MBS used, we observe no difference in the bleed-through ratio for Alexa-488. We use MBS 488 exclusively for 488 nm excitation and we use MBS 488/561/633 for both 633 nm excitation and CC measurements. To determine if cross-talk made a significant contribution to the CC amplitude, we recorded count-rates for the dual-labeled oligonucleotide at concentrations similarly used for ligand binding measurements. We took the ratio of these count rates and multiplied the ratio by the bleed-through ratio. In comparison to the relative cross-correlation, the cross-talk contribution to the CC is less than 1% indicating that cross-talk makes no contribution to the CC amplitude.

3.3.5 Calculating K_D and K_i values from FCCS measurements

We calculated theoretical curves showing the dependency of $G(0)$, the correlation amplitudes, on the concentrations of labeled and competitor ligands. Curves were calculated under the assumptions that the ligands interacted with a 1 to 1 stoichiometry with the receptor, ligand and receptor are 100% labeled, the confocal volumes for green and red excitation are the same volume, there are no chromatic aberrations, and cross-talk is negligible. For saturation binding, we analyzed the behavior of $G(0)$ for two different dissociation constants of 5 and 0.5 nM (Figure 3.3.5)

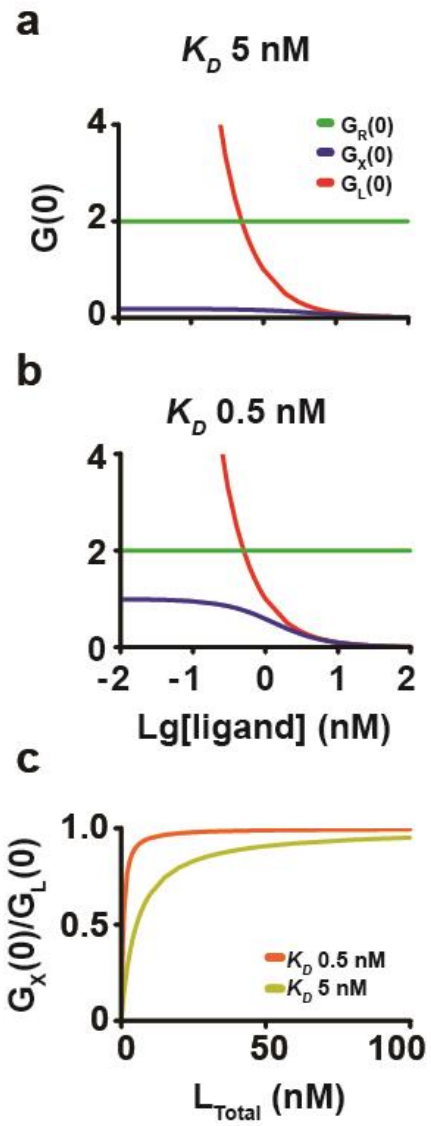

Figure 3.3.5a Dependency of correlation amplitudes on concentrations of receptor (green, $G_R(0)$), ligand (red, $G_L(0)$), and complex (blue, $G_X(0)$) for saturation binding at K_D values of 5 (a) and 0.5 nM (b). (c) Saturation binding isotherms for $K_D = 5$ nM (orange) and $K_D = 0.5$ nM (yellow) derived from the ratio of $G_X(0)/G_L(0)$ as a function of total fluorescent ligand.

Receptor concentration is kept constant in saturation binding so $G_R(0)$, the correlation amplitude from labeled receptors (green line), does not change with varying ligand concentration. In the other hand, $G_L(0)$ the correlation amplitude from ligand (red line), increases as ligand concentration decreases with equal magnitude for both 5 and 0.5 nM binding affinities. $G_X(0)$, the cross-correlation amplitude from the ligand-receptor complex (blue line), shows a sigmoidal behavior for both binding constants analyzed. At low ligand concentrations, $G_X(0)$ reaches a plateau since ligand is the limiting reagent in complex formation. At high ligand concentrations, receptor concentration becomes the limiting reagent and $G_X(0)$ reaches another plateau since no more complex can be formed with more ligand added. At $K_D = 0.5$ nM, $G_X(0)$ has a higher amplitude than $K_D = 5$ nM because there is more ligand-receptor complex at higher ligand affinities. Since the correlation amplitudes are inversely proportional to the concentration of labeled species, the ratio of $G_X(0)$ / $G_L(0)$ gives the fractional occupancy. Figure 3.3.5a (c) shows the saturation binding isotherms for $K_D = 0.5$ nM (orange) and 5 nM (yellow) as a function of total concentration of labeled ligand. The saturation binding isotherms show the expected hyperbolic behavior with the K_D values being at the right place.

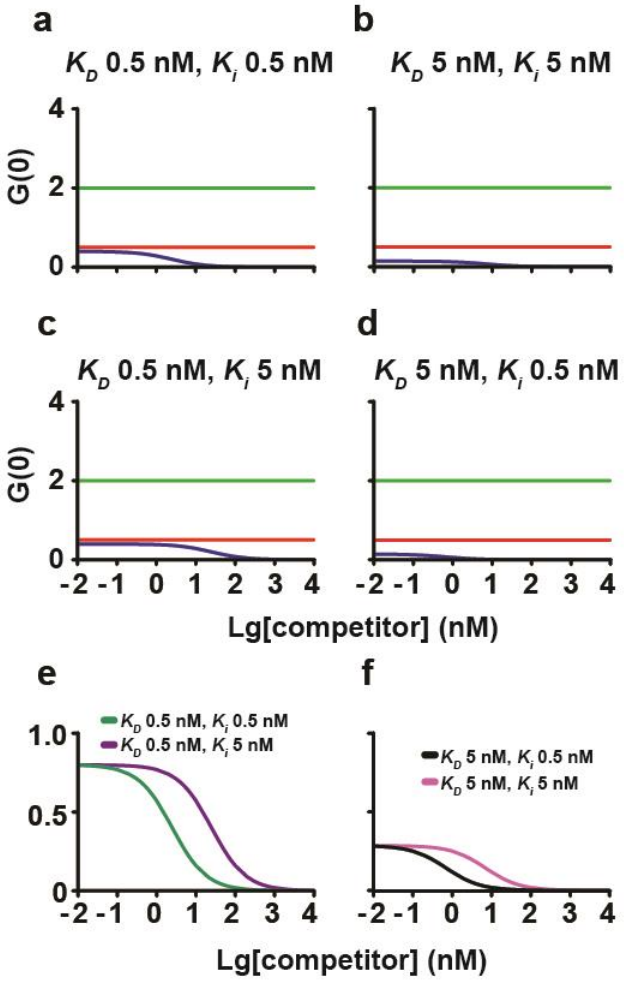

Figure 3.3.5b Dependency of correlation amplitudes on concentrations of receptor, ligand, and complex for competition binding at $K_D = 0.5$ nM; $K_i = 0.5$ nM (a), $K_D = 0.5$ nM; $K_i = 5$ nM (c), $K_D = 5$ nM; $K_i = 5$ nM (b), and $K_D = 5$ nM; $K_i = 0.5$ nM (d). (e) Competition binding isotherms for $K_D = 0.5$ nM; $K_i = 0.5$ nM (purple), $K_D = 0.5$ nM; $K_i = 5$ nM (green), and (f) $K_D = 5$ nM; $K_i = 0.5$ nM (black), and $K_D = 5$ nM; $K_i = 5$ nM (magenta) derived from the ratio of $G_X(0)/G_L(0)$ as a function of total competitor.

For competition binding, we analyzed both $K_D = 0.5$ nM and 5 nM and we assumed that the inhibition constants of the unlabeled ligand were $K_i = 0.5$ nM and 5 nM (Figure 3.3.5b) Like saturation binding, $G_R(0)$ remains constant for all concentrations of competitor tested. $G_L(0)$ also remains constant since a fixed concentration of labeled ligand is used for all tested concentrations of competitor. $G_X(0)$ shows similar sigmoidal behavior as with saturation binding for all competition cases analyzed. The amplitude of $G_X(0)$ is dependent on the concentration of labeled ligand and the dissociation constant such that higher affinities have higher amplitudes. At high competitor concentrations, ligand is displaced from the receptor binding site such that the complex concentration decreases and $G_X(0)$ goes to 0. In that cases that $K_i = 0.5$ nM, the inflection point is shifted towards left since less concentration of competitor is required to displaced the labeled ligand. In the other hand, the inflection point for $G_X(0)$ is shifted to the right for $K_i = 5$ nM since higher concentrations of competitor are required to displaced the labeled ligand. Figure 3.3.5b shows the competition binding isotherms for the cases where $K_D = 0.5$ nM and K_i was set to either 0.5 or 5 nM (e). (f) shows the competition isotherms for $K_D = 5$ nM and K_i was set to either 0.5 or 5 nM. For $K_D = 0.5$ nM, the fractional occupancy is higher than for $K_D = 0.5$ nM since higher complex will be found for the higher affinity ligand at equal competitor concentrations. For $K_i = 5$ nM, the inflection point is shifted to the right since higher concentration of competitor is required to displaced the labeled ligand.

3.3.6 Saturation Ligand Binding with RANTES Analogues

We performed saturation binding experiments with Alexa-647 labeled RANTES analogues and purified CCR5-SNAP-488 by FCCS to determine their equilibrium dissociation constants. Figure 3.3.6a (a) shows representative auto-correlation traces for 5P12- and 6P4-647 in the presence of CCR5-SNAP-488. Correlation traces were fitted to a 1 3D translational diffusion component undergoing independent blinking and triplet state transitions. Triplet and blinking states were normalized to derive the total number of fluorescent particles. Figure 3.3.6a (b) shows the auto-correlation traces for CCR5-SNAP-488 for different concentrations of 5P12- and 6P4-647 tested and their associated fits. CCR5-SNAP-488 auto-correlation traces were fitted to 1 component with 3D translational diffusion undergoing triplet state transitions with $\tau_{Triplet}$ fixed to 4 µs. Figure 3.3.6a (b) shows the cross-correlation traces obtained for the 5P12- and 6P4-647/CCR5-SNAP-488 complexes at the different ligand concentrations tested. Cross-correlation traces were fitted to 1 translational component with no triplet or blinking transitions since Alexa-488 and Alexa-647 photophysical processes are independent of each other.

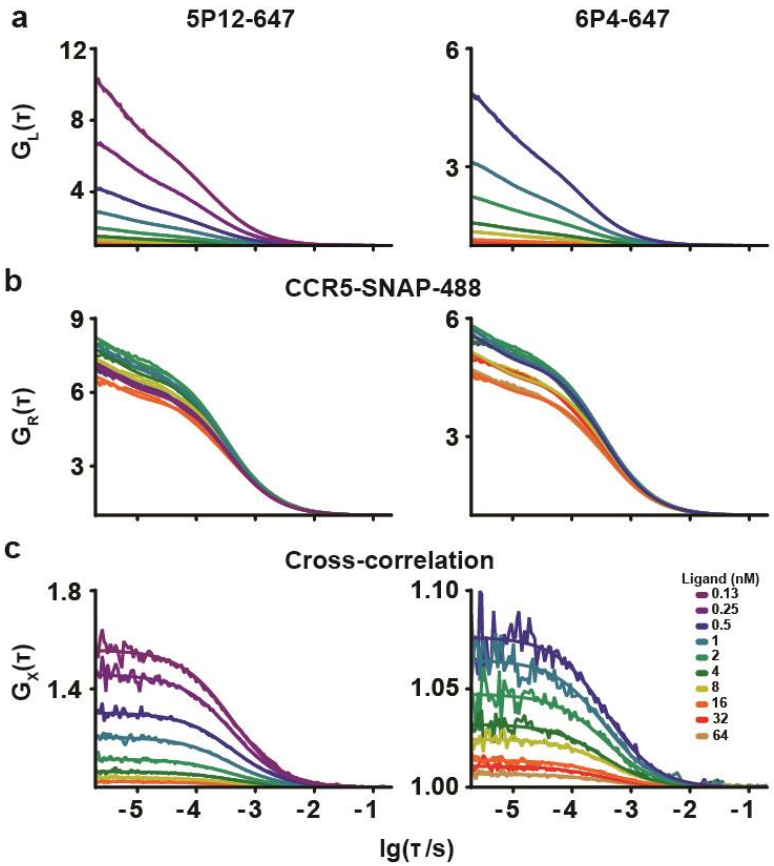

Figure. 3.3.6a (a) 5P12-647 (left) and 6P4-647 (right) auto-correlation traces and fits for all concentrations tested. (b) CCR5-SNAP-488 auto-correlation traces and fits for different concentrations of 5P12-647 (left) and 6P4-647 (right). (c) Receptor-ligand complex cross-correlation traces and fits for different concentrations of 5P12-647 (left) and 6P4-647 (right).

Figure 3.3.6b shows the saturation binding isotherms derived for 5P12- and 6P4-647 by plotting RL/R as a function of labeled chemokine.

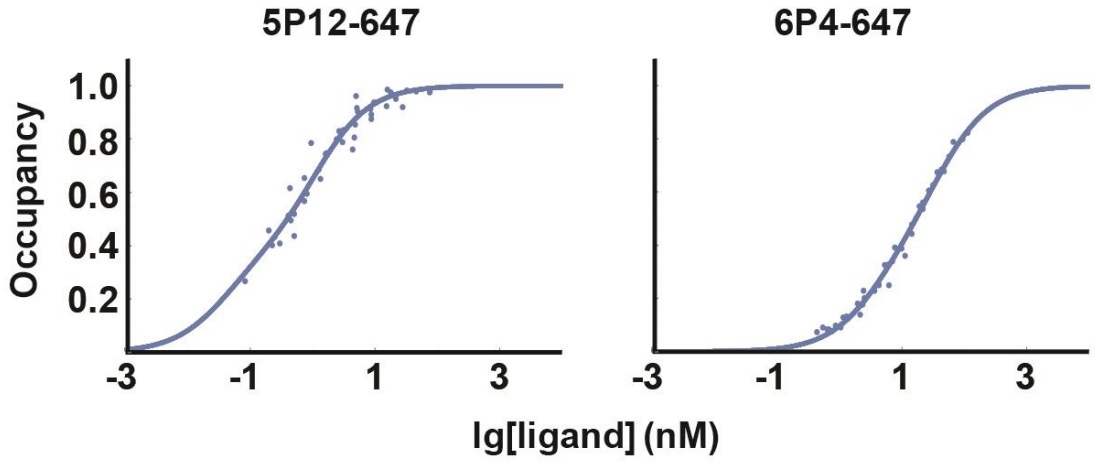

Figure 3.3.6b. Normalized saturation binding isotherms for 5P12- and 6P4-647 binding to CCR5-SNAP-488 in solution. Data points represent individual points for different concentrations of labeled chemokine. The blue solid line represents the global fit performed on the data points.

Qualitatively, 5P12 shows higher affinity than 6P4-647, which is different from the affinities calculated by Gaertner (2008). We repeated the same FCCS measurements on 5P14- and PSC-647 to determine their K_D values. Figure 3.3.6c shows auto-correlation traces for 5P12- and 6P4-647 (a) for CCR5-SNAP-488 (b) and the cross-correlation traces obtained for the ligand-receptor complex (c) at the different ligand concentrations tested. Auto- and cross-correlation traces were fitted the same way as done for 5P12- and 6P4-647 saturation binding measurements.

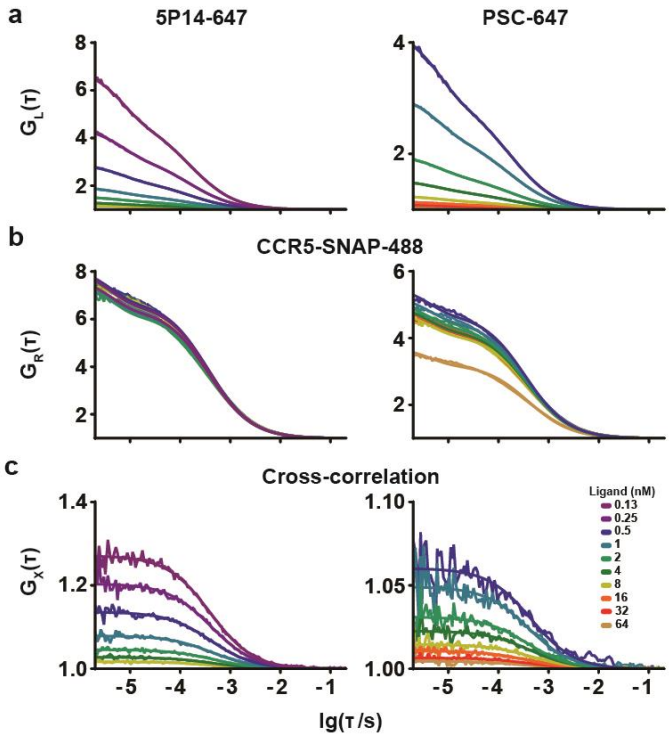

Figure 3.3.6c (a) 5P14-647 and PSC-647 auto-correlation traces and fits for all concentrations tested. (b) CCR5-SNAP-488 auto-correlation traces and fits for different concentrations of 5P14-647 and PSC-647. (c) Receptor-ligand complex cross-correlation traces and fits for different concentrations of 5P14-647 and PSC-647.

Likewise, we derived concentrations for each fluorescent component and derived binding isotherm for 5P14- and PSC-647. Figure 3.3.6d shows the saturation binding isotherms derived for 5P14- and PSC-647 by plotting RL/R as a function of labeled chemokine.

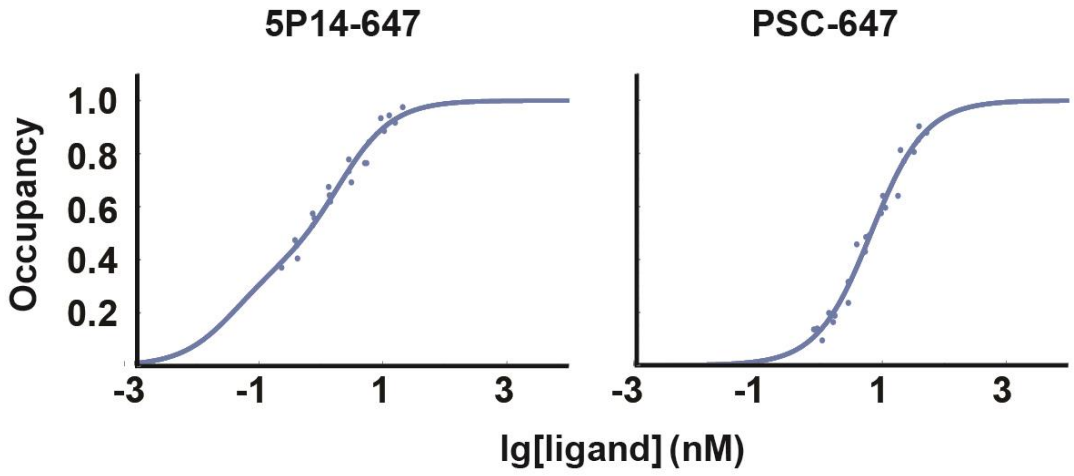

Figure 3.3.6d. Normalized saturation binding isotherms for 5P14- and PSC-647 binding to CCR5-SNAP-488 in solution. Data points represent individual points for different concentrations of labeled chemokine. The blue solid line represents the global fit performed on the data points.

To derive K_D values, we performed global fitting on the saturation binding isotherms employing two binding sites with ligand depletion (Table 3.3.6) We assumed that the binding sites were non-interchangeable since computations where the sites could interchange yielded one observable affinity. We also fixed the active CCR5-SNAP-488 fraction to 25% of the total receptor concentration and within this fraction we fixed the high affinity fraction, $f_{A,H}$, to 38% and low affinity fraction, $f_{A,L}$, to 62%. To derive errors for each value, we performed bootstrapping. The data are resampled with replacement. Global analysis with non-linear least squares fitting of the binding isotherms gives fitting parameters that describe the complete data set. The bootstrap resampling is repeated 100 times and analysis of the means and standard deviations of the fitting parameters describes their distribution. I eliminate few cases (14 out of 100) where the fitting

resulted in fits with high and low affinities switched after the fit for any of the 4 competition experiments (5P12, 5P14, 6P4, or PSC).

Table 3.3.6. Equilibrium dissociation constants for the CCR5-SNAP-488 high affinity state ($K_{D,H}$) and low affinity state ($K_{D,L}$) derived from saturation binding with the RANTES analogues labeled with Alexa-647. Units are in nanomolar and errors were derived using global analysis with non-linear least square fitting of the binding isotherms with bootstrapping.

Chemokine	$K_{D,H}$ (nM)	$K_{D,L}$ (nM)
5P12-647	0.05 ± 0.05	1.3 ± 0.5
5P14-647	0.04 ± 0.03	2.2 ± 0.9
6P4-647	3.8 ± 0.5	43 ± 11
PSC-647	4.8 ± 1.5	16 ± 29

We calculated similar dissociation and bound fraction values for 5P14- and PSC-647 as 5P12- and 6P4-647 respectively indicating that 5P12/5P14 and PSC/6P4 bind similarly to the two CCR5-SNAP-488 species. We did not observe any changes in the molecular brightness for the RANTES analogues and CCR5-SNAP across the concentrations tested (Figure 3.3.6e). We also did not observe any effect Alexa-647 and Alexa-488 triplet state transitions (Figure 3.3.6f) and Alexa-647 blinking transitions (Figure 3.3.6g). Likewise, we did not observe any effect from increasing ligand concentration on the diffusion time of the three fluorescent species (Figure 3.3.6h).

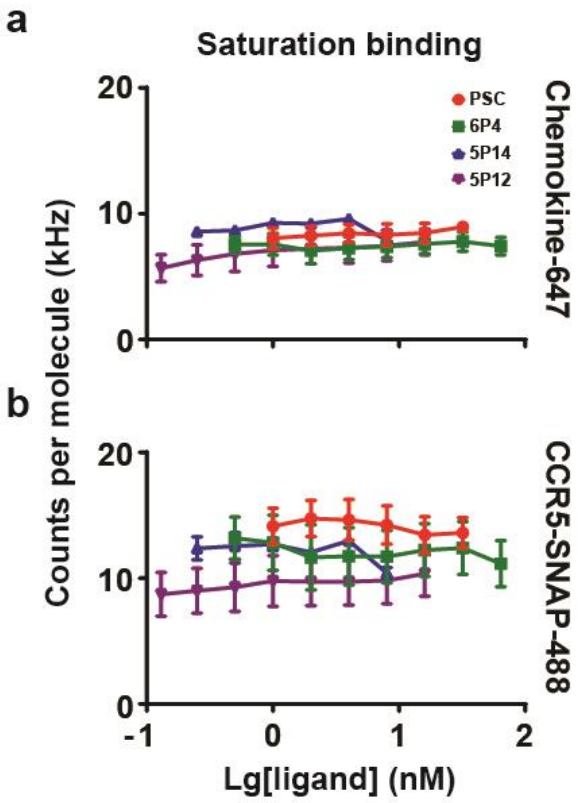

Figure 3.3.6e Brightness Dependency on Ligand Concentration. Average brightness values measured as counts per molecule (kHz) for the RANTES analogues labeled with Alexa-647 (a) and CCR5-SNAP-488 (b) as a function of labeled chemokine. Values are averages from at least 3 independent experiments and errors are the S.E.M.

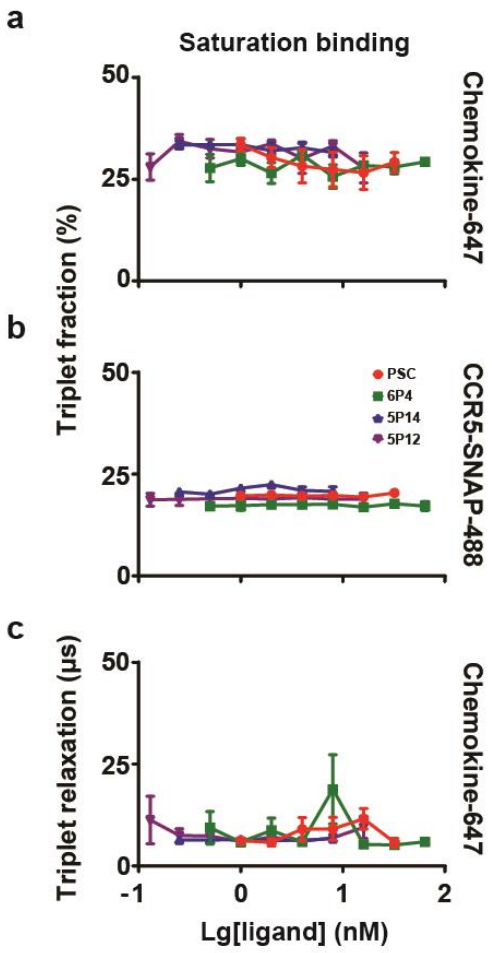

Figure 3.3.6f Average triplet state fraction determined from fitting auto-correlation curves for the RANTES analogues labeled with Alexa-647 (a) and CCR5-SNAP-488 (b) as a function of labeled chemokine. Triplet state fraction are fitted such that they are a percent of total fluorescent and non-fluorescent species in solution. Average triplet state relaxation time in µs determined from fitting auto-correlation curves for the RANTES analogues labeled with Alexa-647 (c) as a function of labeled chemokine concentration. CCR5-SNAP triplet relaxation time was fixed to 4 µs in all experiments and was not plotted. Values are averages from at least 3 independent experiments and errors are the S.E.M.

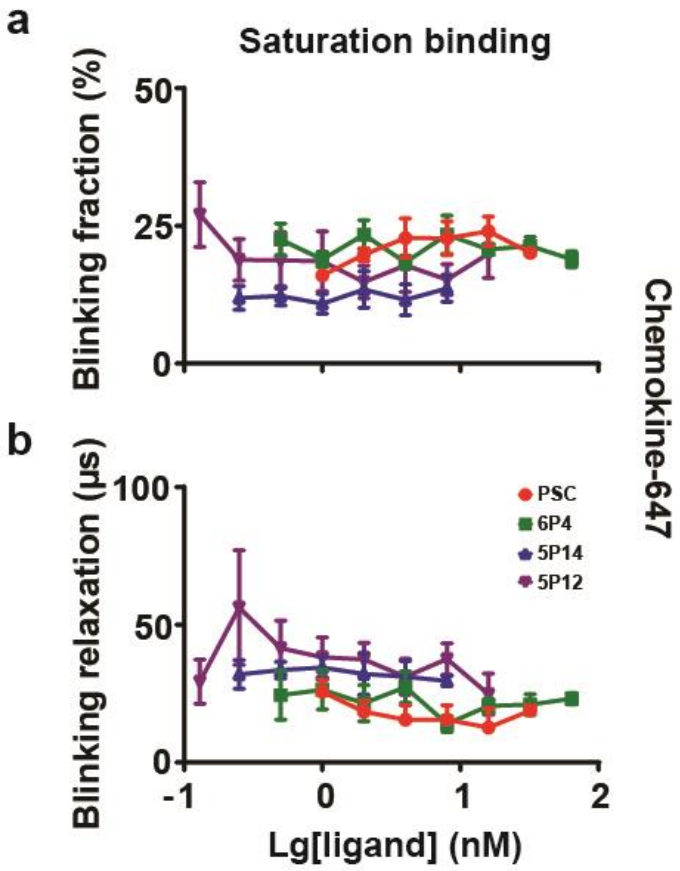

Figure 3.3.6g Average blinking state fraction (a) and blinking state relaxation time (b) determined from fitting auto-correlation curves for the RANTES analogues labeled with Alexa-647 from saturation binding experiments as a function of labeled chemokine concentration. Blinking state fractions are fitted such that they are a percent of total fluorescent and non-fluorescent species in solution. Values are averages from at least 3 independent experiments and errors are the S.E.M.

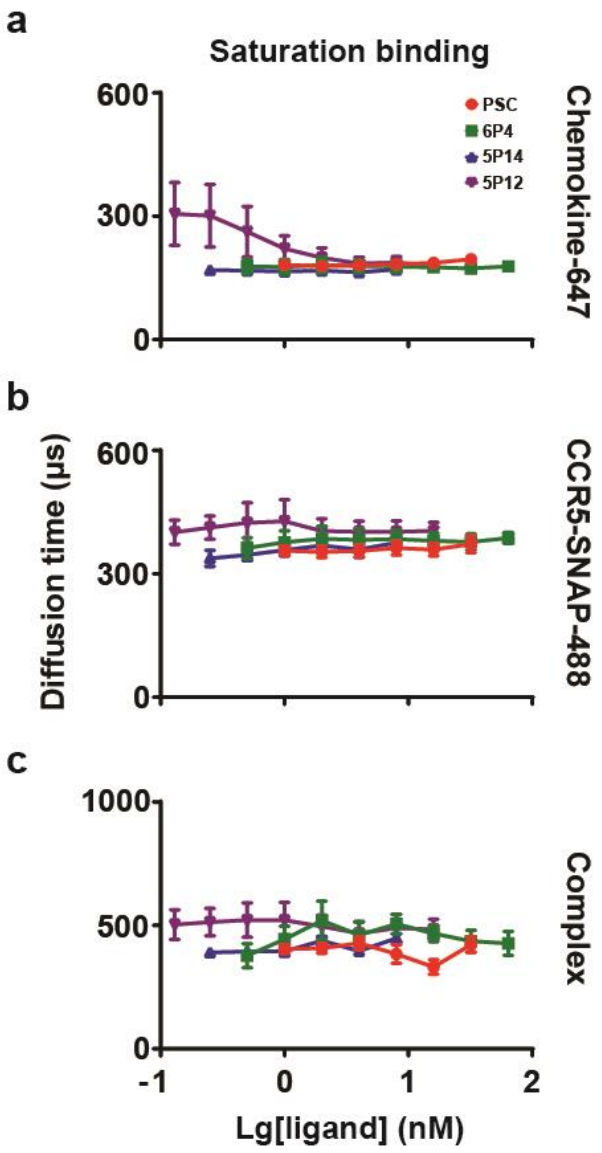

Figure 3.3.6h Average diffusion times (τ_D) in µs determined from fitting auto- and cross-correlation curves for the RANTES analogues labeled with Alexa-647 (a), CCR5-SNAP-488 (b), and the receptor-ligand complex (c) as a function of labeled chemokine concentration. Values are averages from at least 3 independent experiments and errors are the S.E.M.

3.3.7 Competition Binding with 5P12- and 6P4-647

We performed homologous competition binding experiments with 5P12- and 6P4-647 using non-labeled 5P12 and 6P4 to determine the affinity of the non-labeled chemokines. We only employed 5P12- and 6P4-647 for the competition binding experiments since 5P14- and PSC-647 are like 5P12- and 6P4-647 in their binding affinities respectively. Auto- and cross-correlation traces were fit as described previously for the saturation binding experiments. Figure 3.3.7a shows representative auto-correlation traces and associated fits for 5P12- and 6P4-647 (a), auto-correlation traces and fits for CCR5-SNAP-488 (b), and cross-correlation traces and fits for the 5P12- and 6P4-647 bound to CCR5-SNAP-488 in the presence of various concentrations of competing 5P12 and 6P4.

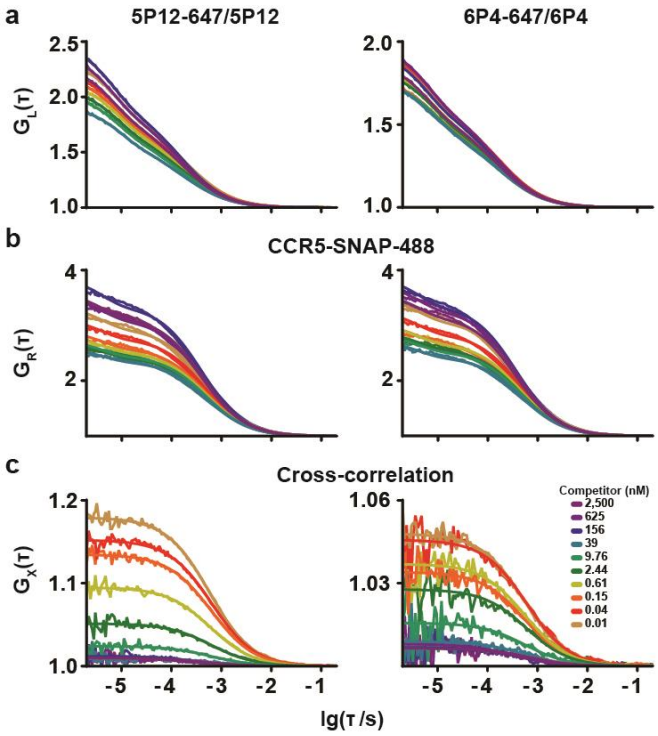

Figure 3.3.7a (a) 5P12-647 (left) and 6P4-647 (right) auto-correlation traces and fits for all concentrations of competitor tested. (b) CCR5-SNAP-488 auto-correlation traces and fits in the presence of 5P12-647 (left) and 6P4-647 (right) at different concentrations of competitor. (c) Receptor-ligand complex cross-correlation traces and fits for 5P12-647 (left) and 6P4-647 (right) at different concentrations of competitor.

We derived binding isotherms for the competition data using the same principles as the saturation binding fits. We performed a global fit with the Cheng-Prusoff equation using the calculated K_D values from the saturation binding experiments. To account for ligand depletion, we fitted the equation iteratively until the fit converged. Fits were plotted in a 3D surface with fluorescent ligand concentration as the 3rd axis. Figure 3.3.7b shows the 3D surface plots for homologous competition binding of 5P12 and 6P4.

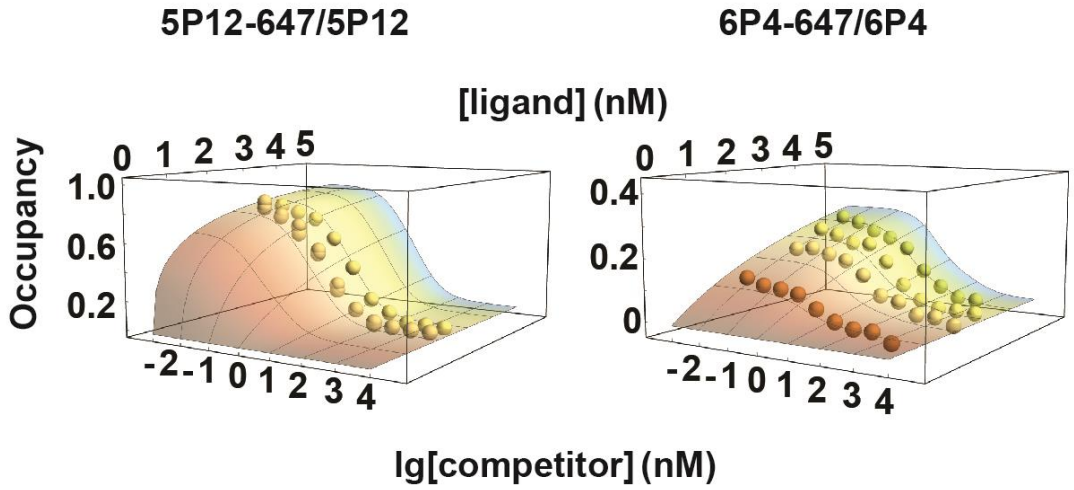

Figure 3.3.7b 3D surface plots for homologous competition binding of 5P12- and 6P4-647. 5P12-647 homologous curves are shown on the right while 6P4 homologous competition curves are shown on the right. 3D surfaces were generated by plotting the normalized global fits and individual data points as a function of labeled chemokine concentration.

We also performed heterologous competition binding experiments using 5P12- and 6P4-647 with 6P4 and 5P12 respectively to validate the two-binding site model. Figure 3.3.7c shows the autocorrelation traces and associated fits for 5P12- and 6P4-647 (a), auto-correlation traces and CCR5-SNAP-488 (b) and cross-correlation traces and for the 5P12- and 6P4-647 bound to CCR5-SNAP-488 in the presence of various concentrations of competing 6P4 and 5P12 respectively.

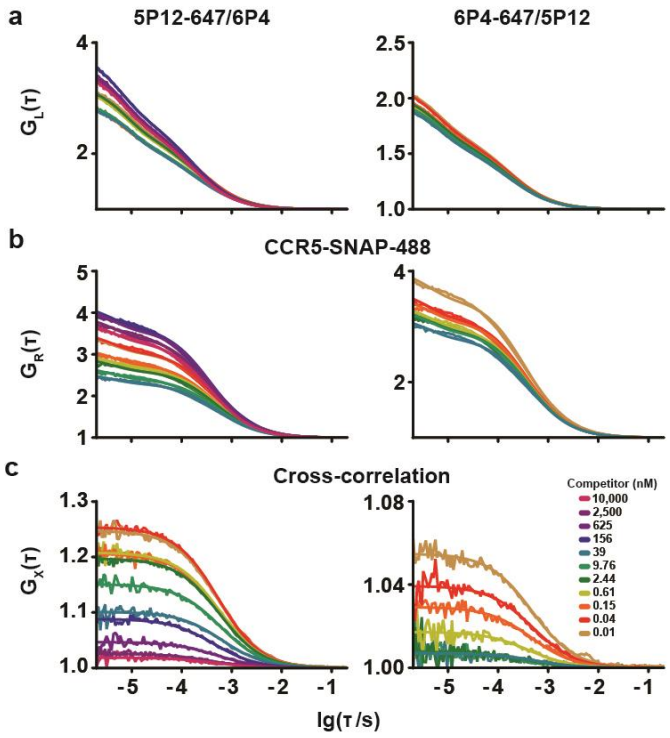

Figure 3.3.7c (a) 5P12-647 and 6P4-647 auto-correlation traces and fits for all concentrations of competitor tested. (b) CCR5-SNAP-488 auto-correlation traces and fits in the presence of 5P12-647 and 6P4-647 at different concentrations of competitor. (c) Receptor-ligand complex cross-correlation traces and fits for 5P12-647 and 6P4-647 at different concentrations of competitor.

We also derived 3D surface plots for heterologous competition binding of 5P12 and 6P4. Figure 3.3.7d shows the 3D surface plots for 5P12- and 6P4- heterologous competition. Surface plots were generated using the same method as for the homologous competition surface plots.

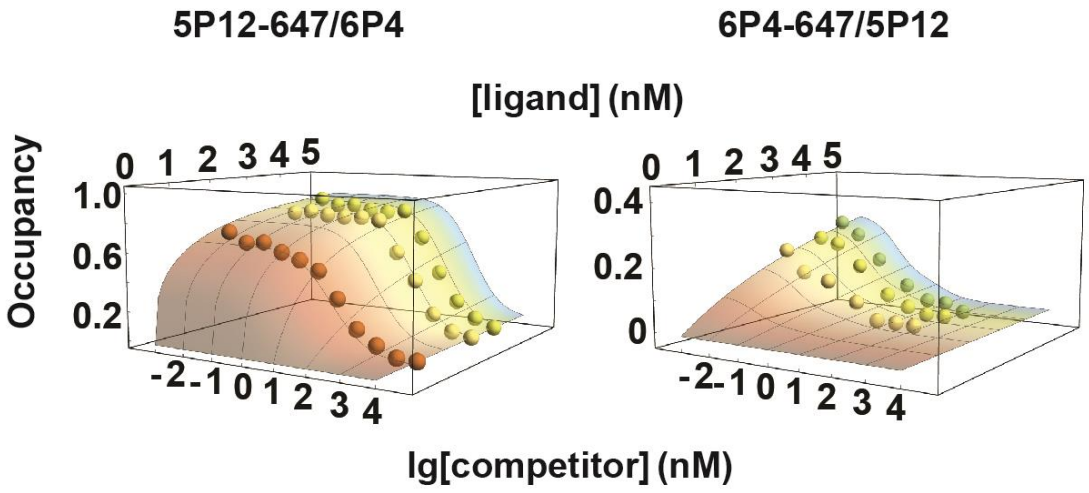

Figure 3.3.7d 3D surface plots for heterologous competition binding of 5P12- and 6P4-647. 5P12-647 heterologous curves are shown on the right while 6P4 heterologous competition curves are shown on the right. 3D surfaces were generated by plotting the normalized global fits and individual data points as a function of labeled chemokine concentration.

Table 3.3.7 Equilibrium constants of inhibition for the CCR5-SNAP-488 high affinity state ($K_{i,H}$) and low affinity state ($K_{i,L}$) derived from competition binding with the RANTES analogues labeled with Alexa-647 and unlabeled analogues. Units are in nanomolar and errors were derived using global analysis with non-linear least square fitting of the binding isotherms with bootstrapping.

Labeled/Unlabeled	$K_{i,H}$ (nM)	$K_{i,L}$ (nM)
5P12-647/5P12	0.007 ± 0.005	0.8 ± 0.4
5P12-647/6P4	0.9 ± 0.7	56 ± 22
6P4-647/6P4	1.3 ± 0.3	N.D.
6P4-647/5P12	0.02 ± 0.01	N.D.

We did not observe any changes in the molecular brightness for the RANTES analogues and CCR5-SNAP across the concentrations tested (Figure 3.3.7e). We also did not observe any effect Alexa-647 and Alexa-488 triplet state transitions (Figure 3.3.7f) and Alexa-647 blinking transitions (Figure 3.3.7g). Likewise, we did not observe any effect from increasing ligand concentration on the diffusion time of the three fluorescent species (Figure 3.3.7h). For some of the values, we observe a sharp increase or decrease in the plots, which is caused by replenishing the immersion water to avoid evaporation during data collection.

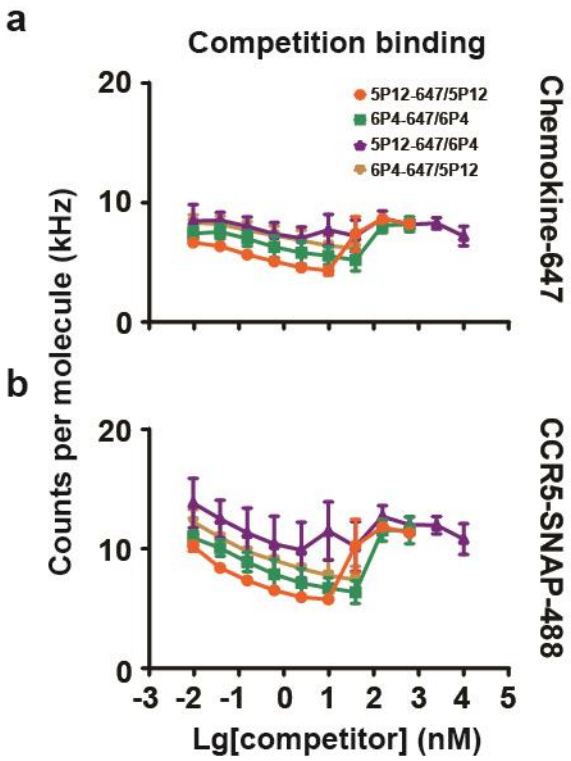

Figure 3.3.7e Brightness Dependency on Competitor Concentration.

Average brightness values measured as counts per molecule (kHz) for the RANTES analogues labeled with Alexa-647 (a) and CCR5-SNAP-488 (b) as a function of competitor. Values are averages from at least 3 independent experiments and errors are the S.E.M.

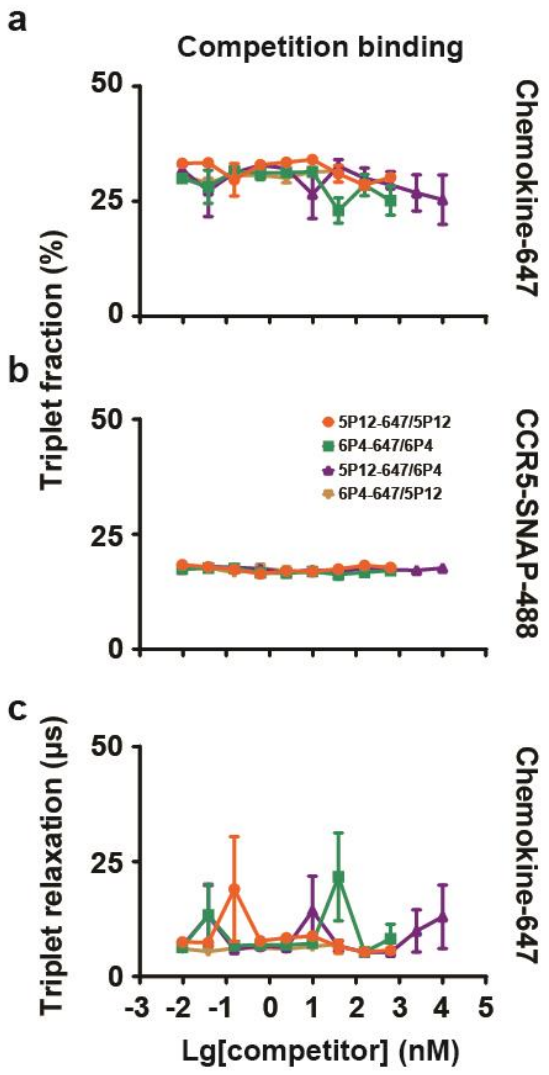

Figure 3.3.7f Average triplet state fraction determined from fitting auto-correlation curves for the RANTES analogues labeled with Alexa-647 (a) and CCR5-SNAP-488 (b) as a function of competitor. Triplet state fractions are fitted such that they are a percent of total fluorescent and non-fluorescent species in solution. Average triplet state relaxation time in µs determined from fitting auto-correlation curves for the RANTES analogues labeled with Alexa-647 (c) as a function of competitor concentration. CCR5-SNAP triplet relaxation time was fixed to 4 µs in all experiments and was not plotted. Values are averages from at least 3 independent experiments and errors are the S.E.M.

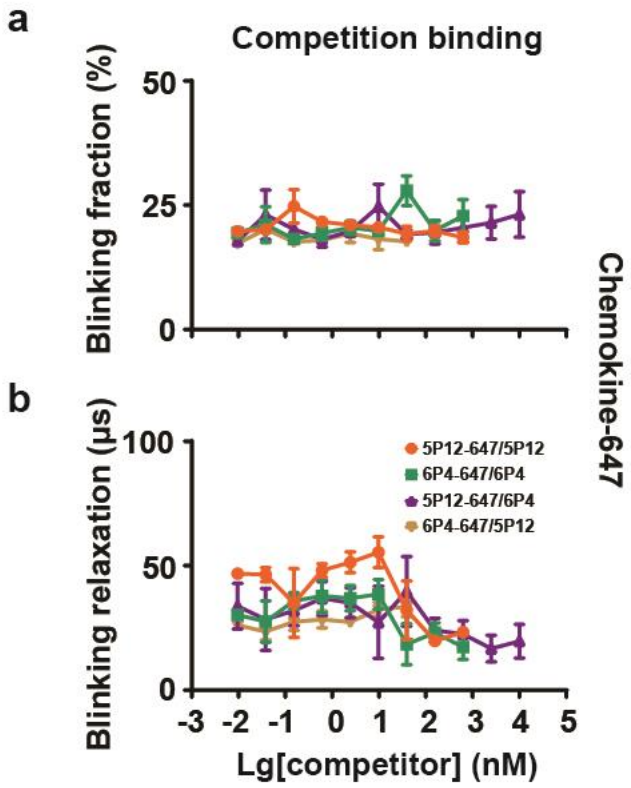

Figure 3.3.7g Average blinking state fraction (a) and blinking state relaxation time (b) determined from fitting auto-correlation curves for the RANTES analogues labeled with Alexa-647 from saturation binding experiments as a function of competitor concentration. Blinking state fractions are fitted such that they are a percent of total fluorescent and non-fluorescent species in solution. Values are averages from at least 3 independent experiments and errors are the S.E.M.

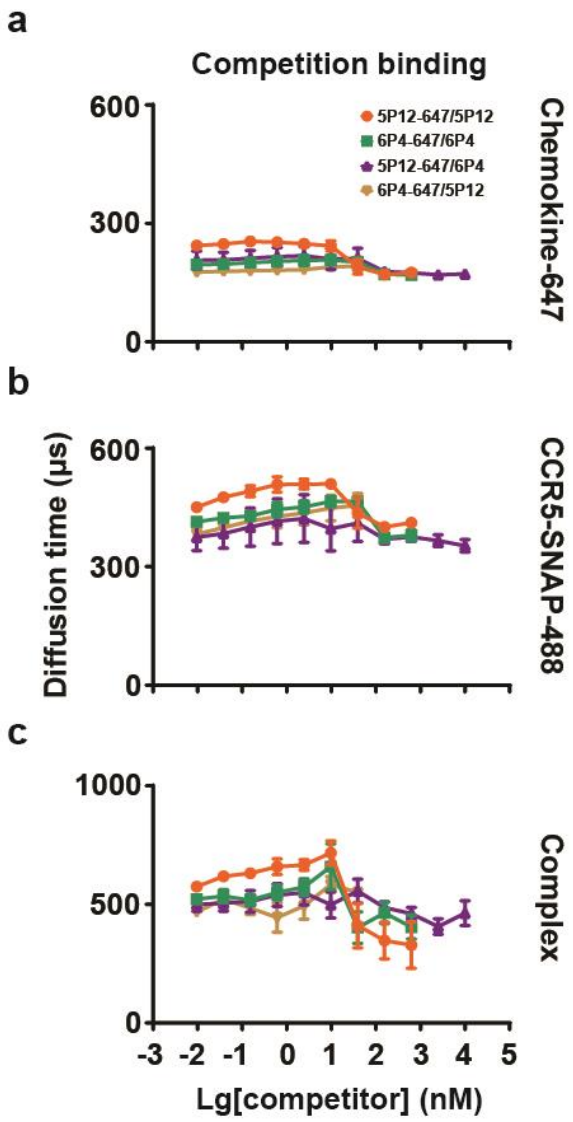

Figure 3.3.7h Average diffusion times (τ_D) in µs determined from fitting auto- and cross-correlation curves for the RANTES analogues labeled with Alexa-647 (a), CCR5-SNAP-488 (b), and the receptor-ligand complex (c) as a function of competitor concentration. Values are averages from at least 3 independent experiments and errors are the S.E.M.

3.3.8 Competition Binding with Native Chemokines and Env

We proceeded to calculate the affinity of gp120 with CCR5-SNAP-488. We performed competition binding experiments with the human soluble CD4 (sCD4) and 2G12 purified monomeric gp120 complex in the presence of 5P12- and 6P4-647. Figure 3.3.8a shows the auto-correlation traces for 5P12- and 6P4-647 (a), CCR5-SNAP-488 (b), and cross-correlation traces for receptor-ligand complex (c) at different concentrations of competing sCD4-gp120.

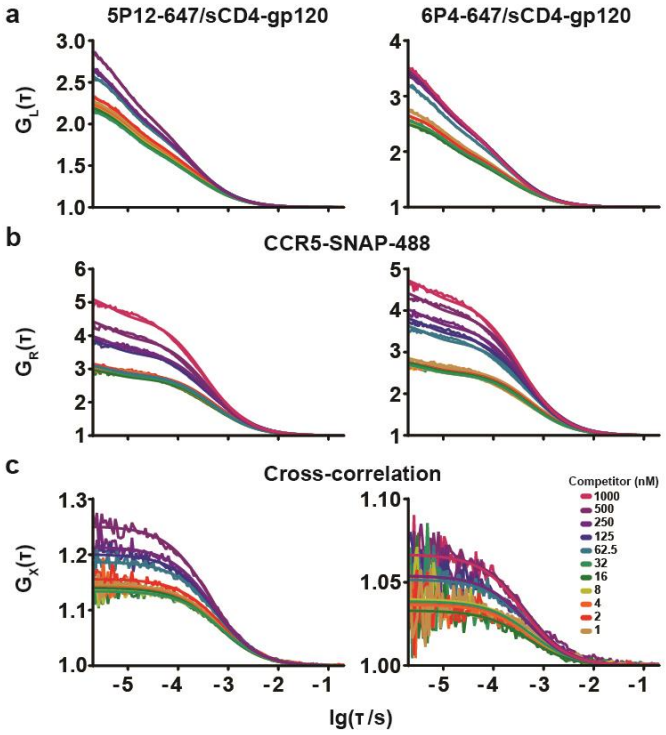

Figure 3.3.8a (a) 5P12-647 and 6P4-647 auto-correlation traces and fits (b) CCR5-SNAP-488 auto-correlation traces and fits (c) Receptor-ligand complex cross-correlation traces and fits for 5P12-647 and 6P4-647 at different concentrations of sCD4-gp120 complex.

Auto- and cross-correlation traces were fitted using the same models and assumptions as done previously. We calculated RL/R and L to determine how the fractional occupancy for 5P12- and 6P4-647 change with increasing concentrations of viral complex. Figure 3.3.8b shows the plots of RL/R as a function L for 5P12- and 6P4-647 in the presence of increasing sCD4-gp120 concentration. sCD4-gp120 concentrations up to 1,000 nM had no effect on 5P12- or 6P4-647 binding to CCR5-SNAP-488 indicating that the complex has low affinity to CCR5-SNAP-488.

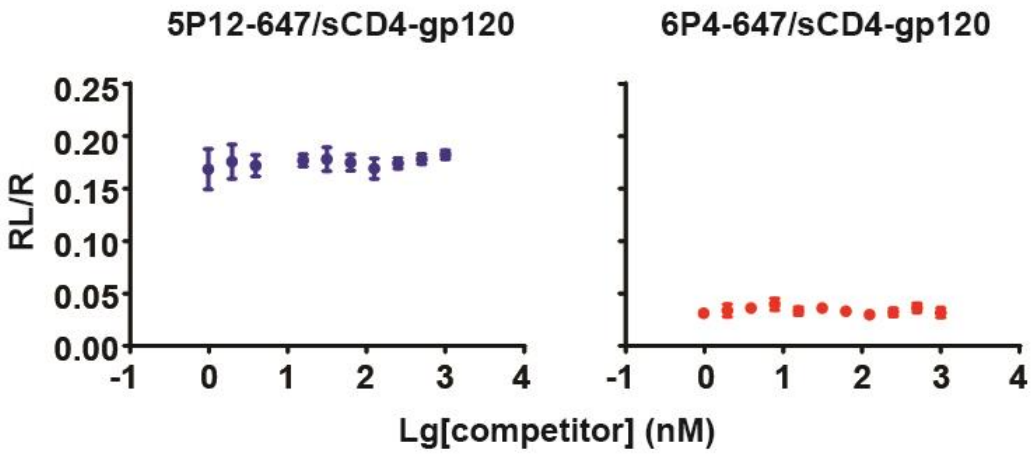

Figure 3.3.8b Competition binding isotherms for 5P12-647 and 6P4-647 at various concentrations of sCD4-gp120 complex. Data points represent the mean from at least 30 individual FCCS measurements and their associated errors.

We then performed competition binding experiments with the native chemokines, RANTES and MIP-1α, to determine their K_i values. Competition binding experiments were performed using the same conditions as with the RANTES analogues competition binding experiments. Figure 3.3.8c shows the auto-correlation traces for 5P12- and 6P4-

647 (a), CCR5-SNAP-488 (b), and cross-correlation traces for receptor-ligand complex (c) at different concentrations of competing RANTES.

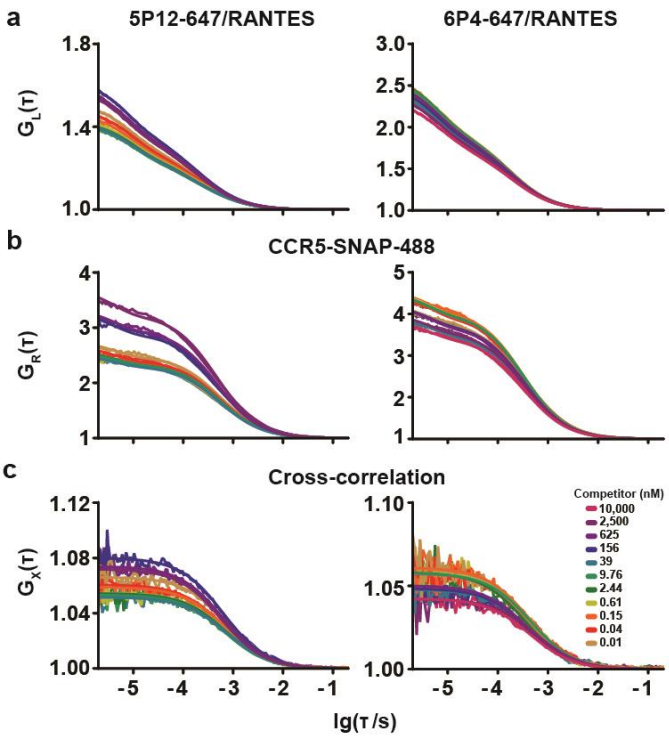

Figure 3.3.8c (a) 5P12-647 and 6P4-647 auto-correlation traces and fits (b) CCR5-SNAP-488 auto-correlation traces and fits (c) Receptor-ligand complex cross-correlation traces and fits for 5P12-647 and 6P4-647 at different concentrations of RANTES.

We observed that $G_X(0)$ varies slightly in comparison to the curves obtained for competition binding with the RANTES analogues. We plotted RL/R and L from the correlation traces to determine the effect increasing concentrations of RANTES had on 5P12- and 6P4- 647 binding to CCR5-SNAP-488. Figure 3.3.8d shows the plots of RL/R as a function L for 5P12- and 6P4-647 in the presence of increasing RANTES concentrations.

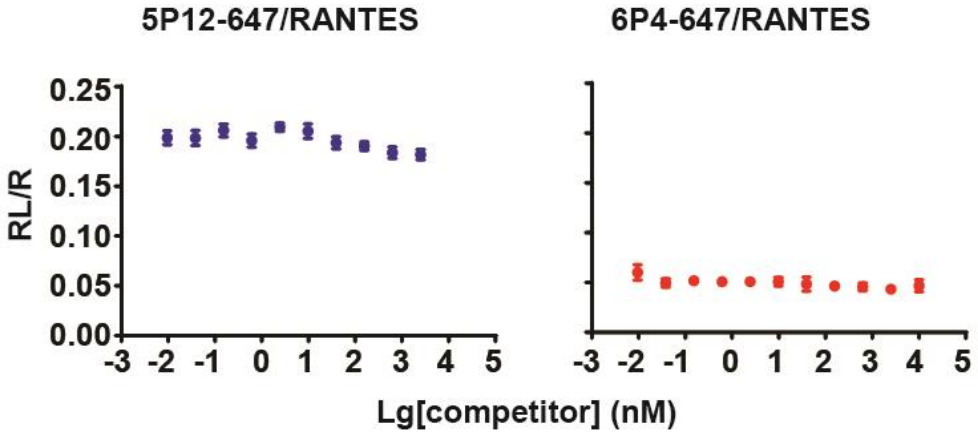

Figure 3.3.8d Competition binding isotherms for 5P12-647 and 6P4-647 at various concentrations of RANTES. Data points represent the mean from at least 30 individual FCCS measurements and their associated errors.

Surprisingly, RANTES did not displace 5P12- or 6P4-647 from CCR5-SNAP-488. Given this remarkable result, we proceeded to test if MIP-1α could compete with 5P12- and 6P4-647. Figure 3.3.8e shows the auto-correlation traces for 5P12- and 6P4-647 (a), CCR5-SNAP-488 (b), and cross-correlation traces for receptor-ligand complex (c) at different concentrations of competing MIP-1α.

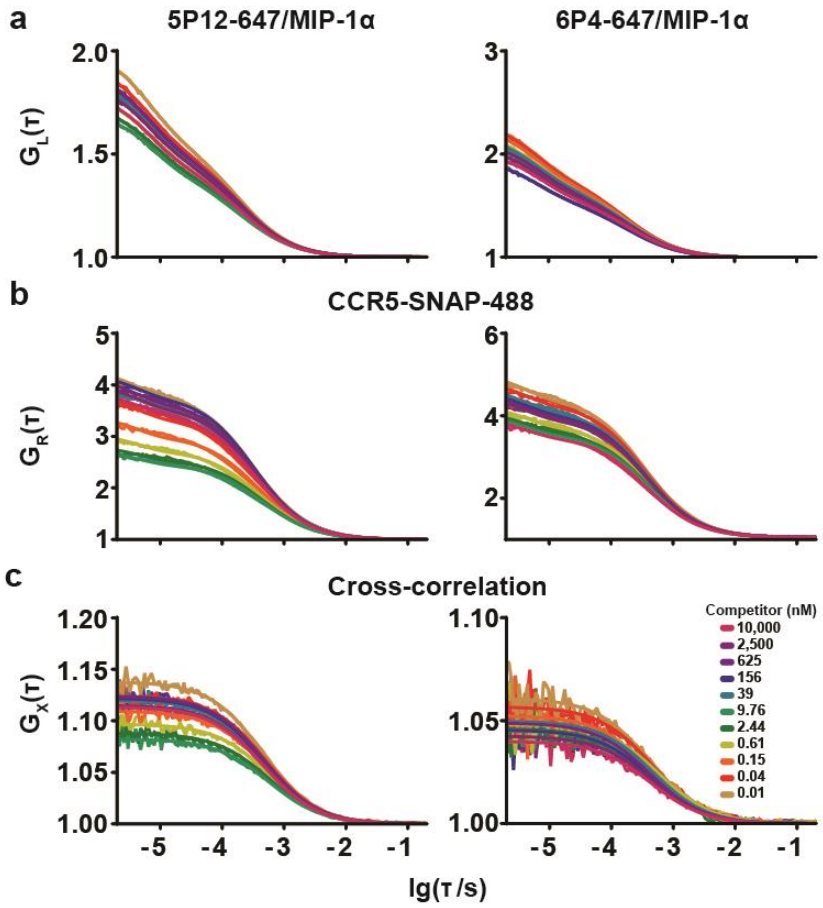

Figure 3.3.8e (**a**) 5P12-647 and 6P4-647 auto-correlation traces and fits (**b**) CCR5-SNAP-488 auto-correlation traces and fits (**c**) Receptor-ligand complex cross-correlation traces and fits for 5P12-647 and 6P4-647 at different concentrations of MIP-1α.

Figure 3.3.8f shows the shows the plots of RL/R as a function L for 5P12- and 6P4-647 in the presence of increasing MIP-1α concentrations. MIP-1α did not displace 5P12- or 6P4-647 from CCR5-SNAP-488. We were surprised by these findings since we expected the native chemokines to completely displace the analogues up to 10 μM concentrations. Given this, we hypothesize that the native chemokines either have very low affinity for CCR5-SNAP-488 or that the chemokines recognize a different receptor state. We have

also observed very little binding of RANTES-647 to CCR5-SNAP-488 in saturation binding experiments and by single molecule TIRF-FRET (data not shown).

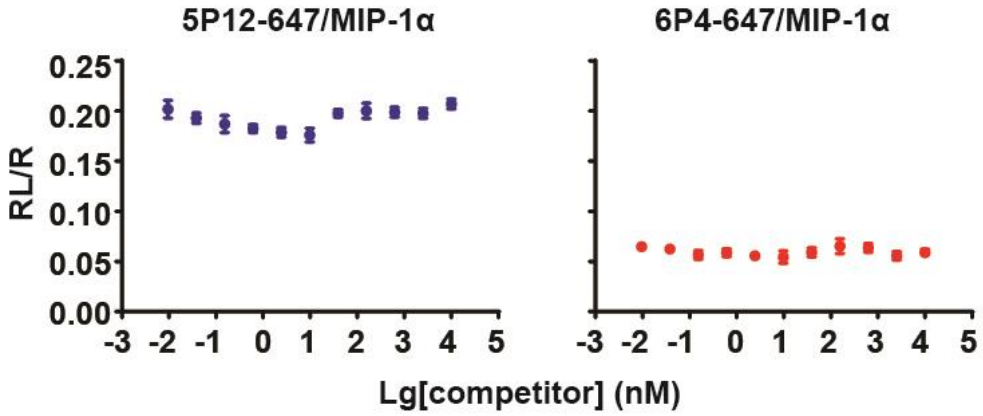

Figure 3.3.8f Competition binding isotherms for 5P12-647 and 6P4-647 at various concentrations of MIP-1α. Data points represent the mean from at least 30 individual FCCS measurements and their associated errors.

3.3.9 Line Scan Analysis of CCR5-SNAP

We performed line-scan analysis FLAG purified CCR5-SNAP-488 resolved by SDS-PAGE and NIR western immunoblotting. We analyzed the lanes using Gel Analyzer in ImageJ. Figure 3.3.9a shows the NIR western immunoblotting results for CCR5-SNAP and the corresponding line scan plots for 680 and 800 nm fluorescence.

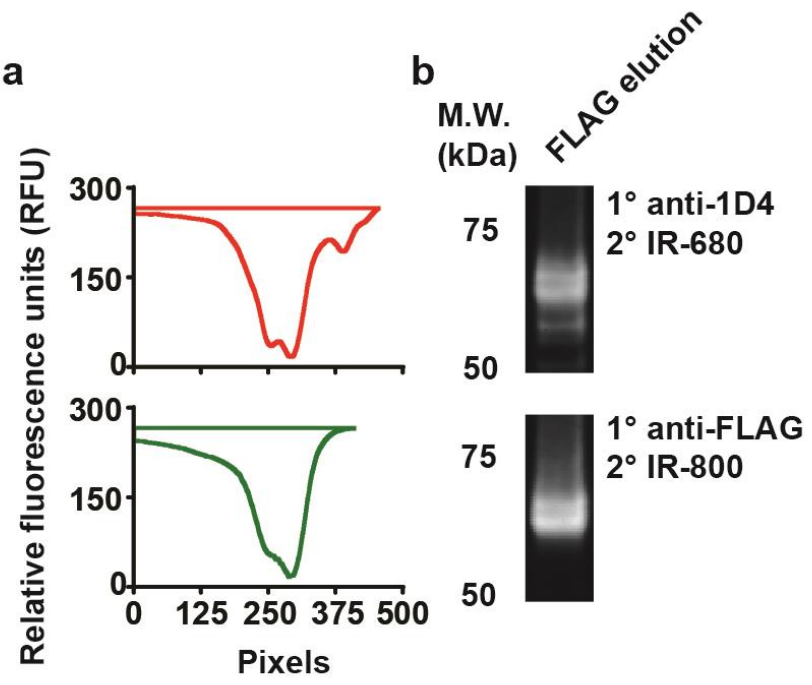

Figure 3.3.9a (a) Line scan analysis performed in ImageJ of the corresponding fluorescent gel lanes in (b). (b) Reducing SDS-polyacrylamide gel electrophoresis and near-infrared fluorescent western blot of FLAG elution from tandem affinity purification of CCR5-SNAP. Full-length CCR5-SNAP was detected using antibodies against the 1D4 and FLAG epitopes and 680 nm (top) and 800 nm (bottom) fluorescent secondary antibodies.

Line scan analysis of FLAG purified CCR5-SNAP-488 fraction reveals two species that are very close in molecular weight. The two overlapping bands are observed in both the 680 and 800 nm emission channels. SNAP-CCR5 also shows similar split band by line-scan analysis (data not shown). We hypothesized that differential O-linked glycosylation yields the split band pattern observed in both CCR5-SNAP and SNAP-CCR5. To test this hypothesis, CCR5-SNAP and SNAP-CCR5 were treated with or without α2-3,6,8,9 Neuraminidase A for 1 hour and then analyzed as described previously. Figure 3.3.9b shows the NIR western immunoblotting results for SNAP-CCR5 treated with and without α2-3,6,8,9 neuraminidase A and the corresponding line scan plots for 680 and 800 nm fluorescence.

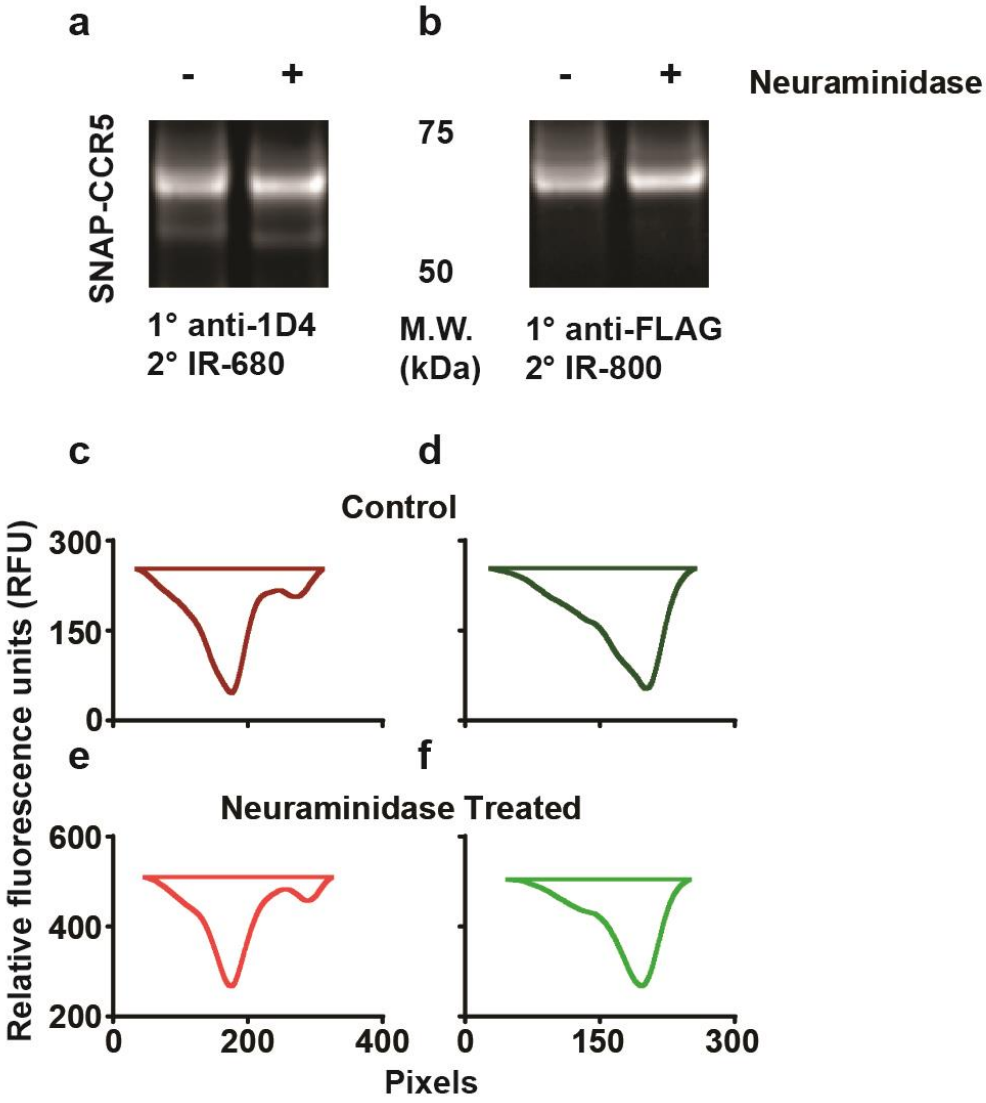

Figure 3.3.9b Reducing SDS-polyacrylamide gel electrophoresis and near-infrared fluorescent western blot of FLAG elution from tandem affinity purification of SNAP-CCR5. SNAP-CCR5 was treated with α2-3,6,8,9 neuraminidase A for 1 hour. Full-length CCR5-SNAP was detected using antibodies against the 1D4 and FLAG epitopes and 680 nm (a) and 800 nm (b) fluorescent secondary antibodies. Line scan analysis performed in ImageJ of the control lanes for 680 nm (c) and 800 nm (d) emission. Line scan analysis performed in ImageJ of the neuraminidase treated samples for 680 nm (e) and 800 nm (f) emission.

SNAP-CCR5 Neuraminidase treatment reduced the observed receptor heterogeneity but did not yield a single band. The result indicates that SNAP-CCR5 is sialylated to some degree. Given this, we cannot exclude the possibility of other post-translational modifications that yield the observed receptor heterogeneity. We observed similar results for CCR5-SNAP (data not shown) indicating both receptors are similarly sialylated *in vitro*.

3.4 Discussion

3.4.1 Ligand Binding by FCS

We successfully employed FCCS to determine the equilibrium dissociation and competition affinities for the RANTES analogues with CCR5-SNAP-488. Antoine (2016) performed saturation and competition binding by FCCS on several GFP-GPCR fusion proteins, such as β2-AR and CXCR4, with fluorescently labeled small molecules and antibodies. Unlike Antoine et al. (2016), we employed the SNAP-tag to label CCR5 with Alexa-488. The SNAP-tag is advantageous to traditional labeling methods such as fluorescent proteins in that it allows different fluorophores and functional tags to be attached. Also, FCCS derived affinities are affected by the number of GFP dark states, which influence the detected number of particles. Foo (2012) showed that the GFP dark

states are caused by combination of misfolded and photobleached protein.[70] Addition of 1 mM DTT and 50 μM SNAP substrate during the labeling step yields stoichiometric receptor labeling. Antoine et al. (2016) did not purify the GPCRs from the cell lysate to remove heterogeneities which can complicate the ligand binding analysis. In our case, we purify away G-proteins and other intracellular partners that can contribute to receptor heterogeneity. For example, live cell ligand binding studies on GPCRs have revealed the existence of different receptor-ligand complexes. Ligand binding to GPCRs was determined by changes in the diffusion of the labeled ligand. In addition to observing the receptor-ligand complex, the reports also observed a second ligand-receptor species with slower diffusion but there is no consensus on the nature of this species. For example, Hegener (2004) investigated binding of fluorescent labeled Arterenol to β2-AR expressed in neuronal or alveolar epithelial cells (A549).[71] The Arterenol/β2-AR complex displayed a diffusion coefficient of 5.23×10^{-8} cm^2/s in neurons and 2.88×10^{-8} cm^2/s in A549 cells. 5 minutes after ligand treatment, 38% of receptor sites displayed a diffusion coefficient of 6.05×10^{-10} cm^2/s in neurons. On the other hand, 15 to 20 minutes after ligand treatment 40% of receptor sites displayed a diffusion coefficient of 1.01×10^{-9} cm^2/s in A549 cells. Forskolin addition shifted the receptor-ligand complex ratio from the

faster component to the slower component. We assume that the slower component arises from G-protein coupling to the Arterenol-receptor complex. Briddon (2004) and Corriden (2014) observed similar results as Hegener (2004) with a fluorescent xanthine analogue binding to the adrenergic 1 receptor (A3R) and CA200645 binding to the A3R respectively.[72, 73] Briddon (2004) showed that the fraction of ligand bound to the fast diffusing component could be reduced by competition with non-fluorescent ligands. Yet, Briddon (2004) could not compete the ligand from the slowly diffusing species and attributed this effect to ligand non-specific binding. Corriden (2014) assumed that the fast diffusing species arise from triplet state transitions and the slowly diffusing species was the receptor-ligand complex. Like Briddon (2004), Corriden (2014) shows that the fluorescent ligand can be competed with a non-fluorescent antagonist. Surprisingly, Corriden (2014) observes that the fluorescent ligand, CA200645, cannot be competed with a different antagonist indicating different receptor species.

3.4.2 CCR5-SNAP Species

We report the observation that the RANTES analogues bind to 25% of CCR5-SNAP-488 with picomolar to nanomolar affinity. GPCR solubilization with detergents is known to reduce the number of active sites. For example, Kuszak (2009) designed a μ-opioid receptor fusion with yellow fluorescent protein (YFP) in the N-terminus. Saturation binding with a μ-opioid receptor agonist revealed that the DDM/CHS solubilized receptor had only 20% of active sites of receptor in cell membranes.[74] We speculate that the remaining 75% of CCR5-SNAP-488 is irreversibly denatured during the purification

procedure. Within this 25% active fraction, the RANTES analogues bind with high affinity to 38% of active receptor and the remaining 62% fraction with low affinity. We assumed that these two receptor species corresponded to two interconvertible conformations described by the cyclic model of receptor activation.[75] We assumed these conformations were interconvertible based on structural data that shows TM6 movement is coupled to different receptor-ligand conformations.[76] We performed simulations with the data set and found that such models yield one observable K_D value indicating that the two conformations must be non-interconvertible. Previous studies by Alves showed that the neurokinin-1 receptor, another GPCR, also exhibits two non-interconvertible binding sites.[77-79] Alves (2006) conducted ligand binding measurements on purified NK-1R by SPR and calculated that substrate P had $K_{D,H} =$ 0.14 nM and $K_{D,L} =$ 1.4 nM while neurokinin A displayed $K_{D,H} =$ 5.5 nM and $K_{D,L} =$ 620 nM.[77] The two NK-1R species also couple to different intracellular pathways. The high affinity receptor species activates cAMP pathway while the low affinity receptor species activates the phospholipase C pathway. Further studies by Alves (2007) showed that the purified NK-1R consisted of several species with varying degrees of glycosylation and palmitoylation.[80] Yet, they were not able to identify which species were responsible for the pharmacology observed by SPR and cell-based functional assays. To our knowledge, we report the second study on GPCRs that detect two distinct non-interconvertible receptor species.

3.4.3 RANTES Analogues Affinities

We compared the FCCS determined K_D and K_i values to previous literature reports and we could not find any calculated K_D values for the RANTES analogues. Colin (2013) calculated K_i values for the RANTES anslogues from ^{125}I-MIP-1α competition in CCR5 expressing HeLa P4C5 cells.[81] In contrast to our results, Colin (2013) reports that 6P4 has a K_i of (0.055 + 0.02) nM and 5P12 a K_i of (0.26 + 0.13) nM. In contrast, Gaertner (2008) reported that the RANTES analogues displayed similar affinities of ~ 1 nM in competition binding experiments with ^{125}I-MIP-1β in CCR5 expressing CHO cells.[40] To complicate things further, Colin (2013) also performed competition binding with sCD4-(^{35}S-gp120) and report for 6P4 K_i = (2.93 + 0.23) nM and for 5P12 K_i = (3.51 + 1.8) nM. The results above illustrate the issue of deriving ligand affinities with different radiolabeled ligands and across different cell types. Affinities are dependent on the ligand, assay conditions, cell type, and radioactive nuclei employed. To circumvent this problem, we used purified CCR5-SNAP in a well-defined buffer-detergent system. We labeled the receptor and chemokines with Alexa fluorophores, which are inexpensive, compared to radiolabeling and they allow for simpler reaction conditions. We calculated from saturation binding experiments that 5P12-647 had a $K_{D,H}$ = (0.05 ± 0.05) nM and $K_{D,L}$ = (1.3 ± 0.5) nM and for 6P4-647 we calculated $K_{D,H}$ = (3.8 ± 0.5) nM and $K_{D,L}$ = (43 ± 11) nM. We obtained similar results for 5P14- and PSC-647 so we classified 5P12/5P14 as ultra-high affinity binders and 6P4/PSC as high affinity binders. It is interesting 5P12 and 5P14 do not activate $G\alpha_q$ while 6P4 and PSC activate $G\alpha_q$ better than RANTES. However, we cannot directly correlate the calculated K_D values with the

pharmacological properties of the RANTES analogues. To validate the saturation binding derived affinities, we performed competition binding measurements with 6P4- and 5P12-647 since PSC- and 5P14-647 bind to CCR5 similarly as 6P4- and 5P12-647 respectively. Homologous competition binding with 6P4- and 5P12-647 revealed that the non-labeled chemokines bind with similar affinities as the labeled chemokines. We performed heterologous competition binding to determine if 6P4 and 5P12 were binding to the same CCR5-SNAP-488 species. 6P4 was capable of displacing 5P12-647 and 5P12 displaced 6P4-647 from CCR5-SNAP-488. We calculated a higher affinity for 6P4 when competing 5P12-647 than in the homologous competition binding case.

3.4.4 Env Does Not Compete 5P12- and 6P4-647

We tested competition of the RANTES analogues with soluble CD4 (sCD4) in complex with gp120. The RANTES analogues were specifically designed to be potent anti-HIV therapeutics. Doranz (1999) calculated that the association half-life for sCD4 and gp120 was less than 1 minute meaning that the complex equilibrates readily at room temperature. Doranz et al. also calculated that the sCD4/gp120 complex association half-life to CCR5 in cells was 5.8 min and the dissociation half-life was 32 minutes. We incubated sCD4 and gp120 for 30 minutes at R.T. before adding the complex to CCR5 and the entire components were incubated for 16 hours at R.T. sCD4 was obtained from the NIH AIDS reagent program and BG505.SOSIPgp120 was a gift from Dr. John Moore. BG505.SOSIP was developed from BG505 by introducing several stabilizing mutations. BG505 was truncated at residue 41 in gp41 and residue 559 was mutated from

proline to isoleucine. Also, a disulfide bridge was introduced between residues 501 and 605.[82] Hoffenberg (2013) identified BG505 from a native Env sequence that preserves the most epitopes neutralized by broadly neutralizing antibodies.[83]

Competition binding with 5P12- or 6P4-647 showed that the sCD4/gp120 complex did not displace the chemokines from CCR5-SNAP-488. Garcia-Perez (2011) performed saturation binding with ^{35}S-gp120 and calculated gp120 K_D = 9.9 ± 1.2 nM. Doranz (1999) obtained similar results, K_D = 4.35 ± 0.75 nM, from saturation binding of ^{125}I-gp120 to CCR5.[84] In contrast, Garcia-Perez (2011) performed competition binding with ^{125}I-MIP-1α and non-labeled gp120 and derived K_i = 103 ± 18 nM. Colin (2013) also performed competition binding with native chemokines and RANTES analogues on ^{35}S-gp120 and ^{125}I-MIP-1α discovered two CCR5 species. ^{125}I-MIP-1α displacement with native and chemokine analogues revealed the existence of a single class of CCR5 receptors. In contrast, ^{35}S-gp120 displacement with the RANTES analogues show a single binding receptor site while the native chemokines, RANTES and MIP-1α, bound to two CCR5 binding sites. Colin et al. calculated that RANTES and MIP-1α bound to the low affinity site with K_i values greater than 1,000 nM. Gpp(NH)p treatment, a non-hydrolysable GTP analogue, decreased the fraction of MIP-1α high affinity sites without changing MIP-1α affinity. RANTES and MIP-1α bind with high affinity to the G-protein pre-coupled receptor. Nucleotide addition or pertussin toxin treatment abolishes high affinity binding of the native chemokines. In contrast, gp120 binds with high affinity the G-protein pre-coupled and un-coupled receptor. Doranz (1999) also discovered that gp120 binding to CCR5 did not depend on receptor coupling to G-protein. These findings

help explain why the RANTES analogues are potent HIV-1 inhibitors but the native chemokines are not.

3.4.5 Native Chemokines Do Not Compete 5P12- and 6P4-647

We proceeded to perform competition binding with 5P12- and 6P4-647 and non-fluorescent RANTES and MIP-1α using the same equilibration conditions as before. FCCS measurements revealed that RANTES and MIP-1α could not displace the RANTES analogues from CCR5-SNAP-488. We were surprised since we tested competitor concentrations of 10 μM and the native chemokines could not bind to CCR5-SNAP-488. Pilot saturation binding experiments with RANTES-647 showed that the affinity of RANTES must be greater than 20 nM. We were not able to derive a precise value because the cross-correlation signal was too low given the very small concentration of receptor-ligand complex. Single molecule TIRF-FRET experiments with the N-terminal SNAP-CCR5-647 fusion and RANTES- and MIP-1α-555 have shown little complex formation over several hours imaging time (data not shown in this report). Based on these results, we hypothesize the following: 1) RANTES and MIP-1α equilibrium dissociation constants must be greater than 10 μM, 2) RANTES and MIP-1α recognize a different CCR5-SNAP-488 species than the 38% active fraction or 3) RANTES and MIP-1α bind with high affinity to the G-protein pre-coupled receptor. Evidence from Colin (2013) and Garcia-Perez (2011) indicates that RANTES and MIP-1α recognize two different CCR5 binding sites with different affinity for gp120. G-protein coupling to the low affinity site shits the site to high affinity indicating that

RANTES and MIP-1α are sensitive to CCR5 coupling to G-protein. Therefore, we can reasonably assume that high affinity binding of RANTES and MIP-1α requires G-protein coupling. Given this, the RANTES analogues recognize a CCR5 binding site that is high affinity for gp120 but is low affinity for the native chemokines. Alternatively, the RANTES analogues modify the RANTES binding site by changing the receptor conformation. CCR5 coupling to G-protein allows the native chemokines to bind the gp120 high affinity site. Given this, we propose to conduct future studies with CCR5-SNAP reconstituted into nanoscale apolipoprotein bound bilayers (NABBs). NABBs are phospholipid bilayers encapsulated by two apolipoprotein belt proteins.[85, 86] Rhodopsin, the visual GPCR, has previously been incorporated into POPC NABBs and rhodopsin NABBs can activate the G-protein transducing in solution. CCR5 has also been incorporated into NABBs where thermal stability studies have shown that CCR5 is more stable in NABBs than in detergent.[85] We propose to employ NABBs to incorporate CCR5 to perform ligand-binding studies in the presence and absence of reconstituted $G\alpha_i\beta\gamma$ to determine if G-protein affect measured affinities and the fraction of low and high affinity receptors.

3.4.6 Structural Determinants of RANTES Binding to CCR5

To understand the differences from 5P12-/5P14-647 and 6P4-/PSC-647, we analyzed the N-terminus sequence of the RANTES analogues to determine which resides may be responsible for their binding affinities. We observed that PSC and 6P4 contain an aspartate residue that is not present in 5P12 and 5P14. Aspartate 6 is also conserved in

the native chemokines RANTES and MIP-1α indicating an important role of this residue on CCR5 recognition.[61] Crystal structure of RANTES bound to CCR5 is not available but Tamamis et al. (2014) reported a computational model of RANTES bound to CCR5 based on previous NMR data, previous chemokine receptor crystal structures, and mutational data.[87] The model shows that aspartate 6 forms a salt bridge with lysine 191 in CCR5. Interestingly, NMR mapping studies did not reveal changes in the chemical environment of asparate 6 during RANTES ligand binding.[88, 89] Instead, Schnur et al. (2013) and Duma et al. (2007) show that chemical shift from threonine 8 changes significantly during ligand binding. Tamamis et al. (2014) observed that threonine 8 forms hydrogen bonds with glycine 21 and asparagine 24 in CCR5. Glutamine replaces threonine 8 in both 5P12 and 5P14 so we don't expect large disruption in the hydrogen bond network. The model from Tamamis et al. also shows that serines 5 and 4 make important hydrogen bonds with aspartate 276 and lysine 22 respectively. Serines 4 and 5 are replaced by leucine 4 and methionine 5 in both 5P12 and 5P14 indicating a major disruption of the hydrogen bond network in these analogues. Given this, one might have naively assumed that 5P12 and 5P14 are weaker binders than 6P4 and PSC. Chemokine binding to CCR5 also requires several contacts with the CCR5 N-terminus and ECL2 domain.[61] Thus, we cannot exclude other contributions from CCR5 that are required for dictating chemokine affinity. Choi et al. (2012) revealed that glutamine 283 plays a fundamental role in the RANTES analogues binding and pharmacological properties.[90] Choi et al. tested the anti-HIV potencies of the RANTES analogues on wild-type CCR5 and CCR5E283A and discovered that 5P12 had 80 fold reduction in potency while both PSC and 6P4 showed enhanced potency up to 100 fold. Interestingly, 5P14 was not

affected by the E283A mutation but its potency was enhanced by the N252A mutation in CCR5. Choi et al. showed that the RANTES analogues affinities were not severely affected by the mutation ruling out that their different affinities were responsible for the changes in PIC50. Tamamis et al. in their molecular model also shows that E283 makes an important salt bridge with Ser1 of RANTES and this residue has also been shown to interact with the tropane nitrogen in Maraviroc by Tan (2013). Future NMR and x-ray crystallography experiments will shed light on the binding mode of the RANTES analogues with CCR5 and explain their different measured affinities.

3.4.7 Partial Signal Peptide Cleavage

Partial signal peptide cleavage may explain the two observed CCR5 species by FCCS and SDS-PAGE. The 5HT3a receptor signal peptide is predicted to be a cleavable signal peptide but it is possible that the FLAG tag and other receptor components can interfere with signal peptidase cleavage. We performed line-scan analysis of FLAG purified CCR5-SNAP from a representative NIR western blot to confirm if two distinct species are present in the 'monomeric' band (data not shown). Line scan analysis shows that CCR5 is composed of two distinct bands with a molecular weight difference of 2 kDa. This molecular weight difference corresponds to the molecular weight of the signal peptide. Similar band splitting has been observed for another GPCR, the glucagon-like peptide-1 receptor (GLP-1R) , which encodes for a cleavable signal peptide.[91] Ge et al. (2014) showed that although the signal peptide from GLP-1R is strongly predicted to be cleaved, the receptor undergoes partial cleavage with two distinct bands observed by western immunoblotting. Yet, expression of a GLP-1R mutant lacking the signal peptide

showed only reduction in cell surface expression with no perturbations in ligand binding or cAMP response. In comparison, Kobilka (1995) also reports a split band for a fusion protein of the β2-adrenergic receptor (β2-AR) where the signal peptide from hemagluttinin followed by a FLAG tag were fused upstream the receptor.[66] However, Kobilka reports that addition of PNGase collapses the dimer into a single band indicating that glycosylation, and not partial signal cleavage, could be responsible for the observed splitting. Furthermore, Guan et al. (1992) emphasizes that if the signal peptide is partially cleaved, then recognition by the M1 FLAG agarose would not be possible since the antibody does not recognize internal FLAG tags.[92] In our case, we employ a rabbit polyclonal FLAG antibody for NIR western immunoblotting, which does not recognize internal FLAG tags. Further experiments such as mass spectrometry will be required to assess whether the 5HT3a signal peptide is fully or partially cleaved.

3.4.8 Post-Translational Modification of FLAG Epitope

We also consider the possibility that the FLAG tag in CCR5-SNAP could be modified by phosphate or sulfate groups. The FLAG tag contains several aspartic acid residues, two lysines, and one tyrosine, all which can be phosphorylated, and/or tyrosine sulfated. Schmidt et al. (2012) and Hunter et al. (2016) have shown that the FLAG tag can be tyrosine sulfated in *E*. coli and mammalian cells.[93, 94] FLAG tag tyrosine sulfation decreases the binding affinity for the FLAG antibody. FLAG tag tyrosine sulfation can also perturb chemokine binding to CCR5 since CCR5 is also tyrosine sulfated in the N-terminus. We could not find any literature reports on FLAG tag phosphorylation but

phosphorylation can mimic tyrosine sulfation. We treated FLAG purified CCR5-SNAP with phosphatase I and analyzed the reaction product by NIR western immunoblotting (data not shown). We observed no difference in mobility between the phosphatase treated sample and the non-treated sample indicating that CCR5-SNAP is not phosphorylated. We could not test if the FLAG tag tyrosine is sulfated since there are no commercially available tyrosine-O-sulfatases.

3.4.9 Disulfide Bridge Reduction

We also considered the possibility that DTT treatment during the SNAP tag labeling step with Alexa-488 could potentially disrupt the disulfide bridges in CCR5. SNAP tag contains a catalytic cysteine, cysteine 145, that undergoes nucleophilic addition at the benzyl guanine to form a covalent bond.[55, 95] DTT addition reduces cysteine 145 so that it can undergo nucleophilic addition. However, CCR5 has two extracellular conserved disulfide bridges between cys20-cys269 and cys101-cys178.[96] The disulfide bridges are required for CCR5 proper folding. We speculate that CCR5 reduction by DTT proceeds through a long-lived intermediate capable of ligand binding. This receptor long-lived intermediate would bind with low affinity to the RANTES analogues. Rummel et al. (2013) investigated the effect of disulfide bridge reduction in CCR5 ligand binding and signaling by alanine mutagenesis.[96] Disulfide bridge removal completely abolished CCR5 ligand binding to MIP-1α and inositol phosphate (IP) accumulation in COS-7 cells indicating that the disulfide bridges are necessary for CCR5 function. In contrast, CCR1 retained ligand binding to MIP-1α with no changes in maximal binding or affinity but

(IP) accumulation was abrogated. Blanpain et al. (1999) published similar results but employed DTT treatment instead of alanine mutagenesis to abolish the disulfide bridges in CCR5.[97] Blanpain et al. treated CCR5 expressing CHO-K1 cells with 100 mM DTT for 1 hour at 37 °C and observed that MIP-1β binding was abolished. The results above show that the disulfide bridges in CCR5 are essential for ligand binding and activity but are not the case for other chemokine receptors. As such, the possibility that a long lived CCR5 intermediate that retains CCR5 conformational integrity without the disulfides is not likely otherwise binding would have been retained in the CCR5 alanine mutants or CCR5 treated with DTT. We should note that during our labeling step, we employ 1 mM DTT well below the threshold for complete denaturation observed by Blanpain et al. (1999). We have observed a small decrease in active receptor sites from DTT treatment but the DTT addition allows quantitative labeling of the SNAP tag (unpublished data). We did observe that prolonged DTT treatment on SNAP-CCR5 completely abolished chemokine binding.

3.4.10 Long-Lived Proline Conformers

GPCRs contain several conserved prolines in the transmembrane region that have been shown to be important for cell surface expression, ligand binding, and signal transduction.[98] Proline is known to undergo *cis-trans* isomerization where the two-receptor conformers could be long-lived species with distinct ligand binding profiles. Proline *cis-trans* isomerization has been shown to mediate channel opening in the 5-HT3A receptor but its role in GPCRs is less understood.[99-101] Mutagenesis analysis

on CCR5 demonstrated that proline P84 in the transmembrane 2 (TM2) was important for differentiating chemokines.[102] Govaerts et al. (2001) tested a CCR5 proline mutant, CCR5P84A, and observed reduced MIP-1α binding but no changes in RANTES binding. Govaerts et al. (2001) also observed that RANTES could signal through the mutant but not MIP-1α. This indicates that proline is required for differentiating chemokines but we would like to emphasize that alanine is not an appropriate replacement for proline. Van Arman et al. (2011) introduced several unnatural amino acids in the dopamine 2 receptor (D2R) to probe directly the effect of N-H bonding and *cis-trans* isomerization in receptor function. Incorporation of ester analogues showed that lack of N-H bonding was required for functional activity while amino acids that restored N-H bonding had perturbed activity. Furthermore, N-cyclic proline analogues with different propensities for *cis-trans* isomerization did not have major effects on D2R function. Thus, we can exclude that the two CCR5-SNAP-488 species are proline *cis-trans* isomers.

3.4.11 CCR5 Tyrosine Sulfation

CCR5 is sulfated at tyrosines 3, 10, 14, and 15 from which tyrosines 10 and 14 are important for chemokine and gp120 high affinity binding.[103, 104] Tyrosine replacement with aspartate shows inefficient ligand binding indicating that charge is not responsible high affinity chemokine binding. In contrast, phenylalanine receptor mutants showed higher viral entry than the aspartate mutants.[104] Thus, hydrophobic interactions may play a larger role in chemokine binding affinity than ionic interactions. Furthermore, it is unknown if CCR5 is heterogeneously or homogeneously sulfated at all

4 tyrosine residues. Elegant studies by Seibert et al. (2002) using a CCR5 peptide comprising of amino acid residues 2 to 18 (CCR5 2-18) point to the possibility that CCR5 can be heterogeneously sulfated.[103] CCR5 is sulfated by TPST-1 and TPST-2 but the two proteins show different sulfation kinetics and residue preferences. TPST-1 primarily sulfates tyrosine 14 while TPST-2 sulfates tyrosine 15. Subsequently, TPST-1 sulfates tyrosine 15 and TPST-2 sulfates tyrosine 14. TPST-1 incorporates sulfate to all the tyrosine residues but the major receptor species in the double-sulfated at tyrosines 14 and 15. On the other hand, TPST-2 incorporates 3 distinct sulfates to CCR5. At 24 hours post-transfection, CCR5 would be comprised of the double- and triple-sulfated species assuming that the *in vitro* kinetics observed for both TPST proteins hold in HEK293T cells. Yet, it is unclear to what extent CCR5 is sulfated in HEK293T cells or *in vivo*. Further experiments will be required to assess whether CCR5 is heterogeneously sulfated in HEK293T cells and *in vivo* and whether these species have different ligand binding properties.

3.4.12 CCR5 Glycosylation

CCR5 contains several amino acid residues that can be N-linked or O-linked - glycosylated. Farzan (1999) showed that treatment with N-glycosidase or tunicamycin did not affect CCR5 mobility in SDS-PAGE. In contrast, CCR5 treatment with O-glycosidase cocktail treatment or neuraminidase shifted CCR5 mobility by SDS-PAGE.[104] Bannert (2001) showed that CCR5 is O-linked glycosylated in the N-terminus since a CCR5 mutant lacking the first 17 amino acids could not incorporated

^{3}H-sugars. Serine 6, serine 7, threonine 16, and serine 17 in CCR5 are possible residues that can be glycosylated. Bannert (2001) showed that alanine mutations in serines 6 and 7 displayed similar mobility as the fully de-glycosylated receptor. Also, CCR5 de-glycosylation abolished MIP-1α binding in competition binding experiments. In contrast, de-glycosylation did not affect HIV-1 infection indicating that glycosylation is not required for viral binding to CCR5. Western immunoblotting analysis of CCR5 expression in macrophages showed two CCR5 species that correspond to the glycosylated and non-glycosylated species. Doring (2014) expressed CCR5 in myeloid cells deficient of alpha2,3-sialyltransferase IV (STE3Gal-IV) and discovered that RANTES binding was severely reduced.[105] Doring (2014) also showed that leukocytes deficient on STE3Gal-IV adhered poorly to carotid arteries in response to RANTES. Thus, CCR5 glycosylation is important for chemokine high affinity binding. Hauser et al. (2016) also investigated the physiological role of glycosylation in the closely related chemokine receptor CCR7. Native T cells showed marginal CCR7 sialylation while a fraction of CD45RO+ cells show strong sialylation. Likewise, CCR7 was sialylated in almost all CD3/CD28 activated T cells indicating that T cell regulates CCR7 glycosylation *in vivo*. Hauser (2016) further showed that murine cells with de-glycosylated CCR7 migrated more rapidly in response to the chemokines CCL19 and CCL21 in 2D and 3D chemotactic assays. Hauser et al. also observed that PNGaseF treated human T cells migrated better than non-treated cells in response to chemokine stimulus. Also, cells expressing de-glycosylated cells showed prolonged calcium flux responses than wild-type CCR7 expressing cells. In contrast, CCR7 alanine mutants that could not be glycosylated internalized poorly in response to chemokine stimulus. The

results demonstrate that receptor activation of different signaling pathways can be regulated by the addition or removal or post-translational modifications. Thus, we hypothesize that the two CCR5 species are the fully glycosylated and de-glycosylated species. To test this hypothesis, we treated SEC purified CCR5-SNAP and SNAP-CCR5 with α2-3,6,8,9 neuraminidase A for 1 hour at room temperature and analyzed the reaction products by SDS-PAGE. Neuraminidase treatment reduced CCR5-SNAP and SNAP-CCR5 heterogeneity but did not completely reduced the observed bands to a single band. Thus, CCR5-SNAP and SNAP-CCR5 are sialylated but receptor sialylation is not the only covalent modification present in these constructs. Future experiments, such as MALDI-TOF, will help us discern the covalent modifications present in CCR5-SNAP. Future FCCS ligand binding measurements will also help us assess whether these covalent modifications, such as sialic acid, affect chemokine binding. Also, we propose to perform experiments to assess whether CCR5 is heterogeneously modified in the immune system and the role of these modifications on receptor physiology. We have shown that FCCS is a powerful technique to discern receptor species that are averaged in cell-based functional assays. These CCR5 species are non-interconvertible and differentially recognize the RANTES analogues. Future studies with purified G-protein and CCR5-SNAP reconstituted in nanoscale apolipoprotein bound bilayers (NABBs) will show if the native chemokines can bind to CCR5-SNAP. The experiments will also help us determine the effect of G-protein on the RANTES analogues affinities and their residence on the two-receptor species. Our methodology is applicable to studying other GPCR-ligand interactions and can be generalized to broader receptor-ligand, and protein-protein interactions in solution at the single molecule scale.

Chapter 4: NANOSCALE APOLIPOPROTEIN AI BOUND BILAYERS (NABBs)

4.1 Introduction

GPCRs are highly susceptible to their lipid environment. Detergents decrease interhelical packing in the transmembrane domain and increase unfolding of the alpha helices.[106] Detergent solubilization also cause GPCRs to aggregate to minimize hydrophobic contacts with water.[107] DDM, the detergent of choice to solubilize GPCRs, maintains good interhelical packing and stabilizes GPCR flexibility. Yet, GPCRs solubilized in DDM or other detergents cannot activate G-protein and the detergents can alter the kinetics of GDP-GTP exchange. [108, 109] Given this, several methods have been devised to study GPCRs in more native hydrophobic environments that maintain receptor structure and function and allow coupling of effector proteins such as G-protein.[110] Nanoscale apolipoprotein bound bilayers (NABBs) is an example of a phospholipid bilayer system devised to solubilize GPCRs without detergents. NABBs are soluble phospholipid bilayers encircled by apolipoprotein A-I derived from zebrafish (Zap1). NABBs offer several advantages over detergent micelles and liposomes, such native bilayer environment, retention of wild-type stability and function, and control of oligomeric state and lipid environment. Rhodopsin incorporated into POPC NABBs showed thermal stability comparable to Rhodopsin in rod outer segments (ROS) and greater than Rhodopsin solubilized in DDM.[86] Also, Rhodopsin incorporated in NABBs can activate the visual G-protein, transducin. Further studies on CCR5 revealed similar thermal stability from CCR5 solubilized in micelles. CCR5 NABBs denatured at

the temperature of 54.5 °C while CCR5 in Buffer N denatured at 47.1 °C.[85] Small molecules such as Maraviroc and Vicriviroc also stabilized CCR5 by shifting the melting temperature of the receptor. Thus, NABBs are a suitable lipid system to study GPCRs in a native environment.

However, NABBs are expensive to work with since Zap1 does not express well in bacterial cultures with protein yields around 10 mg/L culture. Given this, we systematically optimized the expression and purification conditions for Zap1 to increase protein yield and purity. We designed a codon optimized construct, ZapN1, for higher expression in *E*. coli and performed single colony screening for protein expression. We found that double-screened colonies expressed ZapN1 at higher quantities than the single screened colonies. We optimized induction time for single and double-screened colonies and monitored ZapN1 expression every hour after induction. We observed that induction at $O.D._{600}$ 0.8 and 3 hours incubation time gave the highest ZapN1 expression. We tested ZapN1 expression at 16, 23, 30, and 37 ° C for 3 hours and discovered that ZapN1 expressed better when cultures where incubated for 3 hours at 30 °C. We also optimized purification of ZapN1 in batch to increase yield and purity. Large-scale expression of ZapN1 using the optimized expression and purification conditions yielded 250 mg/L culture of ZapN1.

NABBs assembly is also limited by the number of reactions that can be performed simultaneously. To address this problem, we designed and built a custom platform to support mini-scale batch columns for high-throughput chromatography at RT and 0 °C. NABBs assembled with POPC are heterogeneous and this heterogeneity can complicate single molecule analysis and NABBs stability over time. Given this, NABBs assembly

with DLPC yielded near-homogeneous NABB preparations. We optimized NABBs assembly with DLPC and showed that 95 lipids/ZapN1 give near-homogeneous preparations and the assembly conditions are compatible with the detergents and additives used in GPCR solubilization. We reconstituted Rhodopsin labeled with Fluorescein (Rho-Fl) into DLPC NABBs and showed that Rho-Fl is successfully incorporated into NABBs and the particles have the expected size. We then show that CCR5 incorporated into DLPC NABBs (CCR5-NABBs) can bind 2D7-Cy5 and we calculated a K_D value of 5.5 nM. Future experiments will employ CCR5-NABBs to perform saturation and competition binding with the RANTES analogues to validate the results obtained in micelles. We will also reconstitute CCR5-NABBs with purified $G\alpha_i\beta\gamma$ to determine if G-protein pre-coupling affects chemokine affinity and the ratio of the high and low affinity receptor fractions.

4.2 Materials and Methods

4.2.1 SDS-PAGE Analysis

Cell pellets were solubilized in 100 µl of lysis buffer A (150 mM NaCl, 1% Triton X-100, 50 mM Tris pH 8.0) and sonicated for 10 seconds in a Branson 1200 sonicator. Samples were centrifuged at 17,800 rpm for 5 minutes in an IEC Micromax microcentrifuge. 6.5 µl of cell lysate supernatant or Ni fraction was added to 2.5 µl of NuPAGE loading dye buffer and 1 µl of NuPAGE reducing agent in a 1.0 ml Eppendorf microcentrifuge tube. Samples were heat-denatured by placing them in a boiling water

bath for 10 minutes. The denatured samples were then applied to individual wells of a 4-12% Bis-Tris NuPAGE gel (1.0 mm) in MES-SDS buffer (50 mM MES, 50 mM Tris Base, 0.1% SDS, 1 mM EDTA, pH 7.3). Electrophoresis was carried out with a voltage of ≤ 200 V. The gel was then stained for 30 minutes in Coomassie Brilliant Blue-R G250 staining solution and destained by several washes of destaining solution and water.

4.2.2 Double Screening for Apolipoprotein Expression

BL21-Gold (DE3) cells (Agilent Technologies, Catalog # 230132) were aliquoted (10 µl) with 50 ng of plasmid DNA and incubated in ice for 30 minutes. Cells were then transformed by heat-shocking at 42°C for 20 seconds in a water-bath. 190 µl of SOC media was added to each sample and incubated at 37°C with shaking at 1,100 rpm for 1 hour in a Thermomixer compact (Eppendorf, Order # 022670051). Bacterial samples (20 and 180 µl per sample) were then plated onto LB-agar kanamycin plates (50 µg/ml final concentration) and incubated at 37°C for 12-16 hours. Single colonies were selected to inoculate 10 ml of Terrific Broth (TB) media in 13 ml polypropylene culture tubes (Sarstedt, Item I.D. 368625). Bacterial cultures were incubated at 37°C and induced with 1 mM IPTG when the $O.D._{600}$ reached a value of ~ 0.6. Cultures were then incubated for an additional 3 hours at 37°C. 5 ml of each culture were collected in individual 1.5 ml Eppendorf microcentrifuge tubes. Also, 1 ml of each culture was used to make glycerol stocks by adding an equal part of sterile 50% glycerol in water (v/v) in a cryogenic vial (Thermo Scientific, Catalog # 375418).

4.2.3 Generation of Bacterial Growth Curves

A 5 ml LB culture with kanamycin (50 μg/ml final concentration) was inoculated from a glycerol stock of BL21-Gold (DE3) cells previously transformed with ZapN1 that were either randomly selected or double-screened for protein expression. The culture was incubated at 37°C for ≤ 16 hours with shaking at 200 rpm. Then, 100 ml TB cultures with kanamycin (in 250 ml Pyrex Flasks) were inoculated with 500 μl of the starter culture (1:200 dilution) and incubated at 37°C with shaking at 200 rpm. Every hour or 30 minutes, 1 ml sample of each culture was removed for $O.D._{600}$ measurements in methacrylate, 4.5 ml cuvettes with a 10 mm light path (Fisherbrand, Catalogue # 14-955-130). $O.D._{600}$ measurements were obtained using a SmartSpec 3000 spectrophotometer (Bio-Rad, Catalogue # 170-2501) before and after addition of IPTG. Bacterial cultures were induced with 100 μl of 1M IPTG when they reached $O.D._{600}$ values of 0.5, 0.8, and 1.2. Every hour after induction, 1 ml samples of each culture were collected in 1.5 ml Eppendorf tubes and stored at – 20°C.

4.2.4 Temperature Effects on Expression of ZapN1

8 ml LB cultures with kanamycin (50 μg/ml final concentration) were inoculated from glycerol stocks of BL21-Gold (DE3) cells previously transformed with ZapN1 that were either randomly selected or double-screened for protein expression. The starter cultures were incubated at 37°C for ≤ 16 hours with shaking at 200 rpm. Then, 100 ml TB cultures with kanamycin (in 250 ml Pyrex Flasks) were inoculated with 500 μl of each

starter culture (1:200 dilution) and incubated at 37°C with shaking at 200 rpm. When cultures reached an $O.D._{600}$ value of ~0.8, ZapN1 expression was induced by the addition of IPTG (1 mM final concentration). Then, cultures were incubated at four different temperatures (37, 30, 23, and 16°C) for a span of 3 hours each. Each hour after induction, 1 ml samples per culture were collected in 1.5 ml Eppendorf tubes and $O.D._{600}$ values were recorded as mentioned previously.

4.2.5 Small Scale Purification of ZapN1

100 ml TB cultures that were previously inoculated with single or double-screened samples were incubated at 37°C until the $O.D._{600}$ reached ~0.8 at which then IPTG (1 mM final concentration was added). Cultures were then incubated at 30°C for 3 hours with shaking at 200 rpm. Cells were harvested every hour post-induction by centrifuging at 3,000 rpm, 4°C in 250 ml ultracentrifuge conical tubes (Corning, Catalogue # 25350-250) in a Beckman CS-6R Centrifuge. Cell pellets were thawed from – 80°C on ice and then solubilized in 5 ml of lysis buffer B (40 mM Tris, 0.3 M NaCl, 5 mM 2-mercaptoethanol, 2 mM phenylmethanesulfonyl fluoride (PMSF), 10 µg/ml aprotinin, 5 µg/ml leupeptin, 1% Triton X-100, 1 EDTA-free protease inhibitor-table (1 tablet per 50 ml of buffer), pH 8.0). Cell samples were then incubated on ice for 30 minutes with vortexing every 15 minutes. Samples were then spun for 30 minutes at 4°C, 30,000xg in polypropylene ultracentrifuge clear tubes, using a JA-17 rotor in a Beckman Avanti J-25 centrifuge. 600 µl of His60 Ni Superflow resin (Clontech, Catalogue # 635660) was loaded into a Poly-Prep chromatography column (Bio-Rad, Catalogue # 731-1550, 6

columns total) and equilibrated with 5 ml of Equilibration buffer (50 mM sodium phosphate, 300 mM NaCl, 20 mM imidazole, pH 7.4). After centrifugation, the supernatant from each sample was loaded into the equilibrated resin. ZapN1 was allowed to bind the resin by gravity flow. The resin was then washed with 5 ml of wash buffer (50 mM sodium phosphate, 300 mM NaCl, 40 mM imidazole, pH 7.4). To elute ZapN1 from the columns, 1.5 ml of elution buffer (50 mM sodium phosphate, 300 mM NaCl, 300 mM imidazole, pH 7.4) was added twice to the resin and collected in 2 ml Eppendorf tubes. To analyze the efficiency of ZapN1 purification, 6.5 µl of the flow through, wash elution, and fractions were aliquoted for SDS-PAGE analysis as described previously.

4.2.6 Large Scale Expression and Purification of ZapN1

1 L TB cultures (with kanamycin at 50 µg/ml final concentration) were inoculated (1:200 dilution) with a previously grown culture of BL21-Gold (DE3) cells that were double-screened for ZapN1 expression. The 1 L cultures were then incubated at 37°C with shaking at 200 rpm. ZapN1 expression was induced by the addition of IPTG (1 mM final concentration) when the cultures reached an $O.D._{600}$ of ~0.8. Then, the 1 L cultures were incubated for 3 hours at 30°C with shaking at 200 rpm. Cells were harvested by centrifuging the samples at 2,000 rpm for 20 minutes in a J6-HC Beckman centrifuge. Cell pellets were then stored at – 80°C. Cell pellets were thawed to 4°C before solubilizing in 50 ml total of lysis buffer B. The cell mixture was then incubated on ice for 30 minutes. The cell lysate was then sonicated on ice by using a Misonix Sonicator 3000 with an output level of 10, ON time 10 seconds, OFF time 10 seconds, for a total

time of 1.2 minutes. After sonication, the cell lysate was placed into polypropylene tubes and centrifuged at 30,000xg for 30 minutes at 4°C using a JA-17 rotor in an Avanti J-25 centrifuge (Beckman). The supernatant was then applied to 15 ml of His60 Ni Superflow resin previously equilibrated with 10 CVs (150 ml) of equilibration buffer and incubated overnight at 4°C. The resin was then applied to a column and washed with 10 CVs of wash buffer. ZapN1 was then eluted with 10 x 5 ml of elution. To analyze the ZapN1 content of each fraction, SDS-PAGE analysis was performed as described previously. Fractions containing ZapN1 were concentrated and desalted using an Amicon Ultra-15 centrifuge filter unit with a molecular weight cutoff of 10,000 Da (Millipore, Catalogue # UFC901024). ZapN1 was dialyzed twice against 50 mM ammonium acetate in a Slide-A-lyzer Dialysis cassette with a molecular weight cutoff of 3.5 kDa (Pierce, Product # 66130). Samples were then aliquoted, lyophilized using a SpeedVac SC100, and stored at -80°C.

4.2.7 Triton X-100 Removal from Purified ZapN1

250 mg lyophilized ZapN1 is solubilized in 5 milliliters 6 M guanidinium hydrochloride for 1 hour at 4 °C. Meanwhile, 1 ml of His60 Superflow Ni resin is washed with 10 ml Millipore grade water and then equilibrated with 10 ml buffer (50 mM sodium phosphate, 300 mM NaCl, 10 mM imidazole, 6M GuHCl, pH 7.4). ZapN1 is added to the resin and allowed to bind overnight at 4 °C in a 50 ml vessel. The resin is added onto a disposable Poly-prep and allowed to settle by gravity flow. The resin is then washed with 50 mM sodium phosphate, 300 mM NaCl, 10 mM imidazole, pH 7.4 with decreasing

concentrations of guanidinium hydrochloride (4, 2, 1, and 0.5 M) in steps of 5 ml. The resin is then washed in 10 ml of 50 mM sodium phosphate, 300 mM NaCl, 10 mM imidazole, pH 7.4) to remove remaining traces of guanidinium hydrochloride. The resin is then washed with another 10 ml of the same buffer as above supplemented with 1% sodium cholate followed by another 10 ml buffer without detergent. ZapN1 is eluted from the resin 8 1 ml fractions using 50 mM sodium phosphate, 300 mM NaCl, 300 mM imidazole, pH 7.4. Fractions were analyzed by SDS-PAGE and the peak fractions were pooled together, aliquoted, and snap frozen in liquid N_2 for long term storage at -80 °C.

4.2.8 Construction of High Throughout Chromatography Platforms

We designed a platform that allows for simultaneous, high-throughput, mini-scale chromatography at either RT or 0 °C. Platform was designed so that any 96-well plate could be placed below for sample collection. We took dimension measurements from a 96 well plate (Fisher Scientific, Round Bottom 96 well plate, Natural, Polypropylene, Catalogue Number 12-565-502) as a basis for the platform. We also acquired measurements for the pins in the B2 position in the EpMotion 5070 so that the platform could fit between pins. We took this approach since we could automate fluid dispensing with the EpMotion. The measured distance between pins was 102 mm (width) and 54 mm (height) for the inside distances. For the external distances, a 96 well plate was measured and obtained a width of 127.3 mm and a height of 85 mm. Based on the dimensions of the 96 well plate, an adobe illustrator file was made for the plate (Figure 4.2.8a)

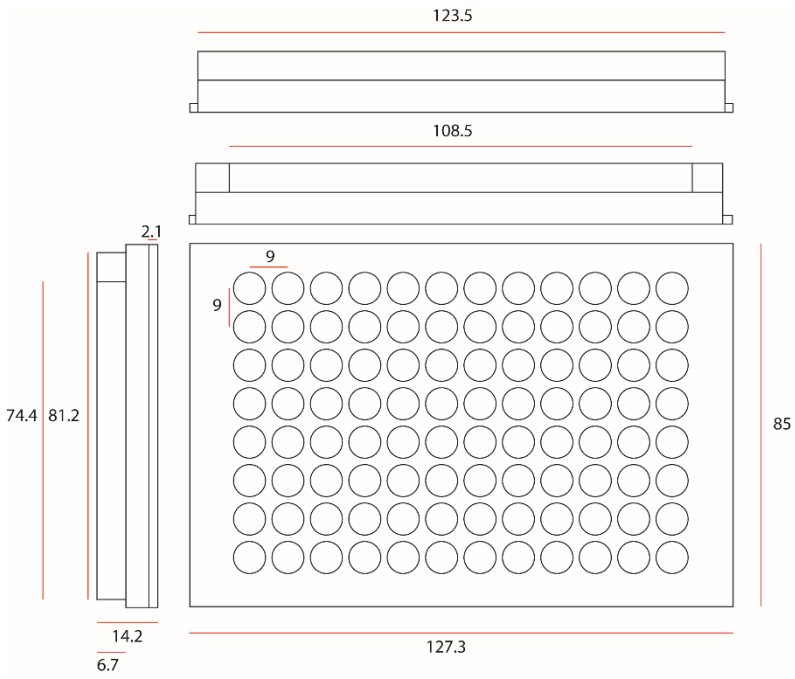

Figure 4.2.8a. Dimensions of a 96-well plate. The red lines indicate the distance between two points and the numbers adjacent to the red lines indicate the length in mm.

To design the platform, we used a box design and modify the dimensions to fit the 96 well plate and the pins in the Eppendorf 5070 (Figure 4.2.8b). We designed two different models that would accommodate mini-scale chromatography purifications at different temperatures. We designed a top that accommodates 24 simultaneous purifications for 0 °C. We designed a second top that accommodates 96 simultaneous purifications for RT. We made the tops compatible with the walls of the platform so that they could be interchanged.

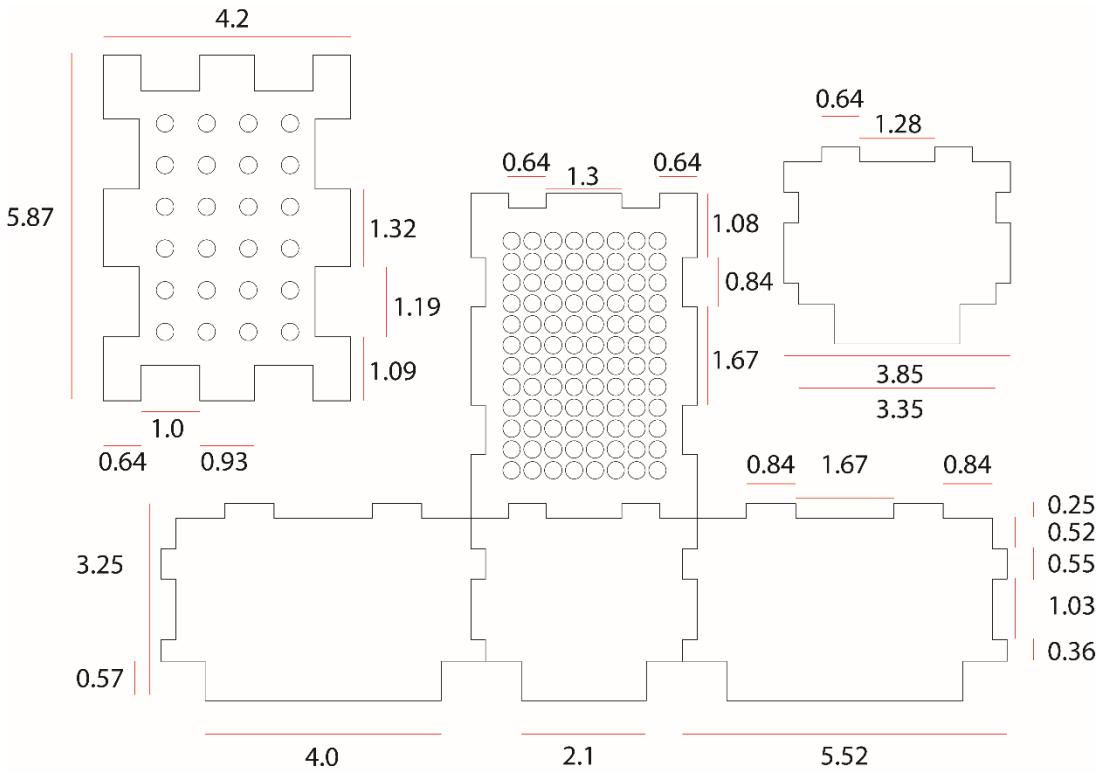

Figure 4.2.8b Dimensions of the high-throughput chromatography platform. The red lines indicate the distance between two points in inches.

For the top of the box, we imposed the drawing made in illustrator for the 96-well plate into the corresponding section of the box. For the 24-sample holder, every other well was deleted such that the top could slide into three different positions in the box and allow fractions to be collected in the same plate. To determine the height of the box, we determined the height of the disposable columns (Extract Clean 1.5 ml reservoir part# 210001/5122381) to be used with the platform to be 65 mm. The height of the column was then added to that of the 96 well plate and 5 mm were added to allow space between the column and the plate for a total height of 78.72 mm. Adobe illustrator files were converted into AutoCAD files for printing the files into plastic. To design the RT box, we employed a VLS 6.60 Laser Cutter and used Cast Colorless Acrylic plastic from

McMaster Carr. To print the 0 °C platform, we employed a 3D PROJET 3510 HD (Plus) printer and used M3 crystal as the material. The RT platform was assembled manually using epoxy glue to hold the individual pieces together.

4.2.9 Assembly of NABBs

1.5 ml columns (Extract Clean 1.5 ml reservoir part# 210001/5122381) are washed with 1 ml 100% ethanol to prime the membrane and allow aqueous solutions to pass through. The columns are then washed with 2 x 1 ml Millipore grade water to wash residual ethanol. Re-suspended detergent removal resin (Pierce Detergent Removal Spin Columns, 4 ml, Prod #97779) is added to each column until 1 ml of packed resin has filled the column. Resin is then equilibrated in 2 ml of Buffer G (10 mM Tris, 0.15 M NaCl, pH 8.0, for empty NABBs) or Buffer C (20 mM HEPES pH 7.4, 0.1 M $(NH_4)_2SO_4$, 1 mM $CaCl_2$, 5 mM $MgCl_2$, 10% glycerol, for GPCR-loaded NABBs). NABBs samples are then added onto the resin and allowed to enter by gravity flow. NABBs are eluted in 4 x 150 µl fractions of buffer and collected in polystyrene 96 well plates. Fractions are analyzed by measuring the 280 nm absorbance to determine the NABB peak fractions. Peak fractions are pooled and utilized for SEC and native PAGE.

NABBs reaction were assembled by mixing all the components in 1.5 ml Eppendorfs and incubating the reactions on ice for 30 minutes prior to detergent removal. Reagent concentrations were determined based on the concentration of ZapN1 used for the reactions. For 75 and 55 POPC NABBs, ZapN1 was added to a final concentration of 90 µM and 1.5% sodium cholate (w/v). For all other NABBs assembly except for receptor

loaded NABBs, ZapN1 was added to a final concentration of 200 µM and 2% (w/v) sodium cholate for total reaction volume of 150 µl. Lipid stocks were made in 7.5% (w/v) sodium cholate which is known to yield more homogeneous preparations than CHAPS or DDM. Lipids are added at a stoichiometric factor relative to the concentration of ZapN1. For example, for 95 DLPC NABBs, DLPC is added to a final concentration of 95 x 200 µM or 19 mM for a total reaction volume of 150 µl. Buffer G or Buffer C is then added to each reaction to bring the final volume to 150 µl. Additives such as DDM, CHS, and glycerol are added to each NABB reaction at a final concentration (w/v) relative to the final volume of 150 µl. For Rhodopsin-Fluorescein loaded NABBs, ZapN1 was added to a final concentration of 100 µM and Rhodopsin-Fluorescein 2 µM in 6 mM DLPC (60 DLPC per ZapN1) in a total reaction volume of 150 µl. Sodium cholate was kept at 2% (w/v) total concentration for Rhodopsin-Fluorescein NABBs. Rhodopsin-Fluorescein NABBs were eluted in Buffer G. For CCR5-SNAP-488 NABBs, ZapN1 and sodium cholate concentration was kept the same as the Rhodopsin-Fluorescein NABBs. CCR5-SNAP-488 was 1D4/FLAG purified as described previously and added directly to the NABB reaction without SEC purification step. 70 µl CCR5-SNAP-488 FLAG elution was added to the DLPC/ZapN1/sodium cholate mixture to bring the final volume to 150 µl. CCR5-SNAP-488 NABBs were eluted in Buffer C and then used for 2D7-Cy5 binding studies or analyzed by SEC and SDS-PAGE.

4.2.10 Native PAGE Analysis

16 µl sample is mixed with equal parts native sample buffer (Bio-rad, catalog# 161-0738, 62.5 mM Tris-HCl, pH 6.8, 40% glycerol, 0.01% bromophenol blue) in individual 1.0 ml Eppendorfs. Samples are loaded into a 4-20% Mini Protean TGX gel immersed in 1x TBE buffer (90 mM Tris base, 80 mM boric acid, 3 mM EDTA, pH close to 8.35) at 16 °C. To analyze NABB particles, the following voltage sequence is used

1. 20 V for 15 minutes.
2. 70 V for 20 minutes.
3. 150V for 12 hours.

Gels are removed from the cassette and stained in Coomassie Brilliant Blue solution (50% methanol, 10% glacial acetic acid, 0.1% Coomassie Brilliant Blue) for 30 minutes at RT and destained with several washes of destaining solution (50% methanol, 10% glacial acetic acid).

4.2.11 Size Exclusion Chromatography

Superdex 200 10/300 GL column is equilibrated with at least 1 CV of Buffer G or Buffer C prior to addition of the NABB samples. NABBs are injected into the column and then eluted over 1 CV in the appropriate buffer with a flow rate of 0.25 ml/mn. 0.5 ml fractions are collected in 1.0 ml tubes and protein elution is monitored using 280 nm absorbance. Fractions are analyzed by native PAGE to determine the peak fractions. If

the column would be used subsequently for more NABB purifications, then the column is washed with 1 CV of the appropriate buffer before loading the NABB sample.

4.2.12 Rhodopsin Purification from Rod Outer Segments

ROS membranes are thawed on ice for 1 hour in the dark and then 500 µl 1% DDM solution in 1x PBS supplemented with protease inhibitor tablets is added to the membranes. Samples are incubated for 2 hours at 4 °C and then centrifuged using the TLA 100.3 rotor at 100,000xg for 30 minutes at 4 °C using the Optima TL ultracentrifuge. Supernatant is transferred to a 15 ml vessel containing 1 ml 50% 1D4 mAb Sepharose 2B resin and 4 ml 1x PBS. Sample is then incubated for 16 hours at 4 °C to allow Rhodopsin to bind the resin. Resin is transferred to a clean 1.5 ml Eppendorf and 0.5 ml reaction buffer (0.1% DDM (w/v) in 1x PBS, pH 7.2) is added to the resin. Sample is incubated with constant nutation for 30 minutes at 4 °C and then spun down to pellet the resin at 5,500 rpm. Supernatant is removed from the resin and the resin is washed one more time with reaction buffer as before. Resin is re-suspended in 1.0 ml reaction buffer and 1.5 µl of 23 mM Fluorescein-maleimide is added to the sample. Rhodopsin is labeled with Fluorescein at 25 °C for 20 hours with constant vortexing. To stop the reaction, resin is pelleted at 4 °C for 2 minutes and the supernatant is discarded. Resin is re-suspended in 1.0 ml reaction buffer and washed for 30 minutes at 4 °C with constant nutation. Resin is pelleted as above and the supernatant removed from the resin. Resin is washed 4 more time in reaction buffer as above to remove any trace fluorophore. Resin is re-suspended in 1.0 ml low salt buffer (0.1% (w/v) DDM, 2 mM sodium phosphate, pH 6.0) and

washed for 30 minutes at 4 °C with constant nutation. Resin is pelleted as above and then Rhodopsin-Fluorescein (Rho-Fl) is eluted from the 1D4 resin by adding 500 µl elution buffer (0.33 mg/ml 1D5 peptide in 0.1% DDM (w/v), 2 mM sodium phosphate, pH 6.0) and incubating on ice for 1 hour. Sample is pelleted as above and the supernatant is collected in a separate 1.5 ml Eppendorf. Elution buffer is added one more time as above and Rho-Fl is eluted one more time. 1D4 elution fractions are pooled together and 5 M NaCl is added to a final concentration of 0.15 M. Rho-Fl is characterized by UV-Vis spectroscopy.

4.2.13 FCS and FCCS Measurements

For antibody binding to CCR5-SNAP-488 NABBs, CCR5-NABBs were mixed with 2D7-Cy5 at various antibody concentrations (1, 2, 4, 8, 16, and 32 nM) for a total reaction volume of 100 µl. Samples were incubated for 30 minutes at RT protected from ambient light. Samples were loaded into # 1.5 glass bottom 96 well black plates and mounted in an inverted laser scanning confocal microscope LSM 780 (Zeiss). Alexa-488/Fluorescein was excited using an Argon 488 nm laser at 0.8% or 1.0% laser transmission and Cy5 was excited using a Helium-Neon 633 nm laser line at 4.0% laser transmission. Laser excitation was focused into the sample by using a 40x C-Apochromat NA 1.2 water immersion objective. Correction collar was adjusted in the objective to 0.17 and room temperature and focal depth set at 50 µm (CCR5 NABBs) or 200 µm (Rho-Fl NABBs) above the glass by performing a line scan using reflected light from the 488 nm laser line. For 488 nm excitation, a 488 only main beam splitter (MBS) was used and for

633 nm and dual excitation a MBS 488/561/633 was used. Emission from Alexa-488 or Fluorescein was collected in the range of 516 – 596 nm using a GaAsP detector and emission from Cy5 in the range of 656 – 750 nm using a PMT detector. Pinholes for both excitations were set to 1.0 airy units and aligned along the xy plane using a solution of free dye or the sample itself. Count-rate binning time was set to 1 ms and the correlator binning time was set to 0.2 µs. Count rates were never greater than 500 kHz and traces showing large deviations from the average or decaying/increasing fluorescence were manually removed from the analysis. Counts per molecule (CPM) values were between 1-16 kHz for all measurements to avoid optical saturation while maximizing counts above background. For Rho-Fl NABBs, 10 repetitions of 10 seconds each were collected and averaged while for CCR5-SNAP-488 NABBs binding to 2D7-Cy5 50 repetitions of 10 seconds each were collected and averaged. For 2D7-Cy5 binding to CCR5-SNAP-488 NABBs, cross-correlation curves were fitted using equation 3.3 and the auto-correlation curves were fitted using the equation below:

$$G(\tau) = \frac{\gamma}{N}\left(\frac{1}{\left(1+\left(\frac{\tau}{\tau_{D1}}\right)\right)}\frac{1}{\sqrt{1+\left(\left(\frac{w_{xy}}{z}\right)^2\left(\frac{\tau}{\tau_{D1}}\right)\right)}} + \frac{1}{\left(1+\left(\frac{\tau}{\tau_{D2}}\right)\right)}\frac{1}{\sqrt{1+\left(\left(\frac{w_{xy}}{z}\right)^2\left(\frac{\tau}{\tau_{D2}}\right)\right)}}\right)\left(1+\frac{T_t e^{-\frac{\tau}{\tau_t}}}{1-T_t}\right)+1$$

(Equation 4.1)

Where the second translational component is to account for NABB aggregates that are present in the solution or the 2D7-Cy5 bound to CCR5-SNAP NABBs. To fit the Rho-Fl NABBs data, we employed the following equation

$$G(\tau) = \frac{\gamma}{N}\left(\frac{1}{\left(1+\left(\frac{\tau}{\tau_D}\right)\right)}\frac{1}{\sqrt{1+\left(\left(\frac{w_{xy}}{z}\right)^2\left(\frac{\tau}{\tau_D}\right)\right)}} + R_a e^{\frac{-\tau}{\tau_r}}\right)\left(1+\frac{T_t e^{-\frac{\tau}{\tau_t}}}{1-T_t}\right)+1 \text{ (Equation 4.2)}$$

Where we included a rotational component that is dependent on translational diffusion. R_a is the rotational amplitude and τ_r is the rotational diffusion time. Concentrations for the fluorescent species were derived as described previously.

4.2.14 Negative Stain Transmission Electron Microscopy

SEC purified DLPC NABBs (empty or with CCR5-SNAP) were diluted in Buffer G or Buffer C at the following concentrations: 10 µg/ml, 5 µg/ml, and 1 µg/ml for EM sample staining. Carbon-coated 200 mesh copper grids were glow discharged for 20 seconds and then 10 µl of was applied directly to the copper grid and incubated for 2 minutes at R.T. Excess sample was blotted using a kimwipe and the grid was washed twice with 10 µl of Millipore water. The grid was stained in 10 µl of 1% aqueous uranyl acetate previously filtered using a 0.45 µm membrane. The staining was repeated twice and in the last staining step the stain was allowed to sit on the grid for 2 minutes at R.T. Excess stain was removed using a kimwipe making sure to leave behind a thin film of stain. Grids were air-dried for 10 mns and then stored at R.T. until imaging. Images were acquired using a JEOL 1400 Plus transmission electron microscope with Gatan 2K x 2K digital

camera. Electron beam energy was set at 120 kV and images were acquired at 25,000x magnification with size of 2048 x 2048 pixels and exposure time of 1 second.

4.2.15 Atomic Force Microscopy on NABBs

Fluid imaging of SEC purified empty NABBS or SNAP-CCR5 NABBs was performed using a Cypher ES AFM (Asylum Research), with a silicon probe (nominal spring constant, k = 2 N/m) in tapping mode at RT. 45 µl of buffer G or buffer C was plated on freshly cleaved mica substrate (SPI) for ~10 seconds before adding 5 µl of the NABBs solution for a final dilution of 1:10. The mixture was incubated for ~ 30 seconds, and then washed with 5 ml of the same buffer to remove excess NABBs in solution. The scan size was 500 nm x 500 nm. Raw data was exported into tiff images using the Asylum Research's Igor Pro software for analysis.

Tiff exported images were then imported into FIJI/ImageJ (NIH) for quantification of height, volume, and diameter of NABBS. A FFT bandpass filter was first applied to the image, and then an unsharp mask filter was applied to allow for segmentation of individual NABB structures. An auto threshold was applied to the image and the thresholded image was converted into a binary image. Using the watershed irregular features plugin in the BioVoxxel Toolbox in FIJI, the NABBs were segmented. An average intensity measurement was converted into an average height measurement for each individual NABB. A Feret's diameter measurement was used to get the diameter of individual NABBs. Volume measurements were calculated using equation 4.3

$$V = I_{avg} \cdot Z_{conversion} \cdot A_p \cdot XY_{conversion}{}^2 \quad \text{(Equation 4.3)}$$

where I_{avg} is the average intensity, $Z_{conversion}$is the conversion of one gray scale unit of intensity into height in nanometers, $XY_{conversion}$ is the pixel to nanometer conversion for the image in xy, and A_p is the area of particles or NABBs in pixels. In addition, images were exported with a 3x3 median filter to reduce the noise seen in images for the figures.

4.2.16 Receptor SDS-PAGE Analysis and Western Immunoblotting

SEC purified CCR5-SNAP-488 NABB fractions were mixed with DTT at 150 mM final concentration and NuPAGE loading buffer. Samples were loaded into a NuPAGE 4-12% Bis-Tris gel in MES-SDS buffer. Electrophoresis was conducted at a constant voltage of 100V. The gel was removed from the cassette and rinsed in water for 5 minutes at RT. 1 piece of Immobilon PVDF membrane was incubated for 1 minute at room temperature in 100% methanol. The PVDF membrane and 2 pieces of extra thick blot papers (Bio-rad) were rinsed in 1x Fast Semi-Dry transfer buffer for 10 minutes at RT. Western transfer was performed in a semi-dry apparatus for 7 minutes with a constant voltage of 25V. After electrophoresis, the membrane was placed in 10 ml of 5% Milk in 1x TBST for 1 hour at room temperature. The membrane was then placed in 10 ml of blocking buffer with anti-1D4 mouse monoclonal (1:3,000). The membrane was incubated overnight at 4 °C. Membrane was then washed 3x5 minutes in 1x TBST. Membrane was incubated for 30 minutes at RT in 10 ml blocking buffer supplemented with anti-mouse horseradish peroxidase (HRP) conjugated secondary antibody (1:10,000). Membrane was washed

again 3x5 minutes in 1x TBST. Solution was removed and the membrane was treated Femto substrate (Thermo Scientific) for 1 minute at RT. Excess solution was removed and the autoradiography film was exposed to the membrane in the dark at various time intervals. Images were scanned using a scanner and analyzed using ImageJ.

4.2.17 Data Analysis and Processing

All Coomassie stained gels were analyzed using a BioSpectrum 500 Imaging System (Ultra-Violet Products) with a LED white illuminator. Images were acquired with an exposure time of 4 seconds and a gain of 581. Data analysis was performed using Microsoft Excel 2010 unless stated otherwise. Figures were made using Adobe Photoshop CC and Illustrator. To fit the saturation binding isotherm of 2D7-Cy5 binding to the CCR5-SNAP-488 NABBs, we employed the equation below

$$y = \frac{B_{max} * L}{K_D + L} \qquad \text{(Equation 4.4)}$$

Where y is the fractional occupancy and L is the concentration of free labeled antibody. Equation 4.4 was fitted using GraphPad Prism.

4.3 Results

4.3.1 Double Screening of Cultures for ZapN1 Expression

Double selection or screening relies on performing two rounds of antibiotic pressure on single colonies plated on LB agar plates. Single colonies are screened for protein expression in small-scale cultures. The highest expressing culture is then re-plated onto a fresh LB agar plate and then single colonies are re-screened for protein expression. We performed double screening on BL21 (DE3) transformed with ZapN1, Zap1, and the commercially available membrane scaffold protein MSP1D1. Transformed bacterial cultures were plated onto LB agar-kanamycin plates and single colonies were grown in 5 ml LB cultures. Cultures were pelleted, lysed, and analyzed by SDS-PAGE to determine which colonies expressed the proteins at the highest levels. Cultures were then screened twice as described previously. Figure 4.3.1 shows the SDS-PAGE analysis of the 3 highest colonies from the 1st and 2nd rounds of screening.

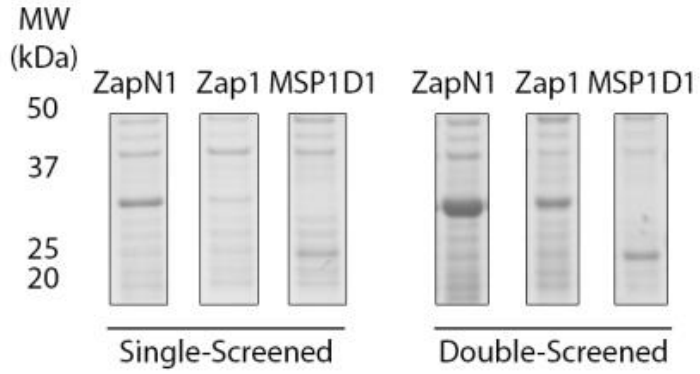

Figure 4.3.1 Screening for Apolipoprotein Expression in BL21-Gold (DE3) Single Colonies. Coomassie Brilliant Blue-stained polyacrylamide gels showing BL21-Gold (DE3) cell lysates that expressed the highest levels of apolipoproteins from $n \geq 3$ screened colonies. The first panel shows cell lysates from the first round of screening while the second panel shows samples that underwent a second screening. The double-screened samples were selected from the glycerol stocks of the highest expressing colonies of the first panel.

ZapN1 and Zap1 run as a single molecular species of 30 kDa molecular weight. MSP1D1 runs at a molecular weight of 25 kDa. The 3 apolipoproteins express in BL21 (DE3) cells but ZapN1 expresses higher than the non-codon optimized construct Zap1 and MSP1D1. Double screening increased expression of all 3 apolipoproteins but ZapN1 increased more than Zap1 and MSPS1D1. For subsequent expression optimization experiments, we employed the single and double-screened ZapN1 colonies that had the highest protein expression.

4.3.2 Optimization of Induction and Incubation Time

ZapN1 expression was assessed on single and double-screened BL21 (DE3) cultures that were induced with IPTG at different $O.D_{600}$ values of 0.5, 0.8, and 1.2. We monitored bacterial growth before and after induction by taking $O.D_{600}$ measurements periodically. After induction, 1 ml samples were taken from each culture to determine ZapN1 expression at every hour by SDS-PAGE analysis. Figure 4.3.2 shows the bacterial growth curves for single and double-screened cultures induced with IPTG at various $O.D_{600}$ values. Figure 4.3.2 also shows the Coomassie blue stained SDS-PAGE gels for bacterial samples taken every hour post-induction to assess ZapN1 expression.

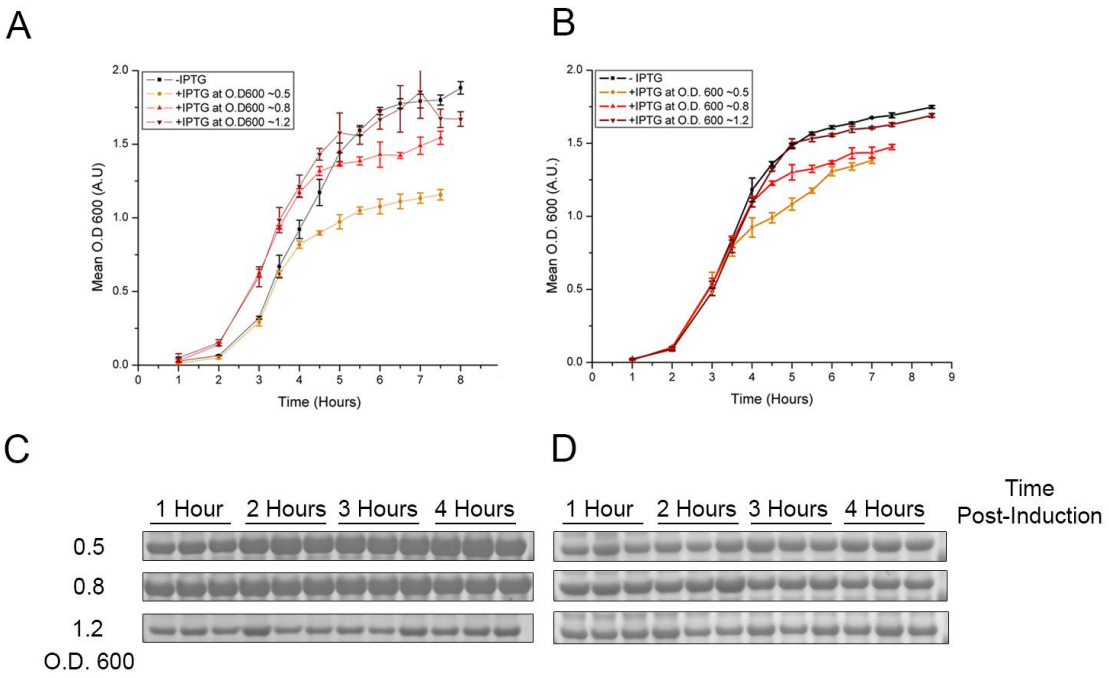

Figure 4.3.2 Induction of ZapN1 Expression at Various Time Points in BL21-Gold (DE3) Cultures. Growth curves of BL21-Gold (DE3) cells (100 ml cultures of TB media) expressing ZapN1 induced by 1 mM IPTG at various O.D. $_{600}$ values (0.5, 0.8, and 1.2). As a control, cultures were incubated without the addition of IPTG to monitor any effect on cell growth after IPTG addition (A). Growth curves of BL21-Gold (DE3) cells (100 ml cultures of TB media) that were double-screened for ZapN1 expression. ZapN1 expression was induced at the same O.D. $_{600}$ values as in A and bacterial growth was also monitored in cultures were no IPTG was added (B). The data points correspond to the mean O.D. $_{600}$ values from 3 cultures and the error bars correspond to the standard deviations of each mean. Coomassie Brilliant blue-stained polyacrylamide gels showing the expression of ZapN1 over time from BL21-Gold (DE3) cultures (no screening) induced at various O.D. $_{600}$ values (C). Coomassie Brilliant blue-stained polyacrylamide gels showing the expression of ZapN1 over time from double-screened BL21-Gold (DE3) cultures induced at the same O.D. $_{600}$ values as in C (D).

We optimized induction time for single and double-screened colonies and monitored ZapN1 expression every hour after induction. We observed that induction at $O.D._{600}$ 0.5 reduced bacterial growth when compared to bacterial cultures induced when the value $O.D._{600}$ was 0.8 or 1.2. However, we observed no difference in ZapN1 expression over 4 hours between cultures induced at either $O.D._{600}$ 0.5 or 0.8. In contrast, bacterial cultures induced at $O.D._{600}$ 1.2 showed severe ZapN1 expression reduction in comparison to the cultures induced at either $O.D._{600}$ 0.5 or 0.8. We observed the same trend n ZapN1 expression for the single screened colony. We did not observe any differences in bacterial growth between the single and double-screened cultures indicating that the higher ZapN1 expression in the double-screened colony is not due to higher bacterial growth. For subsequent expression experiments, we chose induction at $O.D._{600}$ 0.8 and 3 hours incubation.

4.3.3 Temperature Effects on ZapN1 Expression

Bacterial cultures can be incubated at different temperatures post-induction, which affects protein expression. We proceeded to determine ZapN1 expression at 16, 23, 30, and 37 °C in small-scale LB cultures. ZapN1 expression was induced with 1 mM IPTG at $O.D._{600}$ 0.8 and cultures were incubated for 3 hours at the 4 temperatures mentioned previously. 1 ml samples were taken every hour to assess ZapN1 expression by SDS-PAGE analysis. Figure 4.3.3 shows the Coomassie blue stained SDS-PAGE gel for single and double screened bacterial cultures incubated at different temperatures and assessed every hour post-induction.

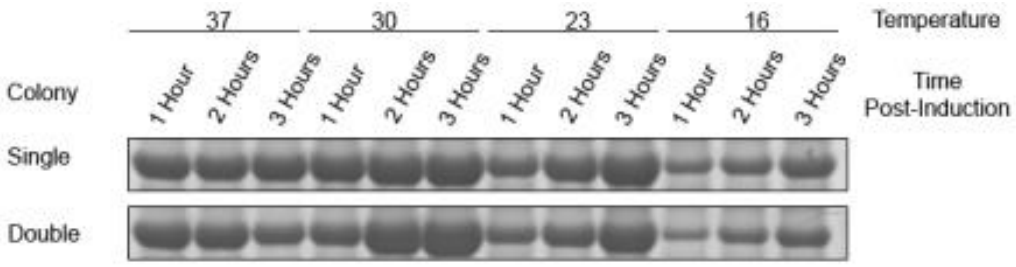

Figure 4.3.3 Temperature Effects on ZapN1 Expression on Single and Double-Screened Colonies. Coomassie Brilliant Blue-stained polyacrylamide gel showing expression of ZapN1 from BL21-Gold (DE3) cultures (single vs. double expressed) at various time points. Cultures were subjected to different temperatures (37, 30, 23, and 16 °C) following addition of IPTG for 3 hours each. Each hour after induction, 1 ml samples were taken for SDS-PAGE analysis. Expression of ZapN1 was highest when induction was carried out at 30 °C (in both single and double-screened samples) but higher in the double-screened samples than the single-screened cultures after 3 hours incubation.

As expected, ZapN1 expression in the double-screened cultures was higher than in the single screened cultures. ZapN1 expression was the highest in both single and double-screened cultures at 30 °C. Surprisingly, ZapN1 expression was lower when cultures

were incubated at 37 °C than either 30 or 23 °C. ZapN1 expression was the lowest when cultures where incubated at 16 °C. For all cases, ZapN1 expression was highest when incubated for 3 hours. Based from these results, ZapN1 expression for future expression experiment will be conducted at 30 °C for 3 hours.

4.3.4 Batch Purification of ZapN1 from Single and Double Screened Cultures

We proceeded to test ZapN1 purification using a batch method to simplify the purification from previous FPLC methods using a novel Nickel affinity resin. We employed the His60 Superflow nickel resin for its high binding capacity and claimed higher purity obtained. ZapN1 was expressed in 100 ml TB cultures of single or double-screened BL21 (DE3) cells. ZapN1 expression was induced with 1 mM IPTG at $O.D._{600}$ 0.8 and cultures were incubated 3 hours at 30 °C. Cultures were pelleted and processed as described in the methods for Nickel affinity purification. To assess the nickel affinity purification, samples from the cell lysate, wash, and elution fractions were analyzed by SDS-PAGE. Figure 4.3.4 shows the Coomassie stained SDS-PAGE gels for single and double screened cultures expressing ZapN1 and the different nickel affinity purification fractions.

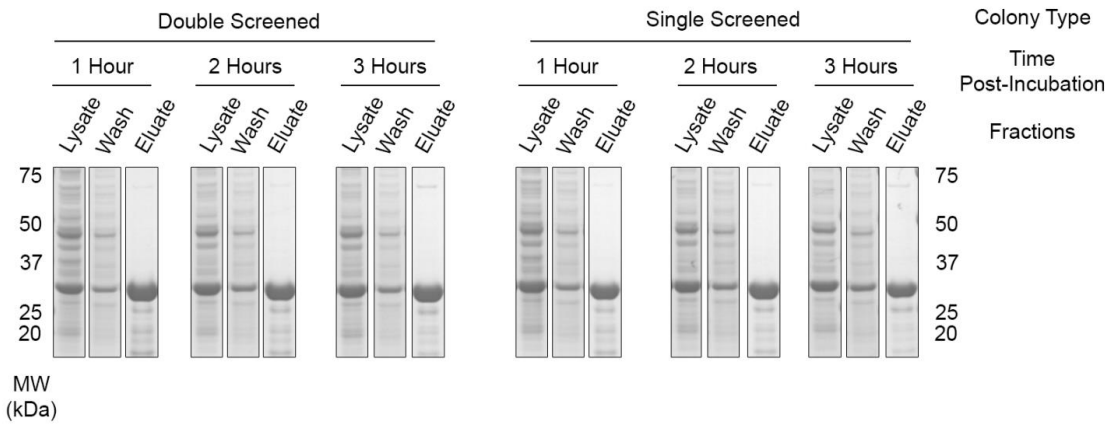

Figure 4.3.4 Purification of ZapN1 from cell cultures harvested at various time points. ZapN1 expression in single and double-screened samples was analyzed by purifying the protein from total cell pellets (100 ml). Cell pellets were collected from samples at various time points and processed equally to look for any differences in protein yield. ZapN1 was purified using the His60 Ni superflow resin each step assessed by SDS-PAGE analysis. The figure above shows the Coomassie Brilliant Blue stained gels of each flowthrough (lysate, wash, and eluate) from each sample.

ZapN1 purification using the His60 superflow resin yielded ZapN1 with very little co-contaminants eluting in the imidazole gradient. We observed no differences in the time point at which cultures were harvested and between the single and double screened cultures. We also observed that most bacterial proteins observed in the cell lysate are washed away during the purification method. We do observe a small amount of ZapN1 that elutes in the wash fraction but the amount is minimal compared to the ZapN1 present in the elution fractions. The batch procedure took only a few hours to complete and yield highly pure ZapN1. In contrast, FPLC based ZapN1 purification takes on average 1 day or longer which adds considerable time to the purification method. Based on these

results, we proceeded to perform a large-scale ZapN1 expression using the previously optimized expression and purification methods.

4.3.5 Large-Scale Expression of ZapN1

We expressed ZapN1 using the double screened BL21(DE3) culture in 8 L TB media using the previously optimized expression and purification parameters. ZapN1 was collected over 5 fractions from the nickel affinity resin and each fraction was analyzed by SDS-PAGE to determine ZapN1 purity. ZapN1 yield was determined by measuring the 280 nm absorbance from the pooled elution fractions. Figure 4.3.5 shows the Coomassie blue stained SDS-PAGE gel for fractions 1 – 5 from the nickel resin. Figure 4.3.5 also shows the combine fractions diluted 100x for clarity.

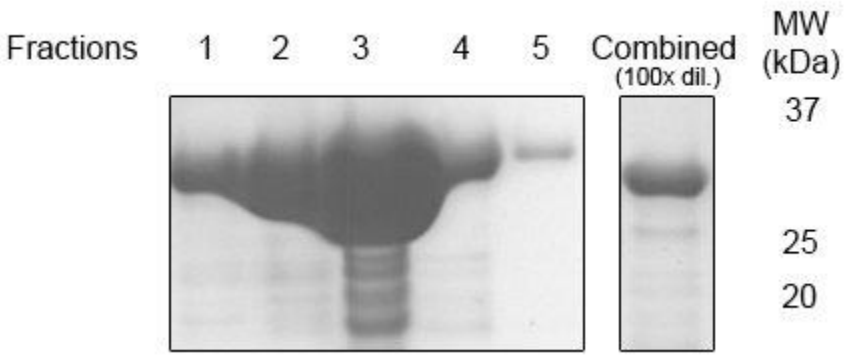

Figure 4.3.5 Large-scale purification of ZapN1. Coomassie Brilliant Blue stained polyacrylamide gel with fractions obtained from the His60 purification of ZapN1. The right panel shows the combined fractions (1- 4) that have been diluted 100x in the same buffer without imidazole. ZapN1 was mainly contained in fractions 2-3 with very little proteolysis products found in the fractions. The total yield of ZapN1 from the 8 L culture was 1.8 grams.

ZapN1 elutes primarily in fractions 2 and 3 with some protein eluting in fractions 1 and 5. We only observed lower molecular weight contaminants in fraction 3. From the combine fraction, we observe that the contaminants, which we believe are ZapN1 truncations, are negligible relative to the concentration of ZapN1. We purified ~250 mg/L culture of ZapN1 which is a massive improvement from the previous method which yielded in average 10 mg/L culture. Given this, we have successfully purified ZapN1 in high purity and yield from BL21 (DE3) cells.

4.3.6 Construction of High Throughput Chromatography Platforms

Initial NABB assembly experiments with ZapN1 revealed several limitations in the set-up employed to remove detergent and collect NABB fractions. We found that the old set-up did not allow for temperature control and only up to 4 purifications could be performed simultaneously. To address this problem, we designed and constructed with aid of the Rockefeller Precision Facility two platforms made from Acrylic (for RT purifications), and M3 crystal (for 0°C purifications) for high-throughput, minis-scale chromatography. Figure 4.3.6 shows photographs of the assembled platforms viewed from different angles. We designed the 96 samples holder in Acrylic to be compatible for RT purifications. For the 24 samples holder, we designed the top with a reservoir surrounding the individual column holders where ice-water mixture will be placed to cool down the samples. Both platforms are compatible with the walls of the box so that they can be freely interchanged. We have employed both platforms in NABBs assembly using

manual or automated Elutions using the EpMotion 5070. Samples are collected in a 96 well plate underneath the platforms in 4 steps. The platforms are compatible with any batch chromatography method, which allow for faster purification optimization.

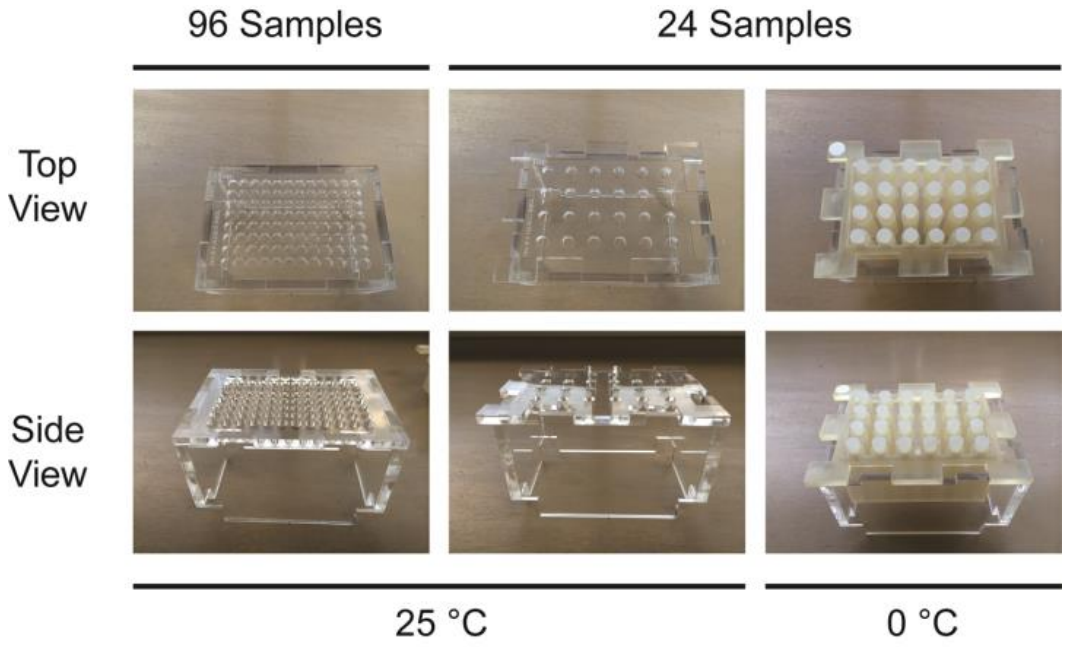

Figure 4.3.6 Photographs showing the HTCPs built at the Rockefeller Precision Fabrication Facility. The top panels show the top view for the three different adapters designed. The lower panels show each adapter in conjunction with the HTCP. The adapters have been designed to hold 96 samples or 24 samples at either RT or at 0 °C.

4.3.7 Assembly of NABBs with POPC

We assembled NABBs using the phospholipid POPC at a stoichiometry ratio of 75 or 55 POPC per 1 ZapN1. Previous NABBs assemblies with Rho and CCR5 employed POPC for receptor reconstitution. Thus, we assembled NABBs using ZapN1 and POPC and

characterized the complexes by SEC and Native PAGE. Figure 4.3.7 shows the 280 nm absorbance chromatographs for POPC NABBs assembled at either 75 or 55 lipids per ZapN1. Figure 4.3.7 also shows the Coomassie blue stained Native PAGE for the two NABB assemblies.

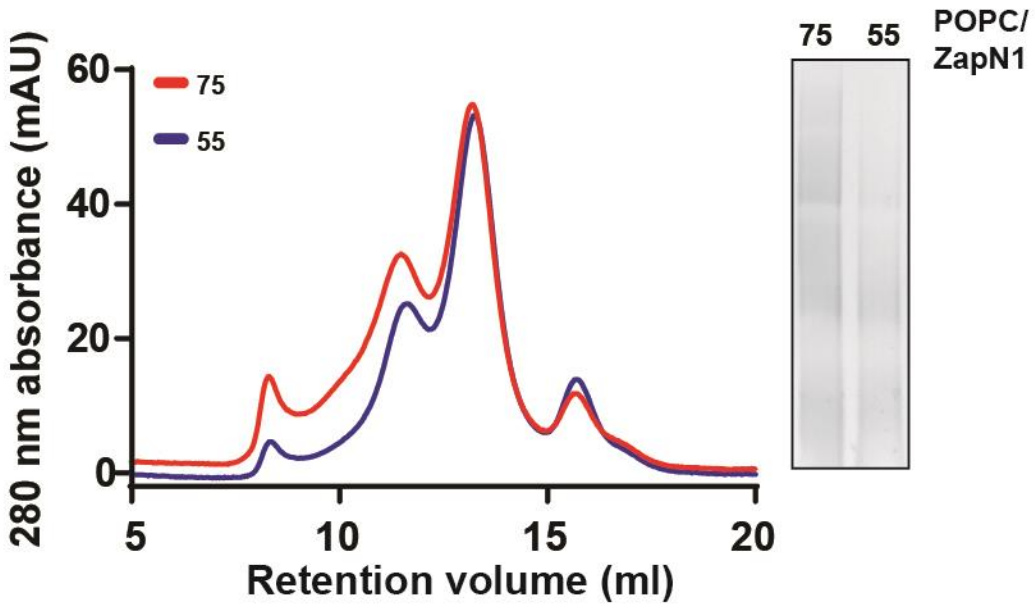

Figure 4.3.7 Size-exclusion chromatographs of NABBs assembled with 75 or 55 POPC lipids per ZapN1. The chromatographs show that the NABBs elute as two distinct peaks corresponding to NABBs of 16 and 11 nm in diameter. The SEC data also shows two other peaks, which correspond to vesicles and free-ZapN1. The inset shows the same samples analyzed by native gel stained in Coomassie blue.

The SEC chromatographs shows that POPC NABBs are highly heterogeneous since we observed 4 distinct species at either 75 or 55 lipids. The peak eluting at 8 ml corresponds to NABBs aggregates that form during the detergent removal procedure. The peaks eluting at 11.5 and 13.5 ml correspond to NABBs of different diameter. We calculated

the size of the assemblies and determined that the NABBs are 16 and 11 nm in diameter. The 4th peak eluting at 16 ml corresponds to either NABBs that are lipid deficient of free ZapN1. The Native page shows similar heterogeneity since the NABBs run as a smear with one singe defined band. Based on these results, we proceeded to find a suitable lipid for NABB assembly that yielded more homogeneous preparations than POPC.

4.3.8 Assembly of NABBs with Various Lipids

We assembled NABBs using various saturated and unsaturated lipids at 75 lipids per ZapN1. We tested SOPC which is like POPC but it is two carbons longer in the alkyl chains and has a transition temperature closer to 0 °C. We also tested the saturated lipids DLPC, DMPC, and DPPC, which differ only in the length of the alkyl chain. NABBs were assembled as described before using identical conditions. NABBs were analyzed by SEC and Native-PAGE. Figure 4.3.8 shows the 280 nm absorbance chromatographs for NABBs assembled with the lipids tested and the Coomassie Blue stained Native PAGE gel.

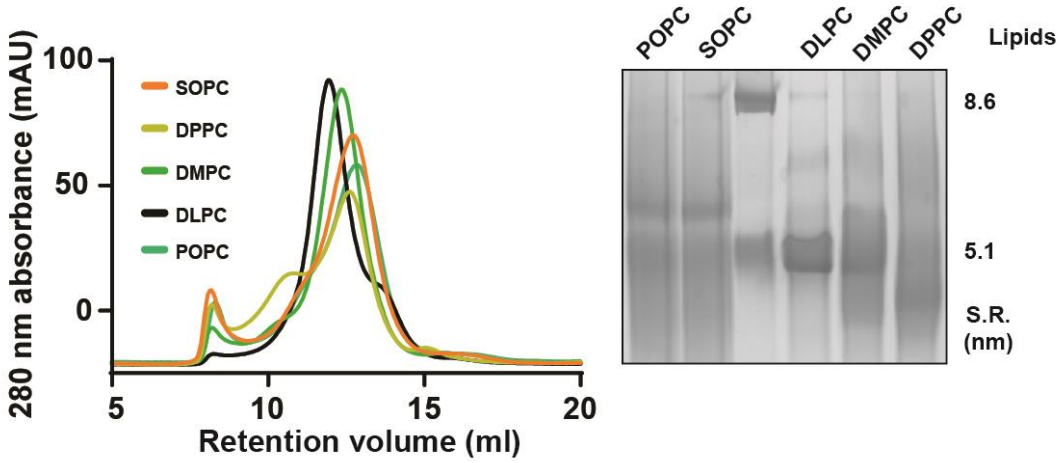

Figure 4.3.8 Chromatographs obtained for ZapN1 NABBs assembled with different lipids at 0 °C and 75 lipids per ZapN1. DLPC NABBs show the greater degree of homogeneity than any other lipid tested. The inset shows the Coomassie Blue stained native gel.

The SEC results show DLPC yields the most homogeneous preparations from the all the lipids tested. All the lipids tested from NABBs of approximate diameter 10 – 11 nm with varying degrees of larger NABBs and aggregates present in the sample. DMPC NABBs are also more homogeneous than the other lipids tested but this lipid has a transition temperature of 24 °C which is not compatible for GPCR reconstitution. DPPC proved difficult to solubilize in aqueous solutions due to its longer alkyl chain and yielded heterogeneous preparations. Native PAGE shows no difference between POPC and SOPC indicating that their difference transition temperature has no effect on NABBs homogeneity. DLPC NABBs run as a single major band while DMPC and DPPC show increasing degree of heterogeneity probably because of increasing alkyl chain length. We also ran the proteins thyroglobulin and catalase for which Stokes' radii are known. Except for DPPC, the NABBs assembled with the other lipids run similarly as catalase indicating that they must also have a Stokes radius close to 5 nm. Based from these results, we proceeded to optimize assembly of DLPC NABBs using varying lipid/ZapN1 ratios.

4.3.9 Assembly of DLPC NABBs With Different Lipid to ZapN1 Ratios

POPC NABBs are assembled at 75 lipids per ZapN1 based on previous optimization performed by Banerjee (2008). We discovered that DLPC yields near-homogeneous preparations by SEC and Native PAGE. Given this, we optimized the lipid to ZapN1 ratio for the DLPC NABBs. We assembled NABBs at 65, 75, 85, and 95 lipids per ZapN1 using identical conditions as described in the methods section. DLPC NABBs were analyzed by SEC and Native PAGE to determine the homogeneity of the preparations. Figure 4.3.9 shows the 280 nm absorbance chromatographs for the DLPC NABBs assembled with varying lipid to ZapN1 ratios and the Coomassie Blue stained Native PAGE gel.

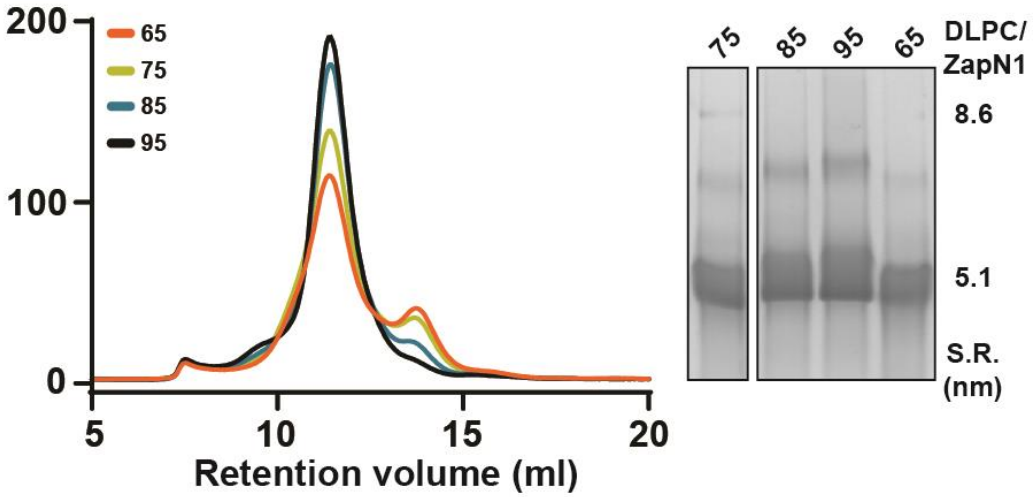

Figure 4.3.9 NABBs assembled at various DLPC to ZapN1 ratios. The size exclusion chromatographs shows that the DLPC NABBs assembled at 95 DLPC/ZapN1 are homogeneous to other stoichiometries tested. The inset show the native gel obtained for the NABBs tested.

SEC chromatographs shows that DLPC NABBs assembled at 95 lipids per ZapN1 are the most homogeneous compared to other stoichiometric ratios tested. For all cases, we observed one prominent peak eluting at 11.5 ml, which corresponds to NABB particles of 10 – 11 nm in diameter. We observed small amounts of aggregate, larger NABBs, and free ZapN1 in the preparations. As the amount of lipid per ZapN1 decreases, we observed that the peak corresponding to free ZapN1 increases. Native PAGE analysis showed that the DLPC NABBs assembled run at the same molecular size as a single sharp band. Given this, we chose the optimal DLPC to ZapN1 ratio to be 95 lipids per ZapN1.

4.3.10 Assembly of DLPC NABBs with GPCR Solubilization Agents

CCR5-SNAP is purified in a detergent mixture comprising of DDM, CHAPS, CHS, and glycerol, which may affect the assembly of DLPC NABBs. We have routinely employed CHAPS in the assembly of NABBs and we have not observed any detrimental effect if sodium cholate is present. Sodium cholate at a concentration of 2% (w/v) is required to yield near-homogeneous preparations. Yet, We have not tested addition of DDM, CHS, or glycerol to the NABB assembly reaction. We assembled DLPC NABBs at a ratio of 95 lipids per ZapN1 with 5% glycerol, 0.15% DDM, 0.15% DDM + 0.015% CHS, and 0.15% DDM + 0.015% CHS + 5% glycerol. NABBs were analyzed by SEC and Native PAGE as described before. Figure 4.3.10 shows the 280 nm absorbance chromatograph for the DLPC NABBs and the Coomassie Blue stained Native PAGE gel.

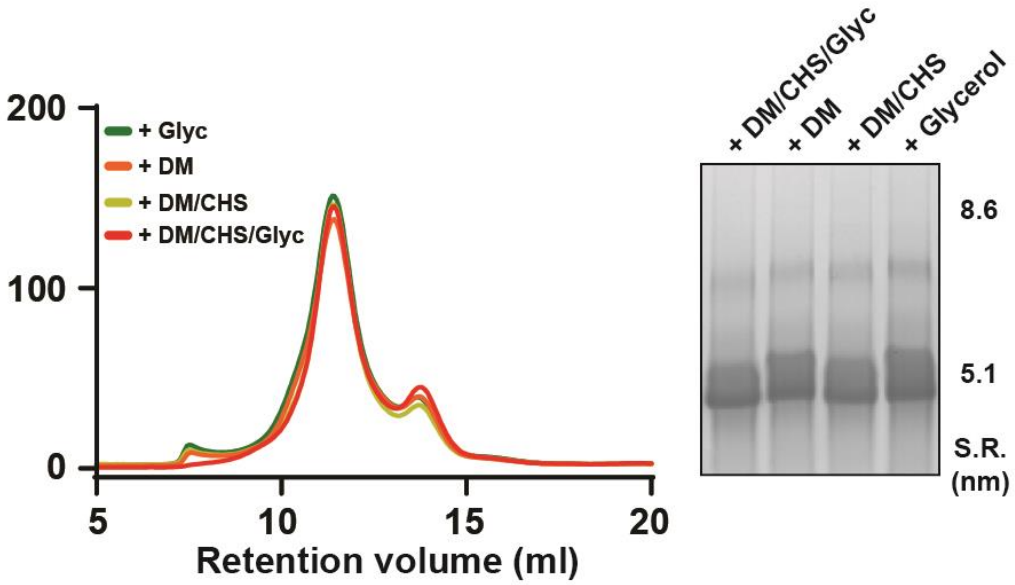

Figure 4.3.10 Size exclusion chromatographs for DLPC NABBs assembled with different GPCR solubilization reagents. NABB elution was monitored by 280 nm absorbance from ZapN1. Inset shows the Coomassie Blue stained Native-PAGE gel with the different NABB samples tested. Thyroglobulin and catalase are added in a separate lane as molecular size standards.

SEC chromatographs show DLPC NABBs are not affected by the addition of DDM, CHS, or glycerol. Likewise, we observed no differences on the assemblies by Native PAGE indicating that DLPC NABBs are robust to the addition of detergents and glycerol. Based from these results, we proceeded to characterize DLPC NABBs by negative stain electron microscopy (EM) and atomic force microscopy (AFM).

4.3.11 Characterization of DLPC NABBs by Negative Stain EM

DLPC NABBs are near homogeneous by SEC and Native-PAGE but it is unclear if they form discoidal particles. To characterize NABBs morphology, we imaged negative stained NABBs on copper grid using transmission electron microscopy. Empty NABBs and CCR5-SNAP NABBs were stained in 1% uranyl acetate solution and imaged as described in the materials and methods section. Figure 4.3.11 shows two representative images from NABBs and CCR5-SNAP NABBs obtained in the JEOL 1400 Plus electron microscope with beam energy set at 120 kV and 25,000x magnification.

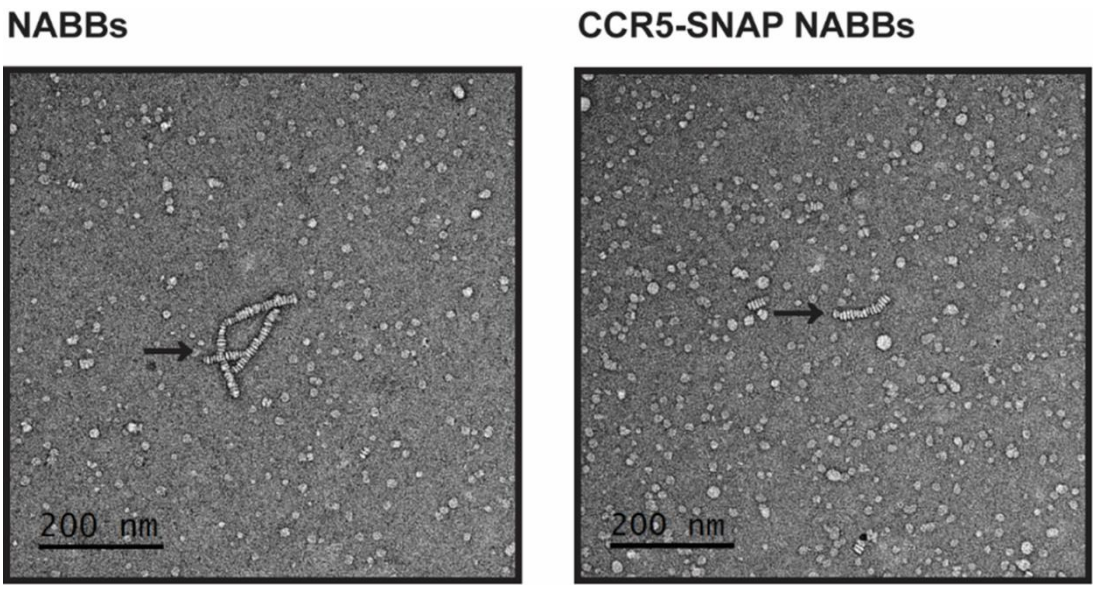

Figure 4.3.11 Negative stained electron microscopy images obtained for empty NABBs and CCR5-SNAP NABBs loaded onto carbon coated copper grids and stained with 1% uranyl acetate. Images were acquired using an electron beam energy of 120 kV and 25,000x magnification. Arrows point to Rouleaux formation indicative of HDL particle formation.

Rouleaux formation, the stacking of discoidal particles into rows, is observed in both the empty and CCR5-SNAP NABBs samples. We observed discoidal particles of varying sizes in the peak fractions indicating that the NABBs are heterogeneous in diameter. We also observed NABB aggregates that result from the fusion of Rouleax formations into a single highly branched species (data not shown). NABB dilution also affected NABB stability since SUVs were also present in the peak fraction. We cannot rule out that the heterogeneity observed is a result from NABBs interacting with the copper grid and affecting NABB morphology. Given this, we proceeded to image the NABBs in solution using AFM and derive quantitative information about NABB diameter and height distribution.

4.3.12 Characterization of DLPC NABBs by AFM

Negative stain EM images on empty NABBs and CCR5-SNAP NABBs revealed high degree of heterogeneity in the SEC peak fraction. We attribute the observed NABB heterogeneity to sample dilution, which precipitates NABB fusion to form SUVs. We also hypothesize that the NABBs are not interacting with homogenously with the copper surface, which contributes to the non-uniform NABB distribution and morphology. Given this, we imaged empty and SNAP-CCR5 NABBs using AFM. Pilot experiments revealed that NABBs imaged on air deflated and lost structural stability on the mica surface requiring the need for AFM imaging in fluid. NABBs were imaged in either Buffer G or Buffer C using a Cypher ES AFM with a silicon probe. Figure 4.3.12 shows

representative AFM images for SNAP-CCR5 and empty NABBs. Figure 4.3.12 also shows histograms for NABBs diameter and height.

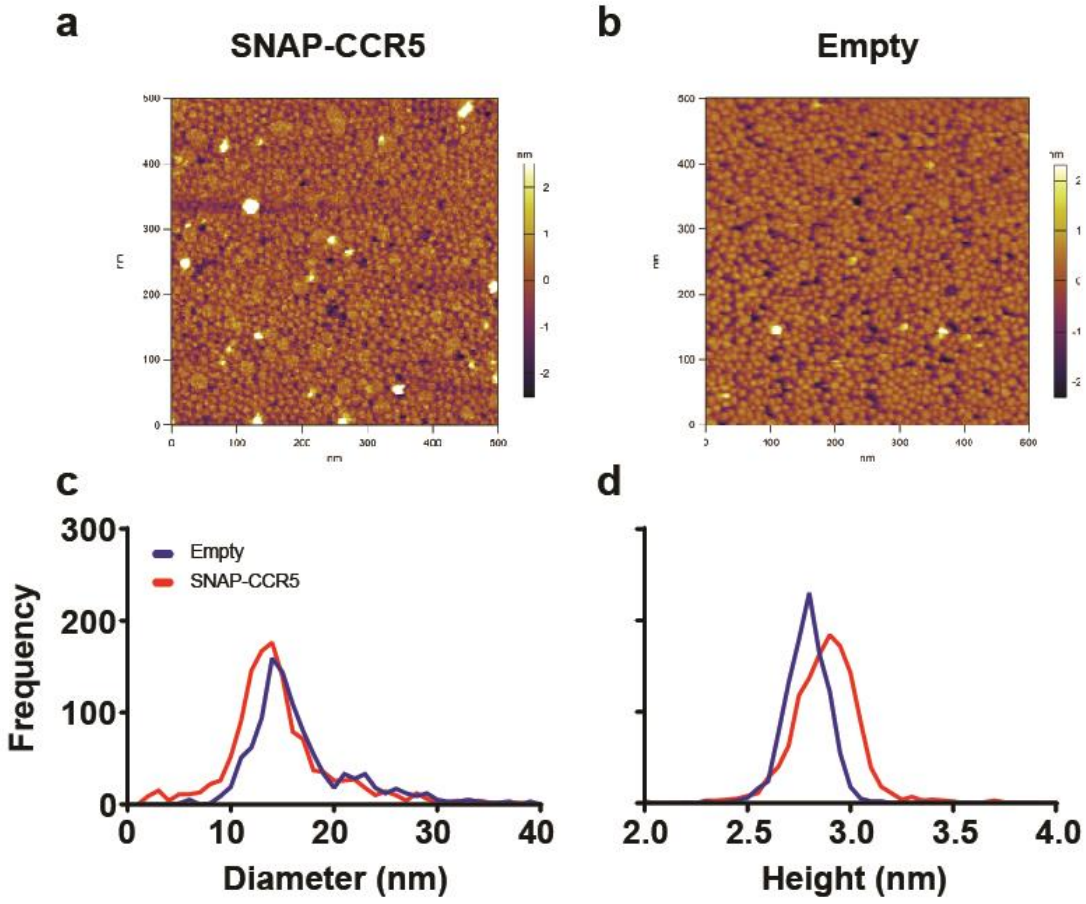

Figure 4.2.13 AFM imaging and analysis of SEC fractions containing empty and SNAP-CCR5 NABBs made with DLPC. a) AFM image for SNAP-CCR5 and b) for empty NABBs. xy Coordinates are in nanometers and the color scheme reflect the height of the sample in nanometers. c) NABBs diameter histogram and d) height histogram derived for SNAP-CCR5 and empty NABBs.

AFM images show that the NABBs are uniformly distributed on the mica surface with no Rouleaux formation present. We observe a small number of bright spots, which we attribute to NABB particle freely diffusing in solution. We also observe large NABBs, which are more prevalent in the SNAP-CCR5 NABBs than the empty NABBs. The larger discoidal structures have the same color as the NABBs indicating that they are the same height. Based from this, we attribute these larger particles to be NABBs of larger diameter. We observe that the NABBs are densely packed on the mica surface. The higher NABB density helps to prevent dilution induced NABB fusion. We calculated height and diameter for individual NABB particles and derived histogram distributions for both parameters. Table 4.3.12 shows the mean height and diameter calculated for SNAP-CCR5 and empty NABBs.

Table 4.3.12 Average height and diameter for SNAP-CCR5 and empty NABBs derived from AFM images. Errors are the standard deviation.

	Height (nm)	Diameter (nm)
SNAP-CCR5 NABBs	2.8 ± 0.2	14 ± 5
Empty NABBs	2.8 ± 0.1	16 ± 5

We observe no difference in particle diameter between the SNAP-CCR5 and empty NABBs. We also do not observe any statistically significant difference between the height of SNAP-CCR5 NABBs and empty NABBs. The calculated diameters from AFM images agree with the calculated values from SEC and Native-PAGE experiments.

4.3.13 Assembly and Characterization of Rho-Fl NABBs

We incorporated the prototypical GPCR, Rhodopsin, into DLPC NABBs and characterized the assemblies by SEC and FCS. We obtained Rhodopsin from bovine rod outer segments that were previously reconstituted with 11-*cis* retinal. We purified Rhodopsin from bovine ROS using DDM and labeled Rhodopsin with the fluorophore Fluorescein-maleimide that forms a covalent bond with solvent accessible cysteine residues. We labeled Rhodopsin with Fluorescein so we could monitor Rhodopsin by SEC and FCS. After Rho-Fl purification, we performed UV-Vis measurements on the 1D4 elution to determine the yield and the labeling stoichiometry. Fluorescein has a maximum absorption at 500 nm so we used the 380 nm absorbance from the dark-light spectrum of Rhodopsin to measure the amount of recovered Rhodopsin. We measured an absorbance of 0.019494 at 380 nm and calculated rhodopsin concentration to be 0.1834 mg/ml using an extinction coefficient of 36,143 and dilution factor of 10. To determine the concentration of Fluorescein, we determined an absorbance of 0.088203 at 500 nm in the light spectrum of Rhodopsin. From this value, we calculated a concentration of 11.47 μM using an extinction coefficient of 76,900 and a dilution factor of 10. We determined the labeling stoichiometry to be 2.2 Fluorescein per Rhodopsin. We employed this labeled protein for reconstitution into DLPC NABBs. Rho-Fl NABBs were loaded into a previously equilibrated Superdex 200 10/300 column and NABBs elution were monitored by absorbance at 280 and 494 nm. Figure 4.3.13a shows the SEC chromatograph obtained by monitoring sample absorbance at 280 and 494 nm.

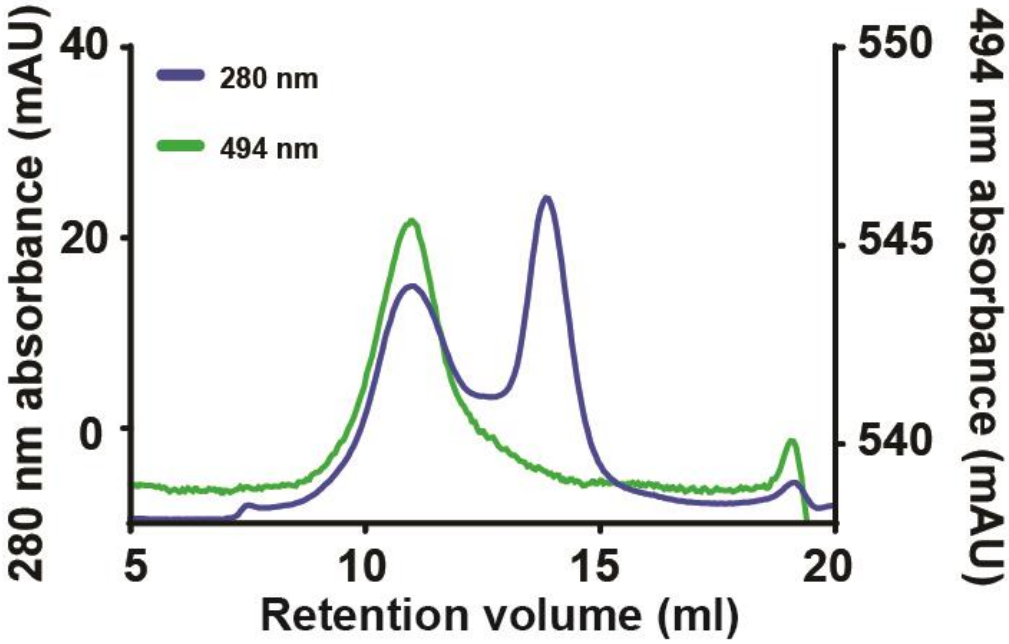

Figure 4.3.13a Rho-Fl NABBs eluting from Superdex 200 10/300 GL column in Buffer G. Fluorescein absorbance was monitored at 494 nm and protein absorbance at 280 nm.

The SEC chromatographs show two distinct peaks in the 280 nm absorbance elution profile. In the other hand, we observe only one peak in the 494 nm absorbance elution profile from the Rho-FL. This second peaks elutes at ~ 10.5 ml and aligns with one peak observed in the 280 nm absorbance profile. We attribute this peak to be the Rho-Fl NABBs since calculating the Stokes' radius for this species yields a value of (6.1 ± 0.6) nm. We did not further characterize the second peak which elutes at ~13 ml but we attribute this peak to be empty NABBs. We also characterized the Rho-Fl NABBs by FCS as described in the methods section. Figure 4.3.13b shows the auto-correlation trace and associated fit for Rho-Fl NABBs.

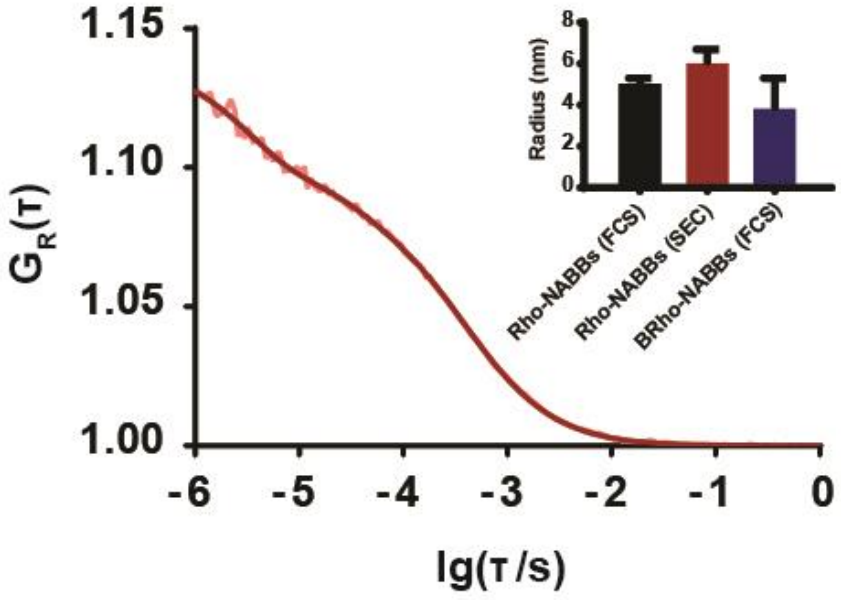

Figure 4.3.13b FCS traces obtained for Rho-Fl NABBs. Autocorrelation was fitted to a 1 component with 3-D translational and dependent rotational diffusion and triplet state fluctuations. The inset in the left panel shows the calculated Stokes radii for Rho-FL NABBs from the FCS and SEC data. For comparison, The Stokes radius bacteriorhodopsin incorporated into nanodiscs is shown in the bar graph.

FCS curves were fitted using a 1 3D translational component with dependent rotational diffusion and independent triplet state transitions. We calculated a (25 ± 1) % triple state fraction with a relaxation time of (3.1 ± 0.4) μs for Rho-Fl NABBs. We also calculated a rotational relaxation time of (27 ± 5) μs and a translational diffusion time of (380 ± 7) μs. Using the calculated confocal volume for 488 nm excitation, we calculated a concentration of (29.8 ± 0.3) nM for Rho-Fl NABBs. Lastly, we employed the translational diffusion time and derived a Stokes radius of (5.1 ± 0.2) nm, which is not that different from the SEC derived value of (6.1 ± 0.6) nm. For comparison,

bacteriorhodopsin incorporated into DMPC nanodiscs had a Stokes radius of (3.9 ± 1.4) nm.[111]

4.3.14 Characterization of CCR5-SNAP NABBs

After successfully incorporating Rhodopsin into DLPC NABBs, we proceeded to incorporate CCR5-SNAP-488 into NABBs and characterize the assemblies by SEC. Since CCR5-SNAP-488 concentration is too low for detection by 280 or 496 nm absorption, we analyzed SEC fractions by SDS-PAGE to detect CCR5. We employed 1D4/FLAG purified CCR5-SNAP-488 for NABB assembly with DLPC. Figure 4.3.14a shows the SEC chromatograph from 280 nm absorption. Figure 4.3.14a also shows the western immunoblot of SEC fractions 20 – 24 where CCR5 was detected using the 1D4 epitope. The SEC chromatographs shows 4 distinct peaks and a shoulder around the main peak. The peak at 7 ml corresponds to NABB aggregates eluting in the void volume. The main peak at 12 ml corresponds to the NABB particles and the shoulder centered on 10 ml represents NABBs of larger diameter than 11 nm. The peak at 14 ml corresponds to free ZapN1 or lipid deficient ZapN1. The peak at 18 ml corresponds to the salt front from the sample.

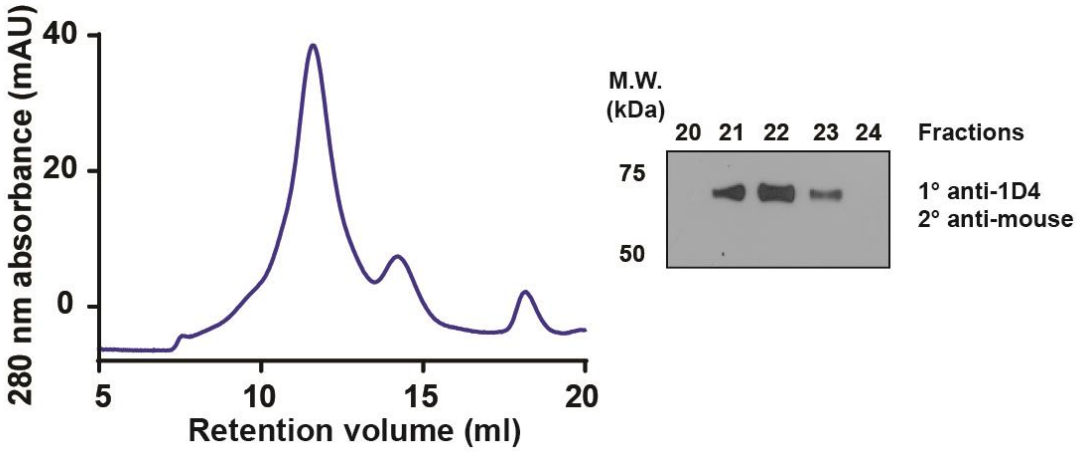

Figure 4.3.14a 280 nm absorbance chromatograph for CCR5-SNAP NABBs eluting in the Superdex 200 10/300 GL column. Inset shows the western immunoblot of SEC fractions 20 – 24. CCR5-SNAP was detected using the 1D4 monoclonal antibody.

To detect CCR5-SNAP in fractions 20 – 24, we performed SDS-PAGE analysis and western immunoblotting to determine the elution of CCR5-SNAP in the NABBs. CCR5-SNAP is present only in fractions 21 – 23. The results indicate that CCR5-SNAP successfully incorporated into DLPC NABBs. We performed saturation binding with the conformationally sensitive antibody 2D7 conjugated to Cy5, which is spectrally like Alexa-647. Figure 4.3.14b shows auto-correlation traces for CCR5-SNAP (a) 2D7-Cy5 (b) and cross-correlation traces obtained for the antibody-receptor complex (c) at the different antibody concentrations tested. Auto-correlation traces were fitted using 2 components with 3D translational diffusion and triplet state transitions. Cross-correlation traces were fitted using a single component with 3D diffusion.

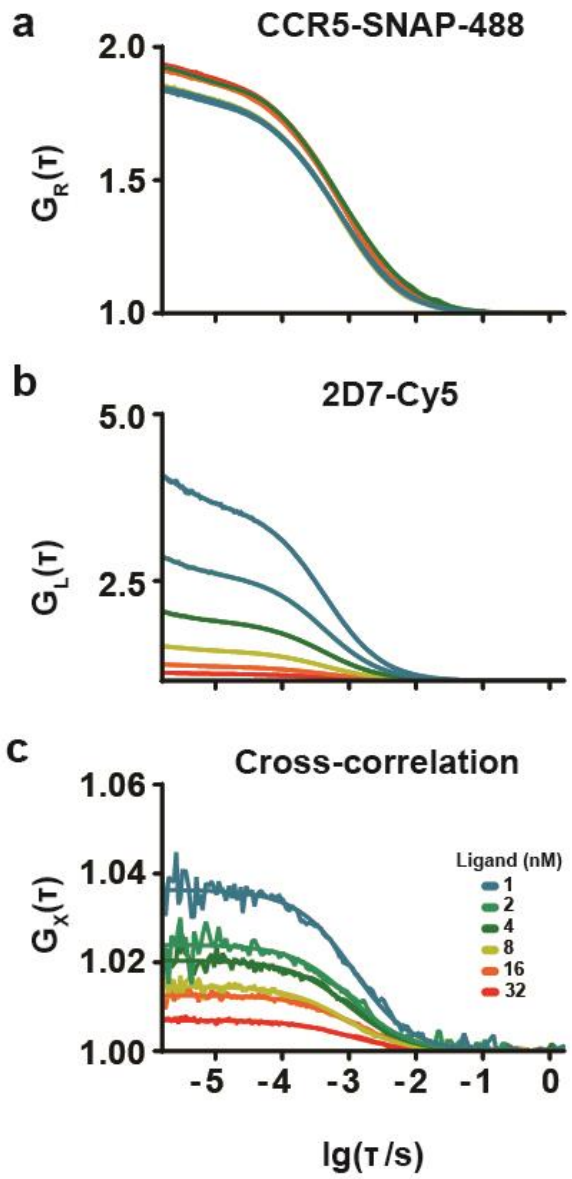

Figure 4.3.14b (a) CCR5-SNAP-488 auto-correlation traces and fits for different concentrations of 2D7-Cy5. (b) 2D7-Cy5 auto-correlation traces and fits for all concentrations tested. (c) Receptor-ligand complex cross-correlation traces and fits for different concentrations of 2D7-Cy5.

We calculated concentrations for each fluorescent component and derived the binding isotherm for 2D7-Cy5. Figure 4.3.14c shows the saturation-binding isotherm derived for 2D7-Cy5 by plotting RL/R as a function of free antibody.

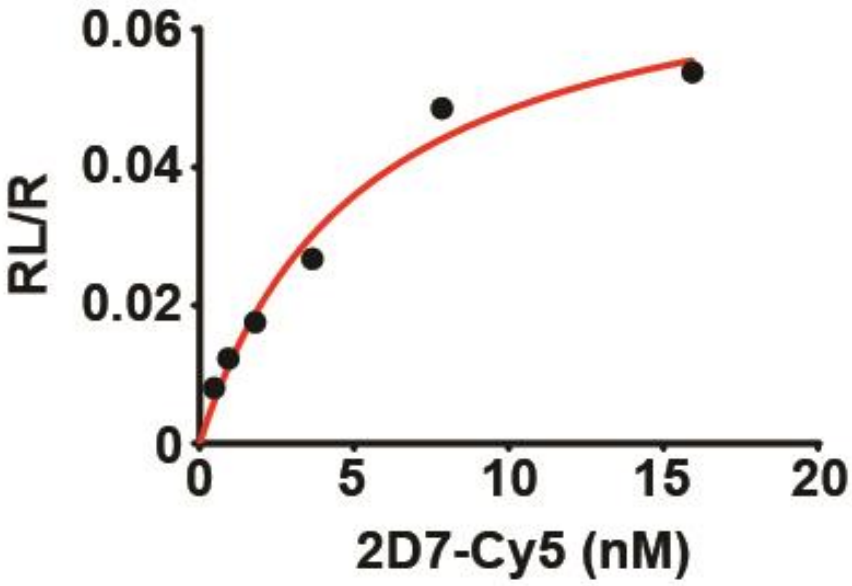

Figure 4.3.14c Saturation binding isotherms for 2D7-Cy5 binding to CCR5-SNAP-488 in DLPC NABBs. Data points represent individual points for different concentrations of labeled antibody. The red solid line represents the fit performed on the data points using equation 4.4.

We did not account for ligand depletion in this binding experiment since we did not observe any appreciable differences between the concentrations of total and free 2D7-Cy5. We calculated a K_D (5 ± 1) nM for 2D7-Cy5 which is similar to the value calculated in cell-based saturation assays of 4.5 nM.[112] We conclude that CCR5-SNAP reconstituted into DLPC NABBs is functional.

4.4 Discussion

4.4.1 Zapn1 Expression and Purification Optimization

We successfully expressed and purified *D. rerio* apolipoprotein AI (ZapN1) from *E*. coli in high yield and purity. From an 8 L culture, we purified 2 grams of ZapN1 using an optimized expression protocol and batch nickel affinity purification. In contrast, Zap1, the non-codon optimized gene, yielded ~ 50 mg total protein from a 13 L culture using the previously published protocol.[86] We assemble NABBs with a total of 1 mg ZapN1 per 150 µl reaction volume limiting the amount of NABB reactions that can performed. Our initial approach was to optimize the Zap1 codon usage to generate a construct that could be expressed in non-Rosetta 2 cell lines. Zap1 was expressed in BL21 (DE3) Rosetta 2 cells, which encode for 7 rare tRNAs to enhance eukaryotic protein expression. We generated ZapN1 in the pET28 plasmid backbone and transformed BL21 (DE3) cells to induce protein expression with IPTG. Pilot expression experiments using a Fermenter to achieve high cell density did not yield higher ZapN1 quantities than cell cultures grown in flasks (data not shown). Given this, we opted to optimize ZapN1 expression in bacterial cultures grown in flasks. Sivashanmugam (2009) discovered that double-selected *E*. coli colonies expressing truncated apolipoprotein E yielded higher protein expression than single selected colonies.[113] We replicated the double-selection protocol using ZapN1 transformed BL21 (DE3) cells and indeed we show that after two rounds of selection, ZapN1 expression increases. We also show that Zap1 and MSP1D1 express higher in double-selected colonies than single selected colonies.

We proceeded to optimize ZapN1 expression induction time by adding 1 mM IPTG at optical densities of 0.5, 0.8, and 1.2. We did not observe any difference in cell growth between the single and double-selected cultures. Thus, the higher ZapN1 expression observed in double-selected colonies cannot be a result of higher cell expression in the double-selected colonies. We also found that IPTG induction at $O.D_{600}$ 1.2 yielded very low ZapN1 expression relative to the cultures induced at 0.5 or 0.8. We postulate that the lower ZapN1 expression observed in these cultures is a result of nutrient depletion in the media. We also tested ZapN1 expression at various temperatures in both the single and double-selected colonies. ZapN1 expression was the highest when single and double-selected colonies were incubated for 3 hours at 30 °C. SDS-PAGE analysis of cultures lysed with guanidium hydrochloride shows that a fraction of ZapN1 precipitates as inclusion bodies (data not shown). Triton X-100 cannot solubilize ZapN1 in inclusion bodies and higher incubation temperatures precipitate ZapN1 aggregation. Given this, we postulate that ZapN1 aggregates less at 30 °C than at 37 °C and we observe higher expression because there is more soluble ZapN1.

For ZapN1 purification, we decided to employ a batch method over the traditional FPLC method because in the past FPLC ZapN1 purification was time consuming and protein loss was significant. We chose the His60 Superflow nickel resin (Clontech) because of its higher binding capacity, higher protein purity, and better compatibility with detergents such as sodium cholate than Ni-NTA resins. We performed small-scale purification using the His60 superflow resin and observed that the purification method is robust and yields highly pure ZapN1 from single and double-screened colonies. We proceeded to scale ZapN1 expression to 8 L using the previously optimized expression and purification

parameters. We purified 2 grams of ZapN1, which is an improvement from the previous protocol which yielded 50 mg of Zap1.

4.4.2 NABBs Lipid Optimization

NABBs assembled with POPC showed 4 different peaks by SEC indicating that the preparations were heterogeneous and not suitable for single molecule analysis. Given this, we assembled NABBs with different lipid compositions to determine which lipid yielded homogeneous preparations. Figure 4.4.2 shows the chemical structures of the different lipids tested and their phase transition temperatures from the ordered gel phase to the liquid crystalline phase.

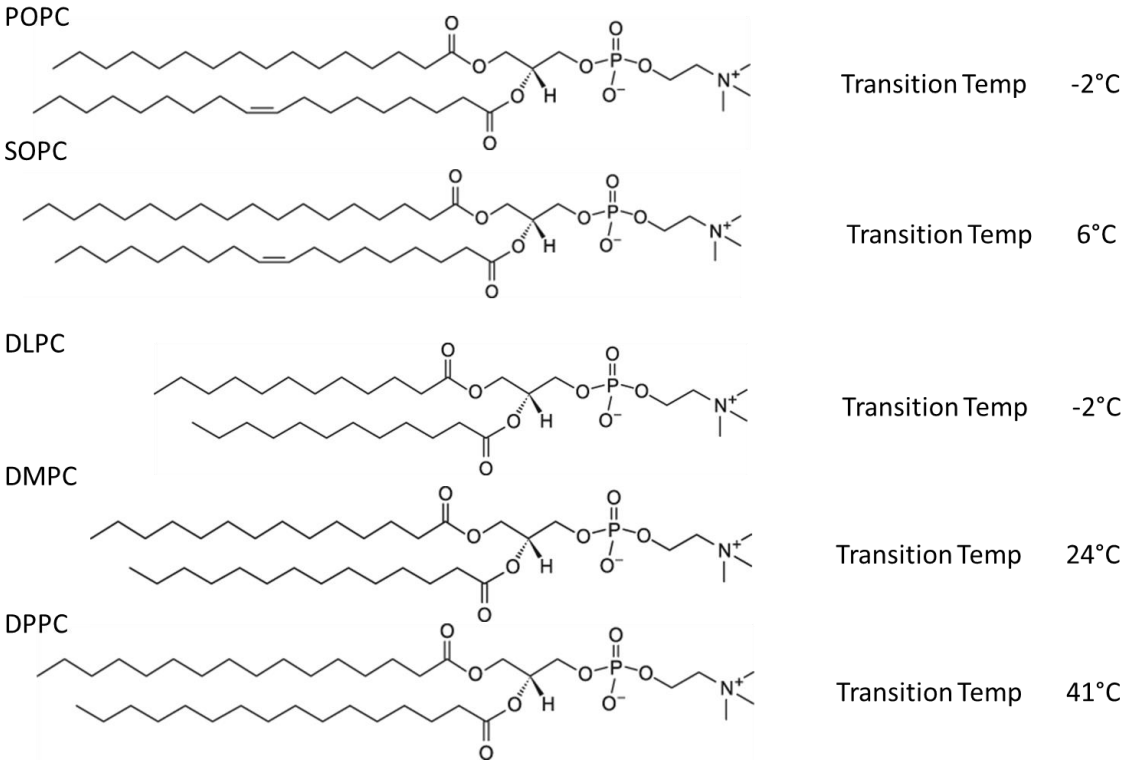

Figure 4.4.2 Chemical structure of the lipids employed to assemble NABBs and their phase transition temperatures.

We hypothesized that NABBs assembled with POPC were heterogeneous because reactions were incubated above the phase transition temperature of POPC. Given this, we chose SOPC as an alternative to POPC because it is chemically like POPC but the phase transition temperature is higher than POPC. Surprisingly, SOPC NABBs yielded similarly heterogeneous NABBs by SEC and identical band pattern by Native-PAGE. Thus, we rule out the possibility that POPC NABBs were heterogeneous because of the phase transition temperature being lower than the NABB assembly temperature. We tested 3 different saturated lipids to determine if NABBs made with these lipids yielded better preparations. DPPC has previously been employed with membrane scaffold proteins to generate homogeneous discs.[114, 115] We chose DLPC and DMPC since they are chemically like DPPC but with different alkyl chain lengths. SEC and Native-PAGE analysis show that DLPC NABBs are near-homogeneous and increasing alkyl chain length decreases sample homogeneity. Bavishi (2016) assembled discs using a lipid mixture of DLPC:DLPG:NBD-PE (73/25/2 mol %) and SEC analysis showed that the discs were near-homogeneous.[116] Similarly, Skar-Gislinge (2010) using small angle neutron scattering (SANS) and small angle x-ray scattering (SAXS) showed that the scattering data for DLPC discs was best fit using a monodisperse elliptical model.[117] We optimized the lipid per ZapN1 stoichiometry and discovered that NABBs assembled with 95 DLPC lipids per 1 ZapN1 yielded homogeneous preparations by SEC. In contrast, Skar-Gislinge (2010) calculated from SANS data that DLPC discs had a

stoichiometry of 76 lipids per 1 membrane scaffold protein. The difference in stoichiometry can be attributed to the fact that MSP is N-terminally truncated. Skar-Gislinge (2010) noted that the DLPC discs had a smaller circumference than the maximal circumference allowed if the MSP was fully extended in the discs. Given this, the MSP in the DLPC discs was not fully stretched and could potentially allow for higher lipid incorporation. We also tested the effect of adding DDM, CHS, and glycerol to DLPC NABBs to determine if they affected sample homogeneity. We did not observe any adverse effect from adding DDM, CHS, and glycerol to DLPC NABBs indicating that GPCRs solubilized in solutions containing those components are compatible with NABB assembly conditions.

We employed EM and AFM imaging of DLPC empty and CCR5-SNAP loaded NABBs to determine their morphology. EM imaging of DLPC NABBs showed that the NABBs were polydisperse and highly heterogeneous. In contrast, Mitra (2012) observed near-homogeneous nanodiscs loaded with the parathyroid hormone receptor 1 (PTH1R) as did Whorton (2007) for the β2AR in POPC nanodiscs [118, 119] Similarly, Choi (2013) were capable of reconstructing a three dimensional model of human integrin αIIbβ3 loaded into nanodiscs showing that they were able to obtain high quality preparations by EM.[120] Zhang (2011) showed that the Rouleaux formation observed for HDL particles is a staining artifact that results from electrostatic interactions between the stain and discs.[121] Stains such as phosphotungstic acid intercalate between discs holding two discs together through electrostatic interactions with the choline headgroup in the phospholipids. Guha (2008) discovered that NABB aggregation results from apolipoprotein dissociating from the bilayer disc.[122] Solvent exposure causes discs to

fuse together eventually forming vesicles to minimize phospholipid exposure to water. Thus, we postulate that NABB dilution contributes to NABB aggregation and interactions with the copper grid contributed to the polydispersity observed. Given this, we decided to image and characterize the NABBs by AFM.

We imaged empty and SNAP-CCR5 NABBs using an AFM microscope that allowed for imaging in fluids. In contrast to the EM images, empty NABBs by AFM were mostly homogeneous with little presence of larger aggregates or SUVs. SNAP-CCR5 NABBs were also mostly homogeneous but we did observe higher fraction of larger diameter NABBs. We did not observe any significant differences in the diameter and height of the empty and SNAP-CCR5 NABBs. Skar-Gislinge (2010) calculated for DLPC discs a bilayer thickness of 2.4 nm at 20 °C which is only 0.4 nm smaller than the thickness calculated from our AFM experiments. Skar-Gislinge (2010) deducted from their SANS and SAXS data that MSP determined disc bilayer thickness by minimizing hydrophobic mismatch between the membrane and protein.

4.4.3 GPCR Incorporation into DLPC NABBs

We incorporated Rhodopsin into DLPC NABBs and characterized the NABBs by SEC and FCS. Unlike CCR5-SNAP, we can obtain microgram quantities of Rhodopsin from bovine ROS which allow us to increase the ratio of receptor loaded NABBs to empty NABBs. Rhodopsin labeling with Fluorescein allow us to monitor Rhodopsin elution in SEC and observe the NABBs by FCS. SEC profile of Rho-Fl NABBs shows two peaks in the 280 nm absorbance and 1 peak in the 494 nm absorbance. Rho-FL NABBs elute at

10.5 ml while the empty NABBs elute at 13 ml. Choi (2013) observed a similar SEC profile for αIIbβ3 nanodiscs eluting in an Superdex 200 column indicating that the receptor loaded NABBs have a larger size than the empty NABBs. Bavishi (2016) also observed two different species for CYP709AI nanodiscs eluting from a Superdex 200 column. However, Bavishi (2016) did not characaterize the individual peaks since they did not have enough chromatographic resolution to obtain good separation. We calculated for the Rho-Fl NABBs a Stokes radius (6.1 ± 0.6) nm. Bayburt (2007) calculated a Stokes diameter of 12 nm for bovine Rhodopsin incorporated into POPC nanodiscs. Likewise, For the PTH1R nanodiscs, Mitra (2013) calculated a similar diameter of 12.5 nm. Mitra (2013) makes an excellent observation that the Stokes diameter assumes that the diffusing particles are spherical while nanodiscs are discoidal.

We also characterized Rho-Fl NABBs by FCS to determine the particles' Stokes radius. We fitted the auto-correlation traces using a functional form that account for rotational and translational diffusion and triplet state transitions. We included the rotational diffusion term based on Gao (2011) where they attributed the fast component to be due to rotational diffusion. Gao (2011) did not consider the possibility that the fast component they observed was due to triplet state transitions. Fitting the Rho-Fl NABBs with the rotational component did not alter the fitted triplet state parameters. We calculated a triplet state relaxation time of 4 μs and triplet fraction of 25%, which is what we observe for Alexa-488. Gao (2011) calculated a rotational diffusion time of 5 μs, which is too short to be due to rotational diffusion, and is most likely due to triplet state transitions. We calculated for Rho-Fl NABBs a rotational diffusion time of 27 μs which is too high to be triplet state transitions but too low to be from free dye diffusion. We cannot exclude

the possibility that the rotational component is due to blinking or other non-diffusional process. We calculated a translational diffusion time of (380 ± 7) μs for Rho-Fl NABBs. Gao (2011) calculated a translational diffusion time of (350 ± 10) μs for BRho nanodiscs. Ly (2014) calculated a higher diffusion time for the Lcrv bound YopB nanodiscs of 630 μs and derived a Stokes radius of 11.1 nm. We calculated a hydrodynamic radius of (5.1 ± 0.2) nm which is twice smaller than that determined by Ly (2014). We should note that the diffusion time measured is dependent on the size of the confocal volume. Thus, direct comparison between diffusion time is meaningful if FCS measurements were performed under identical conditions. On the other hand, we can compare Stokes radius derived from FCS measurements performed under different conditions since the diffusion coefficient is not depend on the size of the confocal volume. Differences in height and Stokes radii across different reports are due to differences in NABB assembly conditions, lipids employed, and apolipoprotein used to make NABBs. Nonetheless, we observe a general trend in height and Stokes radius for these particles across several reports.

We also incorporated CCR5-SNAP-488 into DLPC NABBs and performed saturation binding with 2D7-Cy5. SEC profile of CCR5-SNAP NABBs shows a profile very like that obtained for empty NABBs. To determine where CCR5-SNAP eluted, we analyzed SEC fractions by western immunoblotting where we can detect down to femtomole quantities of receptor. Western immunoblotting shows that CCR5-SNAP is present in SEC fractions 21 to 23. We tested ligand binding by FCCS and calculated a K_D (5 ± 1) nM for 2D7-Cy5 binding to CCR5-SNAP in NABBs. We did not perform control experiment where 2D7-Cy5 was added to empty NABBs to determine non-specific binding to the NABBs. Yet, a cross-correlation would only be observed if the empty

NABBs fluoresce under 488 nm excitation or are labeled with a 488 nm excitable fluorophore. We have not observed considerable fluorescence from NABBs under 488 nm excitation. Future experiments will test ligand binding of 5P12- and 6P4-647 to CCR5-SNAP NABBs and test the effect of G-protein pre-coupling to CCR5 on chemokine affinity and ratio of high and low affinity receptor fractions.

CHAPTER 5: CONCLUSION

CCR5 is a chemokine receptor that is involved in inflammation, chemotaxis, and T cell activation. CCR5 is also the major co-receptor for HIV-1 glycoprotein Env. Recently, four RANTES analogues were developed to block HIV-1 infection by mutating the first 9 amino acids of RANTES. Despite their extensive pharmacological characterization in cell-based assays, we lack structural and mechanistic insights that explain the RANTES analogues functional selectivity. To address this issue, we performed single molecule fluorescence ligand binding assays using the RANTES analogues and CCR5 to derive equilibrium binding constants. We chose single molecule detection because we can observe reaction intermediates or receptor species that are averaged in ensemble ligand binding assays. To detect ligand binding, we employed fluorescence cross-correlation spectroscopy because fluorescent species concentrations can be derived directly, molecules are detected in solution avoiding immobilization effects, and it is suitable to detect ligand binding in the picomolar to nanomolar range. To perform single molecule assays, we generated a CCR5 construct fused to a SNAP tag for fluorescent labeling and two functional tags at the N- and C-termini of CCR5 for tandem affinity purification. We label CCR5 with Alexa-488 using the SNAP tag and purify the full-length monomeric receptor from receptor truncations and aggregates. We performed intracellular calcium mobilization and cAMP inhibition assays and we demonstrate that CCR5-SNAP can activate G-proteins. We show by TIRF microscopy and flow cytometry that CCR5-SNAP expresses at the cell surface of HEKC293T cells.

We performed saturation and competition-binding assays using Alexa-647 labeled RANTES analogues and purified CCR5-SNAP-488 in micelles by fluorescence cross-correlation spectroscopy. Global fitting analysis of the binding isotherms revealed that 25% of the receptor was functional. Within this fraction, chemokines bound with high affinity to 38% of the receptor and with low affinity to 62% of the active receptor. Competition binding analysis showed that 5P12 and 6P4 recognized the same receptor fractions observed in the saturation binding experiments. Competition analysis showed that Alexa-647 did not interfere with chemokine binding to CCR5-SNAP-488. Competition binding experiments with the sCD4/gp120 complex, RANTES, and MIP-1α revealed that the RANTES analogues remained bound to the receptor even in micromolar competitor concentrations.

We hypothesize that the two CCR5-SNAP species observed by FCCS are due to receptors expressing different levels of covalent modifications. Indeed, we observe by SDS-PAGE analysis two bands which we correlate to the receptor species observed by FCCS. Future experiments such as mass spectrometry on purified CCR5-SNAP will shed insights into the covalent modifications that are present in the extracellular side of the receptor. If possible, enzymatic removal of CCR5-SNAP covalent modifications will shed light into how these modifications affect chemokine binding affinity. In case the covalent modifications are PMTs, CCR5 purification from different immune cells will be required to analyze the receptor by MS and determine if the receptor is differentially modified *in vivo*. Thus far, CCR7 is the only chemokine receptor known to be differentially glycosylated *in vivo*. CCR7 glycosylation is tissue dependent and the presence or lack of glycosylation on CCR7 mediates CCR7 signaling and coupling to

physiological responses. We can imagine that such mechanism of receptor regulation is present on other chemokine receptors and potentially other GPCRs.

We hypothesize that high affinity binding of RANTES and MIP-1α requires pre-coupling of G-protein to CCR5-SNAP. We did not perform ligand-binding measurements in the presence of G-protein because CCR5-SNAP in micelles would not activate G-protein. Given this, we chose to reconstitute CCR5-SNAP into NABBs, which provide a more native lipid environment than detergent micelles. CCR5 has previously been incorporated into NABBs and it was shown that CCR5 is more thermally stable in NABBs than detergent micelles. However, we had to address several limitations with the NABBs before we could incorporate the receptor for G-protein functional studies. Previous NABB preparations were limited by the low purification yield of Zap1. Also, NABBs were assembled in a makeshift platform that did not allow for high-throughput and temperature control of NABB assembly. Lastly, NABBs assembly with the lipid of choice, POPC, yielded heterogeneous preparation, which are not suitable for single molecule experiments.

We optimized the expression and purification of ZapN1, a codon optimized construct derived from Zap1, in *E.* coli. We also developed a novel high-throughout platform for mini-scale chromatography. We devised the platform to be compatible with any 96-well plate for sample collection and the EpMotion 5070 for automated liquid handling. We employed this platform to optimize assembly of NABBs with different saturated and unsaturated lipids. We discovered that NABBs assembled with DLPC are homogeneous by SEC and native-PAGE. NABBs assembled with DLPC are compatible with reagents used in CCR5 solubilization. AFM analysis shows that the DLPC NABBs are discoidal

and homogeneous. We successfully reconstituted rhodopsin-fluorescein and CCR5-SNAP into DLPC NABBs and characterized the assemblies by SEC and FCS. We performed pilot ligand binding studies with 2D7 labeled with Cy5 and show that CCR5-SNAP-488 in DLPC NABBs binds 2D7 with an affinity similar to ones reported in the literature.

We propose to perform future saturation and competition ligand binding studies with CCR5-SNAP-488 reconstituted in DLPC NABBs in the presence and absence of G-protein with 5P12- and 6P4-647. We will test if G-protein affects chemokine affinity and the ratio of high and low affinity receptor fractions. We will then perform saturation or competition ligand binding with the native chemokines to determine if G-protein pre-coupling allows for high affinity binding. We should note that these experiments will require careful optimization since the receptor/G-protein complex is short lived in the presence of GTP/GDP. To lock G-protein in one state, we can employ GTP analogues such as GTPγS, which is a non-hydrolysable nucleotide analogue. Another alternative would be to employ G-protein mimetics such as nanobodies or mini G-proteins, modified G-proteins that bind the receptor but lack the catalytic domain, to study the effect of G-protein on CCR5.

REFERENCES

1. Wesley K. Kroeze, D.J.S., Bryan L. Roth, *G-protein-coupled receptors at a glance.* Journal of Cell Science, 2003. **116**: p. 4867 - 4869.

2. Vsevolod Katritch, V.C., and Raymond C. Stevens, *Structure-Function of the G-protein-Coupled Receptor Superfamily.* Annual Review of Pharmacology and Toxicology 2013. **53**: p. 531 - 556.

3. Robert Fredriksson, M.C.L., Lars-Gustav Lundin and Helgi B. Schiöth, *The G-protein-coupled receptors in the human genome form five main families. Phylogenetic analysis, paralogon groups, and fingerprints.* Molecular Pharmacology, 2003. **63**: p. 1256 - 1272.

4. Kobilka, B.K., *G protein coupled receptor structure and activation.* Biochimica et Biophysica Acta (BBA) - Biomembranes, 2007. **1768**: p. 794 - 807.

5. Sudarshan Rajagopal, K.R., and Robert J. Lefkowitz, *Teaching old receptors new tricks: biasing seven-transmembrane receptors.* Nature Reviews Drug Discovery, 2010. **9**: p. 373-386.

6. Dandan Zhang, Q.Z., and Beili Wu, *Structural Studies of G Protein-Coupled Receptors.* Molecules and Cells, 2015. **38**: p. 836 - 842

7. Grünewald, S.W.S., *Sequence, Structure and Ligand Binding Evolution of Rhodopsin-Like G Protein-Coupled Receptors: A Crystal Structure-Based Phylogenetic Analysis.* PLoS One, 2015. **10**: p. e123533.

8. Etienne Khoury, S.C., and Stéphane A. Laporte, *Allosteric and Biased G Protein-Coupled Receptor Signaling Regulation: Potentials for New Therapeutics.* Frontier Endocrinology, 2014. **5**: p. 68.

9. Rie Nygaard, T.M.F., Birgitte Holst, Mette M. Rosenkilde, Thue W. Schwartz, *Ligand binding and micro-switches in 7TM receptor structures.* Trends in Pharmacological Sciences, 2009. **30**: p. 249 - 259.

10. G. Enrico Rovati, V.C.a.R.R.N., *The highly conserved DRY motif of class A G protein-coupled receptors: beyond the ground state.* Molecular Pharmacology, 2007. **71**: p. 959 - 964.

11. Patrick Scheerer, J.H.P., Peter W. Hildebrand, Yong Ju Kim, Norbert Kraus zlig, Hui-Woog Choe, Klaus Peter Hofmann & Oliver P. Ernst, *Crystal structure of opsin in its G-protein-interacting conformation.* Nature, 2008. **455**: p. 497 - 502.

12. Fei Xu, H.W., Vsevolod Katritch, Gye Won Han, Kenneth A. Jacobson, Zhan-Guo Gao, Vadim Cherezov, Raymond C. Stevens, *Structure of an agonist-bound human A2A adenosine receptor.* Science, 2011. **332**: p. 322 - 327.

13. Guillaume Lebon, T.W., Patricia C. Edwards, Kirstie Bennett, Christopher J. Langmead, Andrew G. W. Leslie & Christopher G. Tate *Agonist-bound adenosine A2A receptor structures reveal common features of GPCR activation.* Nature, 2011. **474**: p. 521 - 525.

14. Olaf Fritze, S.F., Vladimir Kuksa, Krzysztof Palczewski, Klaus Peter Hofmann, and Oliver P. Ernst, *Role of the conserved NPxxY(x)5,6F motif in the rhodopsin*

ground state and during activation. Proceedings of the National Academy of Sciences USA, 2003. **100**: p. 2290 - 2295.

15. Offermanns, N.W.S., *Mammalian G Proteins and Their Cell Type Specific Functions.* Physiological Reviews, 2005. **85**: p. 1159 - 1204.

16. Melvin I. Simon, M.P.S., and Narasimhan Gautam, *Diversity of G Proteins in signal transduction.* Science, 1991. **252**: p. 802 - 808.

17. Guzmán Sánchez-Fernández, S.C., Carlota García-Hoz, Cristiane Benincá, Anna M. Aragay, Federico Mayor Jr., Catalina Ribas, *Gαq signalling: The new and the old.* Cellular Signaling, 2014. **26**: p. 833 - 848.

18. Siehler, S., *Regulation of RhoGEF proteins by G12/13-coupled receptors.* British Journal of Pharmacology, 2009. **158**: p. 41 - 49.

19. Shahriar M. Khan, R.S., Sarah Gora, Peter Zylbergold, Jean-Philippe Laverdure, Jean-Claude Labbé, Gregory J. Miller and Terence E. Hébert, and Eric L. Barker, *The expanding roles of Gβγ subunits in G protein-coupled receptor signaling and drug action.* Pharmacological Reviews, 2013. **65**: p. 545 - 577.

20. Eugenia V. Gurevich, J.J.G.T., Arcady Mushegian, Vsevolod V. Gurevich, *G protein-coupled receptor kinases: More than just kinases and not only for GPCRs.* Pharmacology & Therapeutics, 2012. **133**: p. 40 - 69.

21. Louis M. Lutrell, D.G.-P., *Beyond Desensitization: Physiological Relevance of Arrestin-Dependent Signaling.* Pharmacological Reviews, 2010. **62**: p. 305 - 330.

22. Zastrow, A.C.H.a.M.v., *Regulation of GPCRs by Endocytic Membrane Trafficking and Its Potential Implications.* Annual Review of Pharmacology and Toxicology, 2008. **48**: p. 537 - 568.

23. Amynah A. Pradhan, M.L.S., Brigitte L. Kieffer, Christopher J. Evans, *Ligand-directed signalling within the opioid receptor family.* British Journal of Pharmacology, 2012. **167**: p. 960 - 969.

24. Arun K. Shukla , G.S., Eshan Ghosh, *Emerging structural insights into biased GPCR signaling.* Trends in Biochemical Sciences, 2014. **39**(12): p. 594 - 602.

25. Xavier Deupi, B.K.K., *Energy landscapes as a tool to integrate GPCR structure, dynamics, and function.* Physiology, 2010. **25**: p. 293 - 303.

26. Søren G. F. Rasmussen, B.T.D., Yaozhong Zou, Andrew C. Kruse, Ka Young Chung, Tong Sun Kobilka, Foon Sun Thian, Pil Seok Chae, Els Pardon, Diane Calinski, Jesper M. Mathiesen, Syed T. A. Shah, Joseph A. Lyons, Martin Caffrey, Samuel H. Gellman, Jan Steyaert, Georgios Skiniotis, William I. Weis, Roger K. Sunahara & Brian K. Kobilka, *Crystal structure of the β2 adrenergic receptor-Gs protein complex.* Nature, 2011. **477**: p. 549 - 555.

27. Yanyong Kang, X.E.Z., Xiang Gao, Yuanzheng He, Wei Liu, Andrii Ishchenko, Anton Barty, Thomas A. White, Oleksandr Yefanov, Gye Won Han, Qingping Xu, Parker W. de Waal, Jiyuan Ke, M. H. Eileen Tan, Chenghai Zhang, Arne Moeller, Graham M. West, Bruce D. Pascal, Ned Van Eps, Lydia N. Caro, Sergey A. Vishnivetskiy, Regina J. Lee, Kelly M. Suino-Powell, Xin Gu, Kuntal Pal,

Jinming Ma, Xiaoyong Zhi, Sébastien Boutet, Garth J. Williams, Marc Messerschmidt, Cornelius Gati, Nadia A. Zatsepin, Dingjie Wang, Daniel James, Shibom Basu, Shatabdi Roy-Chowdhury, Chelsie E. Conrad, Jesse Coe, Haiguang Liu, Stella Lisova, Christopher Kupitz, Ingo Grotjohann, Raimund Fromme, Yi Jiang, Minjia Tan, Huaiyu Yang, Jun Li, Meitian Wang, Zhong Zheng, Dianfan Li, Nicole Howe, Yingming Zhao, Jörg Standfuss, Kay Diederichs, Yuhui Dong, Clinton S. Potter, Bridget Carragher, Martin Caffrey, Hualiang Jiang, Henry N. Chapman, John C. H. Spence, Petra Fromme, Uwe Weierstall, Oliver P. Ernst, Vsevolod Katritch, Vsevolod V. Gurevich, Patrick R. Griffin, Wayne L. Hubbell, Raymond C. Stevens, Vadim Cherezov, Karsten Melcher & H. Eric Xu *Crystal structure of rhodopsin bound to arrestin by femtosecond X-ray laser.* Nature, 2015. **523**: p. 561 - 567.

28. Terry Kenakin, A.C., *Signalling bias in new drug discovery: detection, quantification and therapeutic impact.* Nature Reviews Drug Discovery, 2013. **12**: p. 205-216.

29. Aashish Manglik, H.L., Dipendra K. Aryal, John D. McCorvy, Daniela Dengler, Gregory Corder, Anat Levit, Ralf C. Kling, Viachaslau Bernat, Harald Hübner, Xi-Ping Huang, Maria F. Sassano, Patrick M. Giguère, Stefan Löber, Da Duan, Grégory Scherrer, Brian K. Kobilka, Peter Gmeiner, Bryan L. Roth & Brian K. Shoichet, *Structure-based discovery of opioid analgesics with reduced side effects.* Nature, 2016. **537**: p. 185 - 190.

30. Lopalco, L., *CCR5: From Natural Resistance to a New Anti-HIV Strategy.* Viruses, 2010. **2**: p. 574 - 600.

31. Fatima Barmania, M.S.P., *C-C chemokine receptor type five (CCR5): An emerging target for the control of HIV infection.* Applied & Translational Genomics, 2013. **2**: p. 3-16.

32. Denis Sohy, H.Y., Patricia de Nadai, Eneko Urizar, Aude Guillabert, Jonathan A. Javitch, Marc Parmentier and Jean-Yves Springael, *Hetero-oligomerization of CCR2, CCR5, and CXCR4 and the protean effects of "selective" antagonists.* Journal of Biological Chemistry, 2009. **284**: p. 31270 - 31279.

33. Zlotnik, D.R.a.A., *The biology of chemokines and their receptors.* Annual Review of Immunology, 2000. **18**: p. 217 - 242.

34. Kristin L. Gillotte, M.Z., Sissel Lund-Katz, G. M. Anantharamaiah, Paul Holvoet, Ann Dhoest, Mayakonda N. Palgunachari, Jere P. Segrest, Karl H. Weisgraber, George H. Rothblat, Michael C. Phillips, *Apolipoprotein-mediated plasma membrane microsolubilization: Role of lipid affinity and membrane penetration in the efflux of cellular cholesterol and phospholipid.* The Journal of Biological Chemistry, 1999. **274**: p. 2021-2028.

35. Thomas J. Schall, K.B., Richard D. R. Camp, James W. Kaspari, and David V. Goeddel, *Human macrophage inflammatory protein alpha (MIP-1 alpha) and MIP-1 beta chemokines attract distinct populations of lymphocytes.* Journal of Experimental Medicine, 1993. **177**: p. 1821 - 1826.

36. DD Taub, K.C., AR Lloyd, JJ Oppenheim, DJ Kelvin, *Preferential migration of activated CD4+ and CD8+ T cells in response to MIP-1 alpha and MIP-1 beta.* Science, 1993. **260**: p. 355 - 358.

37. Craig B. Wilen, J.C.T., and Robert W. Doms, *HIV: cell binding and entry.* Cold Spring Harbor Perspectives in Medicine, 2012. **2**.

38. Michael Roche, H.S., Renee Duncan, Brendan L. Wilkinson, Kelechi Chikere, Miranda S. Moore, Nicholas E. Webb, Helena Zappi, Jasminka Sterjovski, Jacqueline K. Flynn, Anne Ellett, Lachlan R. Gray, Benhur Lee, Becky Jubb, Mike Westby, Paul A Ramsland, Sharon R. Lewin, Richard J. Payne, Melissa J. Churchill and Paul R. Gorry *A common mechanism of clinical HIV-1 resistance to the CCR5 antagonist maraviroc despite divergent resistance levels and lack of common gp120 resistance mutations.* Retrovirology, 2013. **10**: p. 43.

39. Michael A. Lobritz, A.N.R., Eric J. Arts, *HIV-1 Entry, Inhibitors, and Resistance.* Viruses, 2010. **2**: p. 1069 - 1105.

40. Hubert Gaertner, F.C., Jean-Michel Escola, Gabriel Kuenzi, Astrid Melotti, Robin Offord, Irène Rossitto-Borlat, Rebecca Nedellec, Janelle Salkowitz, Guy Gorochov, Donald Mosier, and Oliver Hartley, *Highly potent, fully recombinant anti-HIV chemokines: Reengineering a low-cost microbicide.* Proceedings of the National Academy of Sciences USA, 2008. **105**: p. 17706-17711.

41. Oliver Hartley, K.D., Danielle Perez-Bercoff, Fabrice Cerini, Anouk Heimann, Hubert Gaertner, Robin E. Offord, Gianfranco Pancino, Patrice Debré, and Guy

Gorochov, *Human immunodeficiency virus type 1 entry inhibitors selected on living cells from a library of phage chemokines.* Journal of Virology, 2003. **77**: p. 6637 - 6644.

42. Clara M. Cardaba, J.S.K., Anja Mueller, *CCR5 internalisation and signalling have different dependence on membrane lipid raft integrity.* Cellular Signaling, 2008. **20**: p. 1687 - 1694.

43. Reem Berro, P.J.K., Danny Lascano, Ayanna Flegler, Kirsten A. Nagashima, Rogier W. Sanders, Thomas P. Sakmar, Thomas J. Hope, John P. Moore, *Multiple CCR5 Conformations on the Cell Surface Are Used Differentially by Human Immunodeficiency Viruses Resistant or Sensitive to CCR5 Inhibitors.* Journal of Virology, 2011. **85**: p. 8227 - 8240.

44. Iva Navratilova, J.S., David G. Myszka, *Solubilization, stabilization, and purification of chemokine receptors using biosensor technology.* Analytical Biochemistry, 2005. **339**: p. 271-281.

45. Nils G. Walter, C.-Y.H., Anthony J. Manzo, and Mohamed A. Sobhy, *Do-it-yourself guide: How to use the modern single molecule toolkit.* Nature Methods, 2008. **5**: p. 475-489.

46. Edward C. Hulme, M.A.T., *Ligand binding assays at equilibrium: validation and interpretation.* British Journal of Pharmacology, 2010. **161**: p. 1219 - 1237.

47. Toews, D.B.B.a.M.L., *Radioligand binding methods: practical guide and tips.* American Journal of Physiology, 1993. **265**: p. L421 - L429.

48. Milev, S., *Isothermal titration calorimetry: Principles and experimental design.* 2013.

49. Elson, E.L., *Fluorescence Correlation Spectroscopy: Past, Present, Future.* Biophysical Journal, 2011. **101**: p. 2855-2870.

50. Kirsten Bacia, S.A.K.a.P.S., *Fluorescence cross-correlation spectroscopy in living cells.* Nature Methods, 2006. **3**: p. 83 - 89.

51. T. Wohland , K.F., R. Hovius , and H. Vogel *Study of Ligand−Receptor Interactions by Fluorescence Correlation Spectroscopy with Different Fluorophores: Evidence That the Homopentameric 5-Hydroxytryptamine Type 3As Receptor Binds Only One Ligand.* Biochemistry, 1999. **38**: p. 8671-8681.

52. Kirsten Bacia, P.S., *Practical guidelines for dual-color fluorescence cross-correlation spectroscopy.* Nature Protocols, 2007. **2**: p. 2842-2856.

53. Jody L. Swift, M.C.B., Dominique Massotte, Tanya E. S. Dahms, and David T. Cramb, *Two-Photon Excitation Fluorescence Cross-Correlation Assay for Ligand−Receptor Binding: Cell Membrane Nanopatches Containing the Human μ-Opioid Receptor.* Analytical Chemistry, 2007. **79**: p. 6783-6791.

54. Thomas Antoine, D.O., Katharina Ebell, Kerrin Hansen, Luc Henry, Frank Becker, Stefan Hannus, *Homogeneous time-resolved G protein-coupled receptor-ligand binding assay based on fluorescence cross-correlation spectroscopy.* Analytical Biochemistry, 2016. **502**: p. 24 - 35.

55. Antje Keppler, S.G., Thomas Gronemeyer, Horst Pick, Horst Vogel, Kai Johnsson, *A general method for the covalent labeling of fusion proteins with small molecules in vivo.* Nature Biotechnology, 2003. **21**: p. 86-89.

56. Ch. Wellerdieck, M.O., L. Pott, S. Korsching, G. Gisselman, H. Hatt, *Functional expression of odorant receptors of the zebrafish Danio rerio and of the nematode C. elegans in HEK293 cells.* Chemical Senses, 1997. **22**: p. 467-476.

57. Berchiche, Y.A., et al., *Different effects of the different natural CC chemokine receptor 2b ligands on beta-arrestin recruitment, Galphai signaling, and receptor internalization.* Mol Pharmacol, 2011. **79**(3): p. 488-98.

58. Leduc, M., et al., *Functional selectivity of natural and synthetic prostaglandin EP4 receptor ligands.* J Pharmacol Exp Ther, 2009. **331**(1): p. 297-307.

59. Martin Geiser, R.C., Delia Drewello, and Rita Schmitz, *Integration of PCR fragments at any specific site within cloning vectors without the use of restriction enzymes and DNA ligase.* Biotechniques, 2001. **31**: p. 88 - 90.

60. Benhur Lee, M.S., Cedric Blanpain, Benjamin J. Doranz, Jalal Vakili, Pui Setoh, Ellen Berg, Gao Liu, H. Robert Guy, Stewart R. Durell, Marc Parmentier, Chung Nan Chang, Ken Price, Monica Tsang and Robert W. Doms, *Epitope mapping of CCR5 reveals multiple conformational states and distinct but overlapping structures involved in chemokine and coreceptor function.* Journal of Biological Chemistry, 1999. **274**: p. 9617 - 9626.

61. Cédric Blanpain, B.J.D., Antoine Bondue‡, Cédric Govaerts, Anne De Leener, Gilbert Vassart, Robert W. Doms, Amanda Proudfoot and Marc Parmentier, *The core domain of chemokines binds CCR5 extracellular domains while their amino terminus interacts with the transmembrane helix bundle.* Journal of Biological Chemistry, 2003. **278**: p. 5179 - 5187.

62. Ali Salahpour, S.E., Bernard Masri, Vincent Lam, Larry S. Barak and Raul R. Gainetdinov, *BRET biosensors to study GPCR biology, pharmacology, and signal transduction.* Frontiers in Endocrinology, 2012. **3**: p. 105.

63. Tajib Mirzabekov, N.B., Michael Farzan, Wolfgang Hofmann, Peter Kolchinsky, Lijun Wu, Richard Wyatt, and Joseph Sodroski, *Enhanced expression, native purification, and characterization of CCR5, a principal HIV-1 coreceptor.* Journal of Biological Chemistry, 1999. **274**: p. 28745 - 28750.

64. Lydia Nisius, M.R., Luca Vangelista, Stephan Grzesiek, *Large-scale expression and purification of the major HIV-1 coreceptor CCR5 and characterization of its interaction with RANTES.* Protein Expression and Purification, 2008. **61**: p. 155 - 162.

65. Qiuxiang Tan, Y.Z., Jian Li, Zhuxi Chen, Gye Won Han, Irina Kufareva, Tingting Li, Limin Ma, Gustavo Fenalti, Jing Li, Wenru Zhang, Xin Xie, Huaiyu Yang, Hualiang Jiang, Vadim Cherezov, Hong Liu, Raymond C. Stevens, Qiang Zhao, and Beili Wu, *Structure of the CCR5 chemokine receptor-HIV entry inhibitor maraviroc complex.* Science, 2013. **1387**: p. 1387 - 1390.

66. Kobilka, B., *Amino and carboxyl terminal modifications to facilitate the production and purification of a G protein-coupled receptor.* Analytical Biochemistry, 1995. **231**: p. 269 - 271.

67. Donald MacKenzie, A.A., Paul Hargrave, J. Hugh McDowell, Robert S. Molday, *Localization of binding sites for carboxyl terminal specific anti-rhodopsin monoclonal antibodies using synthetic peptides.* Biochemistry, 1984. **23**: p. 6544 - 6549.

68. Laurie L. Molday, R.S.M., *1D4: A Versatile Epitope Tag for the Purification and Characterization of Expressed Membrane and Soluble Proteins.* Methods in Molecular Biology, 2014. **1177**: p. 1 - 15.

69. S. Rüttinger, V.B., B. Krämer, R. Erdmann, R. Macdonald, F. Koberling., *Comparison and Accuracy of Methods To Determine The Confocal Volume for Quantitative Fluorescence Correlation Spectroscopy.* Journal of Microscopy, 2008. **232**: p. 343-352.

70. Yong Hwee Foo, N.N.-R., Don C. Lamb, Sohail Ahmed, Thorsten Wohland, *Factors affecting the quantification of biomolecular interactions by fluorescence cross-correlation spectroscopy.* Biophysical Journal, 2012. **102**: p. 1174 - 1183.

71. Oliver Hegener, L.P., Frank Runkel, Stephan Leonhardt Baader, Joachim Kappler, and Hanns Häberlein, *Dynamics of beta2-adrenergic receptor-ligand complexes on living cells.* Biochemistry, 2004. **43**: p. 6190 - 6199.

72. S. J. Briddon, R.J.M., Y. Cordeaux, F. M. Flavin, J. A. Weinstein, M. W. George, B. Kellam, and S. J. Hill *Quantitative analysis of the formation and diffusion of A1-adenosine receptor-antagonist complexes in single living cells.* Proceedings of the National Academy of Sciences USA, 2004. **101**: p. 4673 - 4678.

73. Ross Corriden, L.E.K., Barrie Kellam, Stephen J. Briddon and Stephen J. Hill, *Kinetic analysis of antagonist-occupied adenosine-A3 receptors within membrane microdomains of individual cells provides evidence of receptor dimerization and allosterism.* FEBS Journal, 2014. **28**: p. 4211 - 4222.

74. Adam J. Kuszak, S.P., Jessica P. Anand, Henry I. Mosberg, Nils G. Walter and Roger K. Sunahara, *Purification and functional reconstitution of monomeric mu-opioid receptors: allosteric modulation of agonist binding by Gi2.* Journal of Biological Chemistry, 2009. **284**.

75. Andre De Lean, J.M.S., Robert J. Lefkowitz, *A ternary complex model explains the agonist-specific binding properties of the adenylate cyclase-coupled beta-adrenergic receptor.* Journal of Biological Chemistry, 1980. **255**: p. 7108 - 7117.

76. Jeffrey J. Liu, R.H., Vsevolod Katritch, Raymond C. Stevens, Kurt Wüthrich, *Biased signaling pathways in β2-adrenergic receptor characterized by 19F-NMR.* Science, 2012. **335**: p. 1106 - 1110.

77. Isabel D. Alves, D.D., Bernard Mouillac, Zdzislaw Salamon, Gordon Tollin, Victor J. Hruby, Solange Lavielle, and Sandrine Sagan, *The two NK-1 binding sites correspond to distinct, independent, and non-interconvertible receptor*

conformational states as confirmed by plasmon-waveguide resonance spectroscopy. Biochemistry, 2006. **45**: p. 5309 - 5318.

78. Hyun Ryoung Kim, S.L., Sandrine Sagan, *The two NK-1 binding sites are distinguished by one radiolabelled substance P analogue.* Biochemical and Biophysical Research Communications, 2003. **306**: p. 725 - 729.

79. Hanne Hastrup, T.W.S., *Septide and neurokinin A are high-affinity ligands on the NK-1 receptor: evidence from homologous versus heterologous binding analysis.* FEBS Letters, 1996. **399**: p. 264 - 266.

80. Isabel D. Alves , E.S., Gerard Bolbach , Lynda Millstine , Solange Lavielle , and Sandrine Sagan, *Analysis of an intact G-protein coupled receptor by MALDI-TOF mass spectrometry: molecular heterogeneity of the tachykinin NK-1 receptor.* Analytical Chemistry, 2007. **79**: p. 2189 - 2198.

81. Philippe Colin, Y.B., Isabelle Staropoli, Yongjin Wang, Nuria Gonzalez, Jose Alcami, Oliver Hartley, Anne Brelot, Fernando Arenzana-Seisdedos, and Bernard Laganea, *HIV-1 exploits CCR5 conformational heterogeneity to escape inhibition by chemokines.* Proceedings of the National Academy of Sciences USA, 2013. **110**: p. 9475-9480.

82. Ivelin S. Georgiev, M.G.J., Yongping Yang, Mallika Sastry, Baoshan Zhang, Ulrich Baxa, Rita E. Chen, Aliaksandr Druz, Christopher R. Lees, Sandeep Narpala, Arne Schön, Joseph Van Galen, Gwo-Yu Chuang, Jason Gorman, Adam Harned, Marie Pancera, Guillaume B. E. Stewart-Jones, Cheng Cheng, Ernesto

Freire, Adrian B. McDermott, John R. Mascola and Peter D. Kwong, *Single-Chain Soluble BG505.SOSIP gp140 Trimers as Structural and Antigenic Mimics of Mature Closed HIV-1 Env.* Journal of Virology, 2015. **89**: p. 5318 - 5329.

83. Simon Hoffenberg, R.P., Alexei Carpov, Denise Wagner, Aaron Wilson, Sergei Kosakovsky Pond, Ross Lindsay, Heather Arendt, Joanne DeStefano, Sanjay Phogat, Pascal Poignard, Steven P. Fling, Melissa Simek, Celia LaBranche, David Montefiori, Terri Wrin, Pham Phung, Dennis Burton Wayne Koff, C. Richter King, Christopher L. Parks and Michael J. Caulfield, *Identification of an HIV-1 clade A envelope that exhibits broad antigenicity and neutralization sensitivity and elicits antibodies targeting three distinct epitopes.* Journal of Virology, 2013. **87**: p. 5372 - 5383.

84. Benjamin J. Doranz, S.S.W.B., and Robert W. Doms, *Use of a gp120 binding assay to dissect the requirements and kinetics of human immunodeficiency virus fusion events.* Journal of Virology, 1999. **73**: p. 10346 - 10358.

85. Adam M. Knepp, A.G., Sourabh Banerjee, Thomas P. Sakmar, and Thomas Huber, *Direct measurement of thermal stability of expressed CCR5 and stabilization by small molecule ligands.* Biochemistry, 2011. **50**: p. 502 - 511.

86. Sourabh Banerjee, T.H., Thomas P. Sakmar, *Rapid Incorporation of Functional Rhodopsin into Nanoscale Apolipoprotein Bound Bilayer (NABB) Particles.* Journal of Molecular Biology, 2008. **377**: p. 1067 - 1081.

87. Floudas, P.T.C.A., *Elucidating a key anti-HIV-1 and cancer-associated axis: the structure of CCL5 (Rantes) in complex with CCR5.* Science Reports, 2014. **4**: p. 5447 - 5456.

88. Einat Schnur, N.K., Yuri Zherdev, Eran Noah, Tali Scherf, Fa-Xiang Ding, Svetlana Rabinovich, Boris Arshava, Victoria Kurbatska, Ainars Leonciks, Alexander Tsimanis, Osnat Rosen, Fred Naider, Jacob Anglister, *NMR mapping of RANTES surfaces interacting with CCR5 using linked extracellular domains.* FEBS Journal, 2013. **280**: p. 2068 - 2084.

89. Luminita Duma, D.H., Marco Rogowski, Paolo Lusso, Stephan Grzesiek, *Recognition of RANTES by extracellular parts of the CCR5 receptor.* Journal of Molecular Biology, 2007. **365**: p. 1063 - 1075.

90. Won-Tak Choia, R.N., Mia Coetzera, Philippe Colin, Bernard Lagane, Robin E. Offord, Oliver Hartley and Donald E. Mosier, *CCR5 mutations distinguish N-terminal modifications of RANTES (CCL5) with agonist versus antagonist activity.* Journal of Virology, 2012. **86**: p. 10218 - 10220.

91. Yunjun Ge, D.Y., Antao Dai, Caihong Zhou, Yue Zhu, and Ming-Wei Wang., *The putative signal peptide of glucagon-like peptide-1 receptor is not required for receptor synthesis but promotes receptor expression.* Bioscience Reports, 2014. **34**: p. e00152.

92. Xiao-Ming Guan, T.S.K., Brian K. Kobilka, *Enhancement of membrane insertion and function in a type IIIb membrane protein following introduction of a*

cleavable signal peptide. Journal of Biological Chemistry, 1992. **267**: p. 21995 - 21998.

93. Peter M. Schmidt, L.G.S., Rebecca M. Attwood, Xiaowen Xiao, Tim E. Adams, Jennifer L. McKimm-Breschkin, *Taking down the FLAG! How insect cell expression challenges an established tag-system.* PLoS One, 2012. **7**: p. e37779.

94. Morag Rose Hunter, N.L.G., and Michelle Glass, *Sulfation of the FLAG epitope is affected by co-expression of G protein-coupled receptors in a mammalian cell model.* Science Reports, 2016. **6**: p. 27316.

95. Keizo Tano, S.S., Julia Collier, Robert S Foote, Sankar Mitra, *Isolation and structural characterization of a cDNA clone encoding the human DNA repair protein for O6-alkylguanine.* Proceedings of the National Academy of Sciences USA, 1990. **87**: p. 686-690.

96. Pia C. Rummel, S.T., Lærke S. Hansen, Trine P. Petersen, Alexander H. Sparre-Ulrich, Trond Ulven and Mette M. Rosenkilde., *Extracellular disulfide bridges serve different purposes in two homologous chemokine receptors, CCR1 and CCR5.* Molecular Pharmacology, 2013. **84**: p. 335 - 345.

97. Cédric Blanpain, B.L., Jalal Vakili, Benjamin J. Doranz, Cédric Govaerts, Isabelle Migeotte, Matthew Sharron¶, Vincent Dupriez,Gilbert Vassart, Robert W. Doms and Marc Parmentier, *Extracellular cysteines of CCR5 are required for chemokine binding, but dispensable for HIV-1 coreceptor activity.* Journal of Biological Chemistry, 1999. **274**: p. 18902 - 18908.

98. Jurgen Wess, S.N., Zvi Vogel, Roberto Maggio, *Functional role of proline and tryptophan residues highly conserved among G protein-coupled receptors studied by mutational analysis of the m3 muscarinic receptor.* EMBO Journal, 1993. **12**: p. 331 - 338.

99. Ethan B. Van Arnam, H.A.L., and Dennis A. Dougherty, *Dissecting the Functions of Conserved Prolines within Transmembrane Helices of the D2 Dopamine Receptor.* ACS Chemical Biology, 2011. **6**(10): p. 1063.

100. Sine, W.Y.L.S.M., *Principal pathway coupling agonist binding to channel gating in nicotinic receptors.* Nature, 2005. **438**: p. 243 - 247.

101. Isabelle M. Paulsen, I.L.M., Susan M. J. Dunn, *Isomerization of the proline in the M2-M3 linker is not required for activation of the human 5-HT3A receptor.* Journal of Neurochemistry, 2009. **110**: p. 870 - 878.

102. Cédric Govaerts, C.B., Xavier Deupi, Sébastien Ballet, Juan A. Ballesteros, Shoshana J. Wodak, Gilbert Vassart, Leonardo Pardo and Marc Parmentier, *The TXP motif in the second transmembrane helix of CCR5. A structural determinant of chemokine-induced activation.* Journal of Biological Chemistry, 2001. **276**(13217 - 13225).

103. Christoph Seibert, M.C., Anthony Sanfiz, Brian T. Chait, and Thomas P. Sakmar, *Tyrosine sulfation of CCR5 N-terminal peptide by tyrosylprotein sulfotransferases 1 and 2 follows a discrete pattern and temporal sequence.* Proceedings of the National Academy of Sciences USA, 2002. **99**: p. 11031 - 11036.

104. Michael Farzan, T.M., Peter Kolchinsky, Richard Wyatt, Mark Cayabyab, Norma P Gerard, Craig Gerard, Joseph Sodroski, Hyeryun Choe, *Tyrosine sulfation of the amino terminus of CCR5 facilitates HIV-1 entry.* Cell, 1999. **96**: p. 667 - 676.

105. Yvonne Döring, H.N., Manuela Mandl, Birgit Kramp, Carlos Neideck, Dirk Lievens, Maik Drechsler, Remco T.A. Megens, Pathricia V. Tilstam, Marcella Langer, Helene Hartwig, Wendy Theelen, Jamey D. Marth, Markus Sperandio, Oliver Soehnlein, Christian Weber, *Deficiency of the sialyltransferase St3Gal4 reduces Ccl5-mediated myeloid cell recruitment and arrest: short communication.* Circulation Research, 2014. **114**: p. 976 - 981.

106. Sangbae Lee, A.M., Supriyo Bhattacharya, Nathan Robertson, Reinhard Grisshammer, Christopher G. Tate, and Nagarajan Vaidehi, *How Do Short Chain Nonionic Detergents Destabilize G-Protein-Coupled Receptors?* Journal of the American Chemical Society, 2016. **138**: p. 15425–15433.

107. Mohammed Jamshad, J.C., Yu-Pin Lin, Sarah J. Routledge, Zharain Bawa, Timothy J. Knowles, Michael Overduin, Niek Dekker, Tim R. Dafforn, Roslyn M. Bill, David R. Poyner, Mark Wheatley, *G-protein coupled receptor solubilization and purification for biophysical analysis and functional studies, in the total absence of detergent.* Bioscience Reports, 2015. **35**: p. e00188.

108. Makoto Kubota, T.T., Toshiyuki Kohno, and Kaori Wakamatsu, *GDP–GTP Exchange Processes of Gαi1 Protein are Accelerated/Decelerated Depending on the Type and the Concentration of Added Detergents* Journal of Biochemistry, 2009. **146**: p. 875 - 880.

109. Krishna Vukoti, T.K., Laura Macke, Klaus Gawrisch, and Alexei Yeliseev, *Stabilization of functional recombinant cannabinoid receptor CB(2) in detergent micelles and lipid bilayers.* PLoS One, 2012. **7**: p. e46290.

110. Popot, J.-L., *Amphipols, Nanodiscs, and Fluorinated Surfactants: Three Nonconventional Approaches to Studying Membrane Proteins in Aqueous Solutions.* Annual Review of Biochemistry, 2010. **79**: p. 737 - 775.

111. Tingjuan Gao, C.D.B., Wei He, Feliza Bourguet, Sonny Ly, Federico Katzen, Wieslaw A. Kudlicki, Paul T. Henderson, Ted A. Laurence, Thomas Huser, and Matthew A. Coleman, *Characterizing diffusion dynamics of a membrane protein associated with nanolipoproteins using fluorescence correlation spectroscopy.* Protein Science, 2011. **20**: p. 437 - 447.

112. Jun Zhang, E.R., Marianna Dioszegi, Rama Kondru, Andre DeRosier, Eva Chan, Stephan Schwoerer, Nick Cammack, Michael Brandt, Surya Sankuratri and Changhua Ji, *The Second Extracellular Loop of CCR5 Contains the Dominant Epitopes for Highly Potent Anti-Human Immunodeficiency Virus Monoclonal Antibodies.* Antimicrobial Agents and Chemotherapy, 2007. **51**: p. 1386-1397.

113. Arun Sivashanmugam, V.M., Chunxian Cui, Yonghong Zhang, Jianjun Wang, Qianqian Li, *Practical protocols for production of very high yields of recombinant proteins using Escherichia coli.* Protein Science, 2009. **18**: p. 936-948.

114. I. G. Denisov, Y.V.G., A. A. Lazarides, and S. G. Sligar *Directed Self-Assembly of Monodisperse Phospholipid Bilayer Nanodiscs with Controlled Size.* Journal of the American Chemical Society, 2004. **126**: p. 3477 - 3487.

115. Timothy H. Bayburt , Y.V.G., and Stephen G. Sligar, *Self-Assembly of Discoidal Phospholipid Bilayer Nanoparticles with Membrane Scaffold Proteins.* Nano Letters, 2002. **2**: p. 853 - 856.

116. Krutika Bavishi, T.L., Karen L. Martinez, Birger Lindberg Møller & Eduardo Antonio Della Pia, *Application of nanodisc technology for direct electrochemical investigation of plant cytochrome P450s and their NADPH P450 oxidoreductase.* Science Reports, 2016. **6**: p. 29459.

117. Nicholas Skar-Gislinge, J.B.S., Kell Mortensen, Robert Feidenhans, Stephen G. Sligar, Birger Lindberg Møller, Thomas Bjørnholm, and Lise Arleth, *Elliptical structure of phospholipid bilayer nanodiscs encapsulated by scaffold proteins: casting the roles of the lipids and the protein.* Journal of the American Chemical Society, 2010. **132**: p. 13713 - 13722.

118. Nivedita Mitra, Y.L., Jian Liu, Eugene Serebryany, Victoria Mooney, Brian T. DeVree, Roger K. Sunahara, and Elsa C. Y. Yan, *Calcium-Dependent Ligand Binding and G-protein Signaling of Family B GPCR Parathyroid Hormone 1 Receptor Purified in Nanodiscs.* ACS Chemical Biology, 2013. **8**: p. 617 - 625.

119. Matthew R. Whorton, M.P.B., Søren G. F. Rasmussen , Bo Huang , Richard N. Zare , Brian Kobilka , and Roger K. Sunahara, *A monomeric G protein-coupled*

receptor isolated in a high-density lipoprotein particle efficiently activates its G protein. Proceedings of the National Academy of Sciences USA, 2007. **104**: p. 7682 - 7687.

120. Won-Seok Choi, W.J.R., David L. Stokes and Barry S. Coller, *Three-dimensional reconstruction of intact human integrin αIIbβ3: new implications for activation-dependent ligand binding.* Blood, 2013. **122**: p. 4165 - 4171.

121. Lei Zhang, J.S., Giorgio Cavigiolio, Brian Y. Ishida, Shengli Zhang, John P. Kane, Karl H. Weisgraber, Michael N. Oda, Kerry-Anne Rye, Henry J. Pownall and Gang Ren, *Morphology and structure of lipoproteins revealed by an optimized negative-staining protocol of electron microscopy.* Journal of Lipid Research, 2011. **52**: p. 175 - 184.

122. Madhumita Guha, D.L.G.a.O.G., *Effects of acyl chain length, unsaturation, and pH on thermal stability of model discoidal HDLs.* Journal of Lipid Research, 2008. **49**: p. 1752 - 1761.